PROBABILISTIC RISK MAPPING COUPLING BAYESIAN NETWORKS AND GIS, AND BAYESIAN MODEL CALIBRATION OF SUBMARINE LANDSLIDES

A Dissertation

by

PATRICIA YSOLDA VARELA GONZALEZ

Submitted to the Office of Graduate and Professional Studies of
Texas A&M University
in partial fulfillment of the requirements for the degree of

DOCTOR OF PHILOSOPHY

Chair of Committee,	Zenon Medina-Cetina
Committee Members,	Marian Eriksson
	Gretchen Miller
	Arash Noshadravan
Head of Department,	Robin Autenrieth

December 2017

Major Subject: Civil Engineering

ABSTRACT

A spatial and causal probabilistic methodology is introduced for risk assessment based on the coupling of a conceptual Bayesian Network (BN) model and GIS to generate *risk* maps. The proposed integration of these spatial events is referred to as *BN+GIS*, which features forward and inverse modeling, denoted in this work as *spatial prognosis* and *spatial diagnosis,* respectively. This approach is illustrated through two case studies: (1) environmental risk associated to oil and gas site developments implemented in the Barnett Shale Play in Texas, and (2) landslide susceptibility in the Elliott State Forest in the Oregon Coastal Range. This approach will equip stakeholders, such as land owners, operators, regulators, government officials, and other related organizations with a platform that can help them improve the assessment of future potential risk scenarios, and to identify likely consequences that would lead to undesirable states of environmental risks ahead of time. A sensitivity analysis was performed on *BN+GIS* to study the influence of some of the user-defined parameters on the model's results, such as sample size, spatial interval of the systematic sampling methodology, and the prescribed *diagnosis* distribution used for decision making purposes. As an additional effort to portray the potential application of the Bayesian paradigm on risk assessment, a parameter estimation methodology is implemented using bathymetry data and CPT logs. This approach is illustrated through a study case, where information was mined from existent landslides to perform a Bayesian calibration on an infinite slope model. This approach allowed to estimate posterior probability distributions of physical parameters

given a prescribed factor of safety, to assess the most likely depth of failure, and to identify the optimum amount of samples required to maximize the reliability of the inferences. This work focusses on providing a substantial contribution to improved policymaking and management through the use of integrated sources of evidence such as real data, model predictions and experts educated beliefs.

DEDICATION

This work is dedicated to my family. Their ceaseless support and encouragement represented a good source of fuel that I have used to go through this journey from the day I came to Texas A&M University. A special feeling of gratitude to my brother, Jose Miguel Varela, for being a role model, for consistently showing me the right way to do things, and for kindheartedly receiving me in his house every year.

I also dedicate this work to the chosen family I met in College Station, Jeniree Flores, Agustin Diaz, Nefeli Moridis and Troy Brown. My heart is full of joy because I have had the privilege to keep them close every step of the way. I will always appreciate their unconditional support, which I have received in ways I had never imagined possible.

ACKNOWLEDGEMENTS

I would like to thank my committee chair, Dr. Zenon Medina-Cetina, for his dedication to my professional and technical development. He saw something in me and gave the fight when it was needed, and now I am truly thankful for his efforts. I hope that in the future, I can make a difference in a young professional the way he has done it for me.

I would like to acknowledge the contributions of my committee member, Dr. Marian Eriksson, for her guidance and support throughout the course of this research. After a countless amount of coffee cups and lunches, I feel fortunate to consider her a good friend.

It is important to highlight the generous contributions of *Grupo Plenum* to the Stochastic Geomechanics Laboratory, particularly Dr. Victor Gutierrez and Dr. Alberto Muñoz. Another special tanks to Mr. Andrew Haigh for receiving me as his intern during difficult times, and to all other members of the *Gardline* office in Houston.

Another important acknowledgement goes to my Stochastic Geomechanics Laboratory colleagues. Specially Yichuan Zhu and Roneet Daas for helping me out at different stages of my research. To Tam Duong and Jungrak Son for their warm and kind personality, and to Rachel Holanda for proof reading the manuscripts.

Thanks also go to the department faculty and staff for making my time at Texas A&M University a great experience. It was an extraordinary pleasure to meet and work with Theresa Taeger, Laura Byrd, Kay Choate, and Maria Medrano.

CONTRIBUTORS AND FUNDING SOURCES

This work was supervised by a dissertation committee consisting of Texas A&M University Professors Zenon Medina-Cetina (Chair), Gretchen Miller and Arash Noshadravan of the Department of Civil Engineering, Professor Marian Eriksson of the Department of Ecosystem Science and Management. Dr. William Haneberg of the Kentucky Geological Survey, University of Kentucky, also advised and supervised portions of this dissertation.

The data analyzed for Chapter V was provided by *Gardline*, and the script used for its implementation was modified from previous work developed on the Stochastic Geomechanics Laboratory. All other work conducted for the dissertation was completed by the student, under the advisement of Dr. Zenon Medina-Cetina and Dr. Marian Eriksson.

This work was made possible by the funding provided by the *Grupo Plenum* with the project “Stochastic Geomechanics for Shale Gas Developments”. Its contents are solely the responsibility of the authors and do not necessarily represent the official views of the *Grupo Plenum*.

TABLE OF CONTENTS

Page

LIST OF FIGURES

Page

LIST OF TABLES

CHAPTER I

INTRODUCTION

Risk assessment in engineering is conducted with the purpose of performing informed decision-making that can be applied to solve problems related to environmental conservation and societal impact while maximizing material or financial resources (Faber and Stewart 2003). The heterogeneous nature of the available information that can serve for a detailed and comprehensive risk assessment methodology embodies a challenge for the standardization of methods that can be implemented for diverse purposes. Bayesian networks (BN) provides a suitable solution for modeling the interaction and the causal relationship between variables through a probabilistic approach, and for the integration of real data with experts beliefs (Korb and Nicholson 2004; Chen and Pollino 2012).

Most of this work focuses on the use of BNs within a risk assessment framework, scaled to a spatial domain through the use of GIS. To illustrate the proposed methodology, a first approach is discussed in chapter I, were the environmental risk due to oil and gas (O&G) site developments is mapped, given the occurrence of an event that could potentially trigger adverse consequences. This approach couples the use of a conceptual Bayesian Network (BN) model and GIS to generate *risk maps*, illustrated through a case study implemented in the Barnett Shale Play. The proposed integration of these spatial events is referred to as *BN+GIS*, which features forward and inverse modeling. The proposed methodology is illustrated through the development of risk maps aimed at improving the process selecting optimal locations for future infrastructure while

accounting for potential environmental impacts to *aquifers*, s*urface water*, *ecoregions*, and *land use - land cover*. This approach can equip stakeholders, such as land owners, operators, regulators and other related organizations with a platform that can help them improve the assessment of future potential environmental risk scenarios, and to identify likely scenarios that would lead to undesirable states of environmental risks ahead of time.

A parametrical sensibility analysis of the study case implemented in chapter II is illustrated in chapter III. The methodology used to estimate the marginal probabilities of the network consists on a systematic spatial sampling that requires the selection of sampling intervals (g) and buffer sizes (b). A factorial experimental design is used to estimate the influence of these parameters on the results to map the uncertainty and to estimate their best combination to maximize the significance of the results. The sensitivity of the model to policy-making decisions using a diagnostic type of reasoning were also analyzed in this work. A spatial analysis was conducted yielding the visualization and identification of areas with higher levels of uncertainty and a quantification of the autocorrelation structure of the results. The implementation of the parametric sensitivity analysis discussed in this chapter allows to expand the understanding of the spatial behavior of the uncertainty, and to maximize the quality and quantity of the probabilistic inferences derived from the use of *BN+GIS*. Consequently, this updated state of knowledge can be used by stakeholders to further improve the decision making process.

Chapter IV describes the implementation of the *BN+GIS* tool for the quantification of landslide vulnerability and risk using LiDAR-derived data and other ancillary information.

In this chapter, LiDAR derived information such as a Digital Terrain Model (DTM) and a Canopy Height Model (CHM) from a designated area of the Oregon Coast Range, is used to develop a set of landslides hazard and risk index maps. The manipulation of these models resulted in three maps designated as *Physical Model*, *Vegetation Density* and *Wetness Index* that were combined with an existing landslide susceptibility map known as *SLIDO*. The integration of these maps served as input to a Bayesian network capable of assessing the state of risk. Forward and inverse modeling were also tested in this study case to provide illustrative examples of how *BN+GIS* can aid the strategic allocation of resources to minimize the vulnerability to landslides.

As an additional application of the Bayesian paradigm for aiding a better decision-making process, chapter V illustrates a study case where the probability of failure of submarine landslides is assessed by combining sources of evidence such as bathymetry and geotechnical survey logs (CPT). An algorithm using a Bayesian model calibration method is used to estimate the parameters of an infinite slope model, which serves as the physical association between the tested variables. The hypothesis of this chapter consists on the belief that this method can aid to significantly reduce the vulnerability of offshore infrastructure design, especially when limited information is available.

The principal objective of this work is to contribute to the enhancement of current practices for integrated risk and reliability analysis through the use of Bayesian probabilistic approaches. It is hypothesized that the replication of the proposed methodology can be systematically used for a robust, informed and comprehensive decision-making process. The specific objectives of this work are:

- To develop a methodology for the systematic implementation of Bayesian networks within a risk assessment framework that can be scaled to a spatial domain.
- To map prognostic and diagnostic scenarios that can aid the decision-making process.
- To map the uncertainty and examine the conditions that can allow decision makers to maximize the significance of the model's estimated scenarios.
- To conduct large scale risk assessment through a logical and efficient integration of disparate sources of information, model predictions, and expert's beliefs.
- To provide a methodology capable to improve the reliability on modeled estimates of physical parameters when limited access to different sources of evidence exists.

CHAPTER II

COUPLING BAYESIAN NETWORKS AND GIS FOR PROGNOSIS AND DIAGNOSIS ENVIRONMENTAL RISK ASSESSMENT

Introduction

With the surge of new technologies for unconventional reservoir exploration, completion, and enhanced production, there is a growing need to provide decision-making systems capable of maximizing economic benefits while simultaneously minimizing likely environmental and social impacts. That is, there is the need to develop Environmentally Friendly Drilling (EFD) systems given the shortage of integrated decision making methodologies to identify, quantify, and manage different sources of risk for a given oil and gas (O&G) site development (Yu et al. 2012; Ethridge et al. 2015). Moreover, environmental risk assessment and mapping still demand further advances (Lan et al. 2015) and can be improved by the development of a standard methodology for scaling the risk to a spatial and temporal domain.

The risk management process as described by Ethridge et al. (2015) consists on a series of steps involving the interaction between different stakeholders such as problem identification, risk management options, assessments, decision, and evaluation, which leads to a single problem evaluation at a time. These steps are implemented using scientific information along with policies and protocols described by The Texas Commission of Environmental Quality (TCEC), the Railroad Commission of Texas (RRC), the United

States Environmental Protection Agency (US EPA) and local municipalities that serve as the regulating authorities regarding the required environmental conditions for the approval of drilling permits and their operation's management in the State of Texas (Ethridge et al. 2015). The International Association of Drilling Contractors (IADC 2009) recommends the use of a health, safety, and environmental risk assessment matrix classifying qualitatively the identified hazards in order to define the correspondent risk-reduction measures and define the tolerability of the consequences. The potential hazards that operators consider for risk management include blowout, toxic release, explosions, rigging/ lifting incidents, fire, and structural failure among others (IADC 2009). Individual O&G companies often contract environmental firms to maximize the efficiency of impact assessment and risk management, resulting in tools such as the one described by Westfall (2016). The process described by Westfall (2016) includes the revision of financial, environmental, social, and health management plans through a series of tables and flowcharts that ultimately rank the magnitude and manageability of the impacts. Yet, these types of approaches are mostly utilized for *risk management* and do not consider the probabilistic causal relationships between the implemented activities. Furthermore, they are not yet implemented within standardized procedures for a quantitative *risk assessment* and do not allow for the consideration of more than one site at a time.

The objective of this work is to generate environmental risk maps that can guide selection of optimal well placement within an EFD framework. To achieve this goal, a new methodology is introduced that integrates the use of Bayesian networks (BN) and geographical information systems (GIS). A unique benefit of this approach is the

possibility to perform forward and inverse modeling, denoted in this work as spatial prognosis and spatial diagnosis, respectively. The new system is referred to herein as *BN+GIS*; it is anticipated that it will improve the understanding of the state of environmental risk for a given O&G site development based on inputs from different stakeholders, including operators, land owners, regulators and non-government organizations. BNs rely on the definition of probability distributions of variables that are depicted as nodes, and their relationships represent causal evidence for a process at a given point in space and time.

The proposed BN model was formulated as a proof of concept using four key environmental variables (parent nodes) that cover prescribed time and spatial domains. These input variables comprise four maps in and around the Barnett Shale Formation in northern Texas, where the development of the O&G industry has been particularly intense for more than a decade. Dissensions concerning air quality, noise pollution, land footprint, water resources, ecosystem degradation, waste disposal and ecological risk to wildlife due to O&G site developments are among the most common environmental topics examined in the literature (Dincer 1999; Mariano and La Rovere 2007; HARC 2010; Vidic et al. 2013; Brittingham et al. 2014; Wright 2014; Ethridge et al. 2015; Wesfall 2016). A set of conditions used to select the four parent nodes in this work included (1) relevance of the variable to the objective of the model, (2) availability of information on reliable and official web sources, (3) spatial coverage of 100% of the area of interest, and (4) the ability to be measured or validated with field examination. Based on this criteria, the four key parent nodes considered by the authors were proximity to surface water bodies (*W*), the

presence of aquifers (*A*), the existent ecoregions (*E*), and the correspondent land use/ land cover (*L*). The selection of these four variables provided minimum temporal variability which allows the model to create prognostic and diagnostic scenarios that can be representative of relatively large periods of time. The joint influence of these variables on the given site defined the environmental sensibility (*ES*) node, which allows the model to introduce a risk index in a prognostic analysis. Although the definition of the number of variables for the proposed model is not exhaustive, the authors consider that this can serve well to integrate a first conceptual spatial environmental risk assessment on the impact of O&G site developments. On the other hand, the diagnostic reasoning allows for the mapping of likely scenarios targeting a prescribed state of risk (i.e. risk index) for the same variable conditions and provides a unique tool for generating policy making scenarios based on acceptable risks (Reid 2000; IADC 2009). BNs, such as the one proposed in this work, provide a mathematical tool for combining multiple variables through conditional probability tables (CPTs) reflecting cause-effect relationships using simple graphics comprised of nodes and arrows (Korb and Nicholson 2004).

A number of studies have explored the use of BNs to represent different processes (both physically based and non-physically based). Aguilera et al. (2011) presented an analysis of 1,375 references based on ISI Web of Knowledge (Reuters 2010) and narrowed their search to 128 publications on BN applications completed between 1990 and 2010. These included 27% applications in computer science, 21% in mathematics, 16% in engineering, 15% in health science, 11% in life science, 4% in sociology and education, and 4% in environmental sciences, which shows a limited contribution of BN to

environmental studies. This suggests that there is a need to further develop applications of BN within environmental studies.

Early applications implementing decision-making tools and spatial analysis via BN and GIS include classification of digital surface models (Brunn and Weidner 1997), risk assessment of desertification due to burned forests (Stassopoulou et al. 1998), and salinization monitoring of farmlands (Kiiveri and Caccetta 1998). More recently, spatial data managed through a GIS has been used as input for BNs for a wide variety of applications, such as image interpretation (Growe et. al. 2000), model design using spatial relationships (Walker et. al. 2005), land use or land cover change (Bacon et. al. 2002; Kocabas and Dragicevic 2007; Aitkenhead and Aalders 2009), environmental analysis of habitat suitability (Smith et al. 2007), marine planning (Stelzenmüller et al. 2010) and risk assessment (Grêt-Regamey and Straub 2006; Medina-Cetina and Nadim 2008; Li et al. 2010; Liu et. al. 2015). Another branch of exploitation of BN's capability to combine diverse sources of information from data and experts beliefs for decision making has been explored by Huang and Yuan (2007) and Huang et al. (2008) with applications on data mining from spatially explicit sources including GPS data, remote sensing, GIS, and ancillary information. Most of these studies use spatial data that has been pre- and post-processed using GIS or remote sensing tools and introduce the use of BNs to model cause-effect processes.

Johnson et al. (2012) summarized some of the most relevant BN and GIS integration study cases that illustrate good practice for different applications. They identified four ways in which the integration has been performed by researchers: (1) GIS input to BN; (2)

GIS input to and output from BN; (3) BN and GIS complex interactions; and (4) BN and GIS within a larger framework. The first two categories are related to the use of spatial data to populate the variables of the BN and its potential to produce results that can be mapped. Yet, the complex interactions of BN and GIS consist on the model's capability to update and account for uncertainty. BN and GIS within a larger framework describe the uses in which the output of the BN is part of an integrated model of a higher order. The closest depiction of the conceptual model presented in this study within the characterization provided by Johnson et al. (2012) corresponds to the category (3) with the additional, and important, feature of performing diagnostic analysis to update the likely states of the input variables.

Suggestions of proper practices for the design of BNs (Marcot et al. 2006) and its integration with GIS (Chen and Pollino 2012) have been made. An important aspect to consider is whether BNs are a friendly tool for data integration. Further, BNs can be misused if unreliable models are used. Therefore, it is necessary that the overall model is reviewed by several experts to ensure the coherence of the node's relationships and proper calibration with appropriate information, when possible, so that meaningful results may be extracted (Marcot et al. 2006). Chen and Pollino (2012) recommend certain protocols that should be followed for achieving the best results from combining BN and GIS. These practices include the clear definition of the model's objective and the appropriate use of the information so that the nature of the system is accurately represented. They also suggest the use of as few node's classes as possible when the CPTs are defined by expert's

belief and the inclusion of a comprehensive documentation of the assumptions and reasoning behind the definition of each variable.

When implementing BNs and coupling them with GIS, there is a paucity of studies that calibrate and validate their models (Marcot et al. 2006; Aguilera et al. 2011). Even fewer studies developed the automation of the BN for GIS applications in order for it to be accessed from an ArcGIS environment (Grêt-Regamey and Straub 2006; Varela 2013) or to perform diagnostic spatial analysis. In this case study, the GIS analysis is not limited to the data pre- and post- processing. On the contrary, a process was designed to automate the implementation of a BN from the ArcMap toolbox in a way that the user does not need to do any computation but to run a tool from the software.

Most BN representations of risk-based decision-making processes focus mainly on methodological aspects, such as the analysis of dependencies between events, the integration of qualitative and quantitative evidence, the integration of temporal aspects, uncertainty quantification and uncertainty propagation (Weber et al. 2012) but do not focus often on spatial applications. Medina-Cetina and Nadim (2008) introduced a definition of risk widely used in engineering applications into the form of a BN, based on the delineation of hazards, vulnerability, and elements at risk that can be addressed using different sources of evidence such as existing data, model predictions and expert's educated opinions. The proposed methodology within this study extends Medina-Cetina and Nadim's risk assessment approach from *a point* to *a space* formulation when applied to the environmental risk assessment for O&G site developments.

Yu (2010) developed a Bayesian decision network model for describing a comprehensive system of activities developed by the O&G industry when a site is chosen for drilling. This model evaluates the combination of several technologies in *decision* nodes that are grouped as *site and rig*, *power*, and *operations* categories. The causal dependencies, derived from the deterministic choices made in the decision nodes, are also discriminated according to *cost*, *environmental impact*, and *public perception.* The consecutive propagation of the information through the model allows for making probabilistic inferences about the state of the emissions, footprint, and monetary costs for each subsystem. This probabilistic approach provides a value of risk that serves as a decision-making factor which is obtained after evaluating a combination of technologies for a single site at a specific geographical location. To ensure the applicability of Yu's model based on environmental and societal requirements, Medina-Cetina and Varela (2012) enhanced the decision-making model by coupling it with the Score Card System (HARC 2010). To follow up with the real applications of BNs for improved economic, social, and environmental decision-making, additional capability to scale the model to a spatial and/or temporal domain was required. To test the hypothesis that these types of risk scenarios can be mapped and used for a systematic decision making process became the principal motivation for the development of the methodology proposed in this work for merging BNs and GIS capabilities in a comprehensive O&G risk assessment model.

Considering these antecedents, the key contributions of this work are: (1) the definition of environmental risk scenarios based on the analysis of surface water bodies, aquifers, ecoregions and land use / land cover maps, (2) the development of a computational tool to

assess risk maps through a BN model under prognostic and diagnostic modeling, and consequently, (3) the improvement of the decision-making process associated to the selection of environmentally friendly suitable regions to locate O&G operation sites reasoning in prognosis and diagnosis.

Methodology

The proposed *BN+GIS* methodology consists of four phases: (I) data collection, (II) data pre-processing, (III) data analysis, and (IV) data post-processing (Fig. 2.1). The data collection comprises gathering the relevant spatial data from different publicly available repositories. A CPT designating the influence of the input variables on the results and the definition of the coefficients used to transform the probability distribution into a state of risk are also prepared in this stage. On the data pre-processing phase, ArcMap 10 is used to transform the maps to an adequate projection system and to extract the spatial data from the area of interest. In this phase is also prepared the classification of the parent nodes into discrete states (e.g. high, moderate, and low). The criteria used for the classification of the nodes, for the selection of the CPT values, and for the definition of the aforementioned coefficients can be derived either from data collection, model predictions, or expert's beliefs, as discussed by Marcot et al. (2006), Medina-Cetina and Nadim (2008), and Chen and Pollino (2012). A Python algorithm (version 2.6) was developed and embedded into ArcToolbox with the name of *BN+GIS* to extract the spatial samples and perform the BN analysis while populating the output feature classes displayed in phase IV.

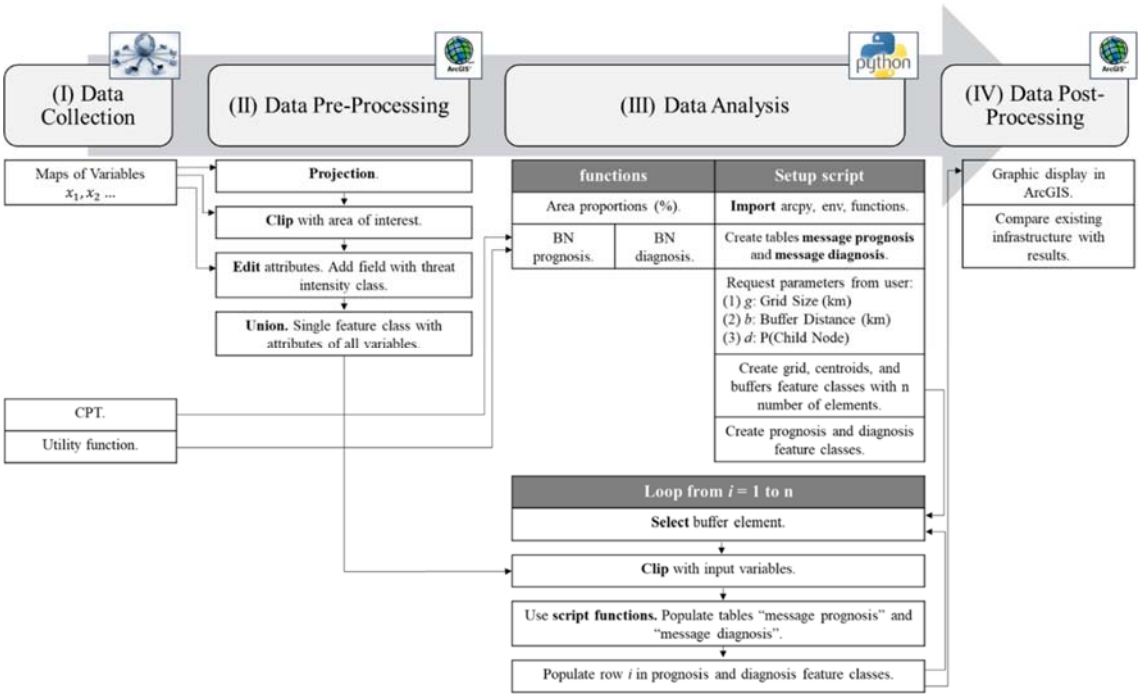

Fig 2.1 Methodological sequence of *BN+GIS* tool.

Definition of Marginal Probabilities

A systematic sampling is performed to obtain the marginal probabilities of the BN from the spatial domain. The script generates a grid over the study area and creates a buffer around the centroid of each grid element to define the spatial extent of the samples used to assess the BN's inputs. The distance between the centroids of the grid elements serve as sample intervals, and the buffer serves as the plot area. Each buffer functions as a clip tool to extract the spatial information from the input variables, which is used to compute the percentage of the area that each state of the four parent nodes occupies within the buffer (see Fig. 2.2). This proportion provides the BN's marginal probability distribution of each discrete element in the study area.

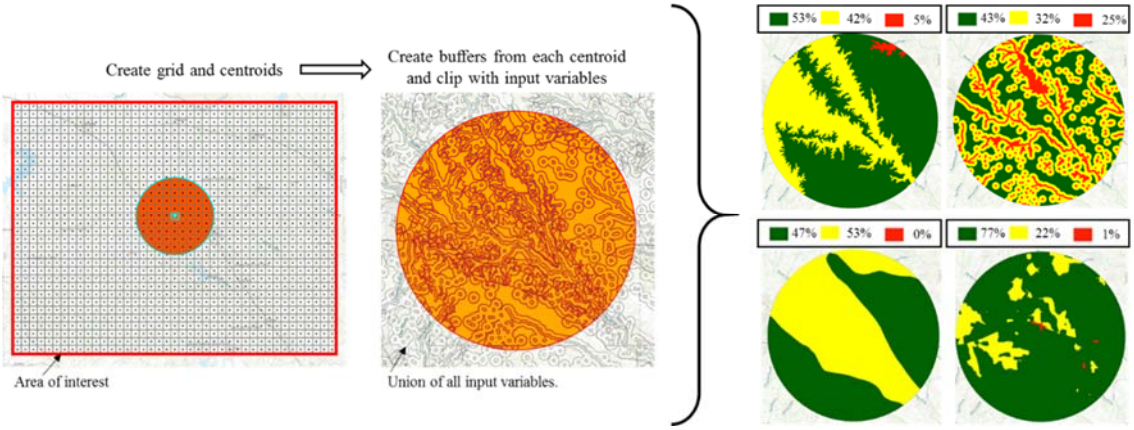

Fig 2.2 Methodology used in BN+GIS to generate the marginal probability distributions of parent nodes.

The size of the grid elements and the buffer distances are parameters specified by the user through the toolbox's interactive window when the *BN+GIS* is launched (see setup script Fig. 2.1). To reach full coverage of the study area during the spatial sampling process, it is desired to select buffer distances (b) equal or larger than half of the diagonal of the grid cells (g) as seen in Fig. 2.3-A, where the relationship can be expressed as $b \geq \frac{\sqrt{2}}{2} g$. Notice that when this condition is achieved, an overlapped sampling area is produced between contiguous grid elements. The proportion of the areas that will be sampled multiple times will rise as the buffer distance increases with respect to the grid size, as illustrated in Fig. 2.3-B.

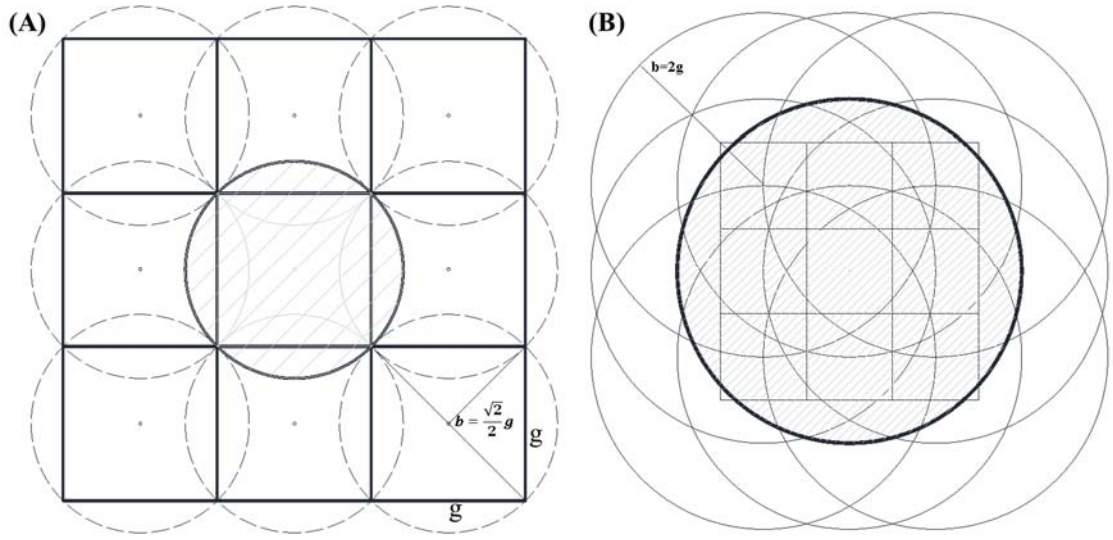

Fig 2.3 Graphical relationship between grid size (g) and buffer distance (b) during spatial sampling. Shaded areas shown as the sampling coverage of the central grid element for (A) minimum buffer size for 100% spatial coverage, and (B) Buffer size 2 times the grid size.

Bayesian Networks and Risk Assessment

Bayesian Networks

Bayesian Networks are a graphical modeling method used to represent the causal dependencies between continuous or discrete random variables of a process through a probabilistic approach that are able to follow the natural structure of a process (Korb and Nicholson 2004). The Bayes theorem is described by Korb and Nicholson (2004) to be a representation of the most elemental structure of the probabilistic inference as seen in Fig. 2.4, where a BN of the normalized conditional probability between a hypothesis H (child node) and the evidence E (parent node) is illustrated.

Fig 2.4 BN on causal relationship between the evidence (E) and the hypothesis (H) depicting the Bayes Theorem. Modified from Korb and Nicholson (2004). There might be multiple parents/children.

A *prognosis* type of reasoning is performed when the model maps the evidence from the parents to the child node. This concept represents predictive reasoning or a forward modeling, where the causes provide a posterior state of the effects, updating the condition of the child node (Korb and Nicholson 2004; Medina-Cetina and Nadim 2008; Varela 2013). Consider a BN with a simple structure of *n* nodes ($X_1 = x_1, X_2 = x_2, \dots, X_n = x_n$) with $n - 1$ independent parent nodes connected to one child node. Using the chain rule, the joint probability distribution of this model can be expressed as $P(x_1, x_2, \dots, x_n) = P(x_1) \times P(x_2|x_1) \times \dots \times P(x_n|x_1, \dots, x_{n-1}) = \prod_i P(x_i|\, x_1, x_2, \dots, x_{i-1})$. Note that $\prod_i P(x_i|\, x_1, x_2, \dots, x_{i-1}) = \prod_i P(x_i|\, Parents(X_i))$. Given the assumed independence of the parent nodes, it is inferred that $P(x_2|x_1) = P(x_2)$, $P(x_3|x_1, x_2) = P(x_3)$, and so on, until $P(x_{n-1}|x_1, x_2, \dots, x_{n-2}) = P(x_{n-1})$. The child node $X_n = x_n$ depends on the $n - 1$ independent parent nodes, hence, the joint probability function is expressed as $\prod_i P(x_i|\, Parents(X_i)) = P(x_1) \times P(x_2) \times \dots \times P(x_{n-1}) \times P(x_n|x_1, x_2, \dots, x_{n-1})$. If all nodes are discretized in *m* classes or states, where $X_{ij} = (x_{i_1}, x_{i_2}, \dots, x_{i_m})$, then $\prod_{ij} P\left(x_{ij}\middle|\, Parents(X_{ij})\right)$ returns a list of m^n values with all the possible combinations of *m* discrete states of *n* probabilistic nodes. Obtaining the posterior state of the probability

of the child node requires to sum the values of this list that correspond to each state m, and can be expressed by equation 2.1.

$$P(Child_j) = P(x_{n_j}) = \begin{cases} P\left(x_{n_{j=1}} \middle| Parents(X_{ij})\right) = \sum_{i=1}^{n} \prod_{ij} P(x_{ij} | Parents(X_{ij})) \quad \forall\, x_{n_{j=1}} \\ P\left(x_{n_{j=2}} \middle| Parents(X_{ij})\right) = \sum_{i=1}^{n} \prod_{ij} P(x_{ij} | Parents(X_{ij})) \quad \forall\, x_{n_{j=2}} \\ \vdots \\ P\left(x_{n_{j=m}} \middle| Parents(X_{ij})\right) = \sum_{i=1}^{n} \prod_{ij} P(x_{ij} | Parents(X_{ij})) \quad \forall\, x_{n_{j=m}} \end{cases} \tag{2.1}$$

The values used for Eq. 2.1 correspond to the marginal probabilities of the parent nodes and the conditional probability table (CPT) quantifying the dependence of the child node, which are mined from available evidence or experts beliefs.

When the model propagates the evidence from the child to the parent nodes, it is performed an inverse modeling or *diagnosis* type of reasoning (Korb and Nicholson 2004). In this case, the child node is fixed with a prescribed distribution to assess the new conditions of the marginal probabilities of $x_1, x_2, \dots, x_{n-1}$. In other words, the modeler can populate the probability distribution of $P'(x_n)$ and update the state of the parent nodes ($P'(x_1, x_2, \dots, x_{n-1}|x_n)$). Using Bayes' Theorem of conditional probability illustrated in Fig. 4, the diagnostic modeling can be expressed as $P'(x_1, x_2, \dots, x_{n-1}|x_n) = \frac{\prod_i P(x_i|Parents(X_i)) \times P'(x_n)}{P(x_n)}$. In this case, using the probabilistic semantics of BN, $P'(x_1, x_2, \dots, x_{n-1}|x_n)$ represents the updated parent node, $\prod_i P(x_i|\, Parents(X_i))$ is the

likelihood, $P'(x_n)$ represents the prior distribution, and $\frac{1}{P(x_n)}$ represents a normalizing constant α used to allow the updated probabilities to sum to 1 (Korb and Nicholson 2004). This can be re-written as $P'(Parents|Child) = \alpha P(Child|Parents)P'(Child)$. Considering the *m* number of states of all the BN's nodes, the updated probabilities of the parent nodes can be expressed by Eq. 2.2.

$$P(Parent_{ij}) = P'(x_1, x_2, \dots, x_{n-1}|x_n) \begin{cases} \sum_{1}^{m^{n-1}} \frac{\prod_{ij} P(x_{ij}|\, Parents(X_{ij})) \times P'(x_n)}{\sum_{1}^{m^n}[P(x_{ij}|\, Parents(X_{ij})) \times P'(x_n)]} \ \forall\, i = 1 \ \wedge j = 1 \\ \sum_{1}^{m^{n-1}} \frac{\prod_{ij} P(x_{ij}|\, Parents(X_{ij})) \times P'(x_n)}{\sum_{1}^{m^n}[P(x_{ij}|\, Parents(X_{ij})) \times P'(x_n)]} \ \forall\, i = 1 \ \wedge j = 2 \\ \vdots \\ \sum_{1}^{m^{n-1}} \frac{\prod_{ij} P(x_{ij}|\, Parents(X_{ij})) \times P'(x_n)}{\sum_{1}^{m^n}[P(x_{ij}|\, Parents(X_{ij})) \times P'(x_n)]} \ \forall\, i = n-1 \ \wedge j = m \end{cases} \quad (2.2)$$

To illustrate the implementation of BN, Fig. 2.5 introduces the model used in this work, with parent nodes: surface water -*W*, aquifers -*A*, ecoregions -*E* and land use/cover -*L* and one child node, Environmental Sensibility -*ES*, illustrating the cause and effect relationship between the selected variables and a probabilistic joint state of the environmental impact due to O&G operations. Notice that the oval nodes represent probability functions discretized in three classes named low, moderate and high.

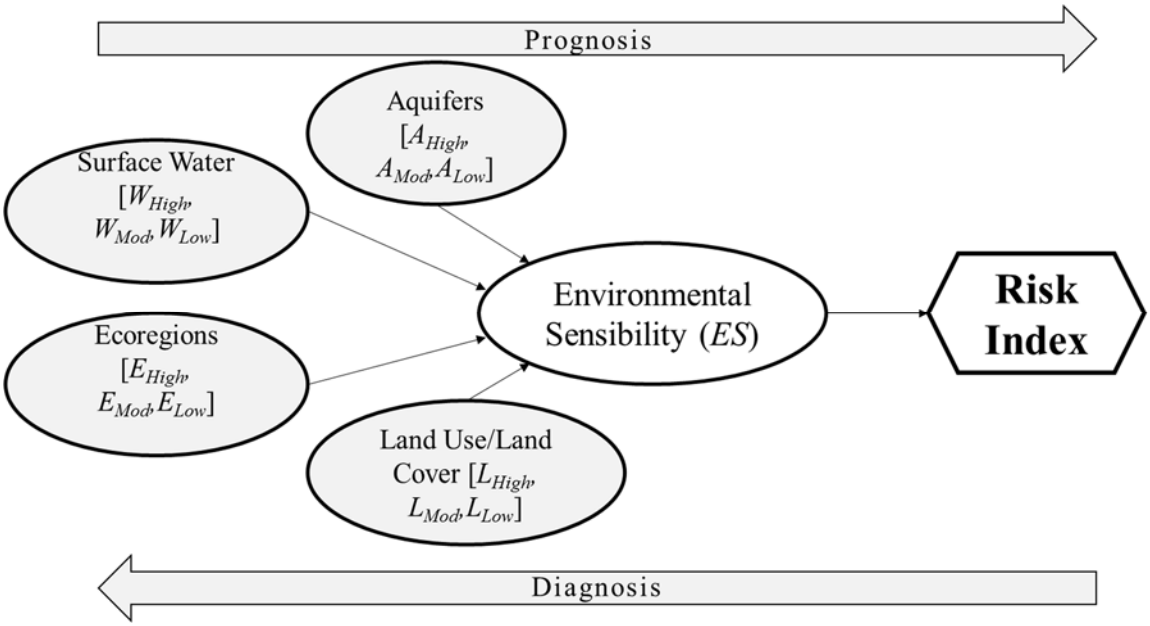

Fig 2.5 Proposed BN model for environmental Risk Assessment.

The *BN+GIS* script loops through each grid element and populates a *prognosis* table with the $P(ES_j)$ list as illustrated in Fig. 2.1. The conditional probability described in Eq. 2.1 is depicted by a CPT (Table 2.1) that joins the probability of the parent nodes where the influence of each variable has been equally weighted. For this proof-of-concept model, the CPT was populated using a subjective criterion based on experts opinions due to the lack of evidence or observations that can be used to assess the influence of *W*, *A*, *E* and *L* on the environmental risk. The authors defined these values considering higher probabilities of ES_{High} when the parent nodes are high and vice versa. Notice that parent nodes are treated as independent variables with respect to each other. The fact that the model introduces independency among the variables is to guarantee the simplicity of the model, which would allow proofing the coupling of BN with GIS. To depart from the simplicity of the model will require further phenomenological examination such as the

work conducted by Tong and Chen (2002), Sohl and Sayler (2008) or GWP (2014) for modeling the relationship between land use and surface water quality, ecoregions and aquifers, respectively.

Table 2.1 Conditional probability table of environmental sensibility (*ES*) node given parent nodes classes.

Parent Node 1 (*A*, *W*, *E*, or *L*)	**Parent Node 2 (*A*, *W*, *E*, or *L*)**	**Parent Node 3 (*A*, *W*, *E*, or *L*)**	**Parent Node 4 (*A*, *W*, *E*, or *L*)**	**P(*ES*: High)**	**P(*ES*: Moderate)**	**P(*ES*: Low)**
High	High	High	High	0.950	0.040	0.010
High	High	High	Moderate	0.800	0.150	0.050
High	High	High	Low	0.800	0.100	0.100
High	High	Moderate	Moderate	0.450	0.450	0.100
High	High	Moderate	Low	0.600	0.200	0.200
High	High	Low	Low	0.450	0.100	0.450
High	Moderate	Moderate	Moderate	0.150	0.800	0.050
High	Moderate	Moderate	Low	0.200	0.600	0.200
High	Moderate	Low	Low	0.200	0.200	0.600
High	Low	Low	Low	0.100	0.100	0.800
Moderate	Moderate	Moderate	Moderate	0.025	0.950	0.025
Moderate	Moderate	Moderate	Low	0.050	0.800	0.150
Moderate	Moderate	Low	Low	0.100	0.450	0.450
Moderate	Low	Low	Low	0.050	0.150	0.800
Low	Low	Low	Low	0.010	0.040	0.950

Once the child node is assessed, the utility function shown in Eq. 2.3 (adapted from Korb and Nicholson 2004), is implemented to transform the probability distribution into a single useful index that quantifies the model's output. To reach a single value, it is assigned a weighted designation of coefficients (e.g. $c_1 = 1, c_2 = 0.5, c_3 = 0$) to the probabilistic levels of the child node. For the model proposed in this work, this function quantifies each state of the risk index, therefore the maximum coefficient ($c_1 = 1$) is assigned to ES_{High} since it embodies the most unfavorable state.

$$U(C) = c_1 P(ES_{High}) + c_2 P(ES_{Mod}) + c_3 P(ES_{Low}) \quad (2.3)$$

Risk Assessment

There are different definitions of risk currently in use within engineering and scientific applications. For instance, the definition provided by Jones (2006) states that the risk is "the probable frequency and probable magnitude of future loss" (p. 7). This definition includes the probabilistic approach that is used in this study but focusses on the likelihood of a natural threat or any other catastrophic event. On the other hand, a more neutral definition is conceived by the ISO (2009), which describes risk as the influence of the uncertainty on the objects of study. Purdy (2010) rephrases this definition as "the consequence of an organization setting and pursuing objectives against an uncertain environment" (p. 882). According to this definition, risk is the result of a configuration of uncertain events and is able to describe both loss and benefits.

The Office of the United Nations Disaster Relief Coordinator (UNDRO 1979) relates the risk as a function of the *Hazard*, *Vulnerability* and *Elements at Risk*. The Hazard is described by Medina-Cetina and Nadim (2008) as the probability of a threat occurring, and the Vulnerability is described as the conditional probability of an event occurring given the intensity of the threat. The Elements at Risk are defined by UNDRO (1979) as the social, economic or environmental elements that are exposed to a triggering event. If the parent nodes of the proposed BN model are considered as Hazards, and the conditional probability of the ES is considered as the Vulnerability of the modeled system; then Eq. 1 can be interpreted as the UNDRO (1979) definition of Risk as follows: $Risk =$

$$[Hazard] * [Vulnerability] * [Consequences] = [\mathrm{P}(W) * \mathrm{P}(A) * \mathrm{P}(E) * \mathrm{P}(L)] * [\mathrm{P}(ES \mid W, A, E, L)] * [\mathrm{U}(\mathrm{C})].$$

In this study case, P(W), P(A), P(E) and P(L) are marginal probabilities of the hazard, depicting the state of the threat to those variables given a triggering event due to O&G operations. P($ES \mid W$, A, E, L) is an assessment of the vulnerability given the states of the hazards. The utility function U(C) is evaluating the impact of the consequences (C) as a single risk index. The implementation of U(C) as defined in Eq. 3 translates the probability of ES to a value that oscillates between 0 and 1, indicating the minimum and maximum Risk Index, respectively. This method has been successfully implemented by Medina-Cetina and Nadim (2008) and by Gardoni and LaFave (2016).

Case Study

The benchmark BN model proposed in this study was implemented in the Barnett Shale area located at the central-northern region of Texas. The intensive research made in this play, due to the increased development of its gas resources, has created a substantial amount of available information, where economic, societal, environmental and other technical data can be reached through numerous official sources. Additionally, the Barnett Shale was selected due to its importance in the local and national economy, given that the growth of the production in this play has been a key factor for unconventional reservoirs all over the country, as discussed by Montgomery et al. (2005).

The Barnett Shale is a geological formation located in the Fort Worth basin. Pollastro et al. (2007) defines the Fort Worth Basin as a depression that deepens and wedges to the

northeast encompassing approximately 38,100 km^2. The age of the Barnett Shale is middle-late Mississippian, and the shale represents the primary source rock of gas in the Bendarch-Fort Worth basin in Texas. The formation is a thermally mature and organic rich shale, making it a large unconventional gas reservoir (Pollastro et al. 2007). The Texas RRC (2014) states that the Barnet Shale lies within twenty five counties and is located in the north eastern region of Texas (Fig. 2.6), including the Dallas-Fort Worth metropolitan area.

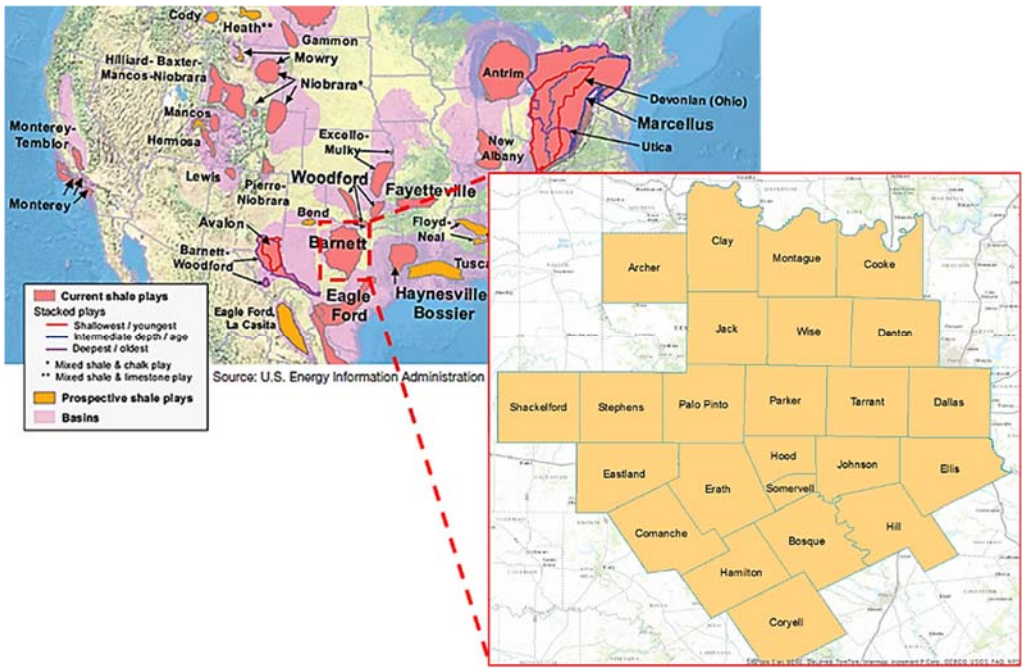

Fig 2.6 Shale Gas Plays and Location of Study Area. Modified from: EIA, 2011.

State of Parent Nodes

The classification of the four parent nodes was made using a criterion that the authors considered provided a reasonable estimation of the environmental risk. Each parent node responds to the state of the variable given the occurrence of a potential triggering event

with possible negative environmental impacts, such as hydrocarbon spills, increased footprint, and pollutant emissions among others. Conversely, while a spill event does not occur at a drilling location, its correspondent risk index should be equal to zero; even though, the hazard does not change. If the vulnerability of the model is updated as the drilling campaign advances, lower values of the risk index would be observed. This updating feature is not presented in this work.

An environmental impact assessment of a given O&G site development depends on multiple elements that may include the depletion or contamination of natural resources, air pollution, ecosystem degradation, potential alteration of forests and protected areas such as National Parks, archaeological sites and land and habitat fragmentation among many other factors (Dincer 1999; Mariano and La Rovere 2007; IADC 2009; Vidic et al. 2013; Wright 2014). For the development of this conceptual model, the authors selected four variables that can be mapped across the complete study area with available and reliable public data. Similar mapping can be replicated with other variables. For *BN+GIS* under a risk assessment framework, the spatially discretized state of the hazard was defined as intensity levels of the probability of a threat to *A*, *W*, *E* and *L* given a triggering event due to O&G developments. Fig. 2.7 shows the spatial representation of the parent nodes using the following criteria:

Aquifers (A)

Operation activities such as O&G drilling or production could potentially affect the quality or deplete the water sources, making the presence of underground major or minor water bodies an important topic to consider. The spatial data was retrieved from the Texas Water Development Board (TWDB 2006a; TWDB 2006b) and the Oklahoma Water Resources Board (OWRB 2006a; OWRB 2006b) in polygon geodatabase format (scale 1:250,000). These files were modified to define the hazard levels for this variable as follows:

- High: is composed of the outcrop zones of any major or minor aquifer. It represents most of the recharge zones, where the aquifer formation is exposed to the surface. The hazard is higher in this zone due to the sensitivity of the water quality given any triggering event on the surface or in the wellbore.
- Moderate: represents the area where the aquifer is below the outcrop formation meaning that if a well is perforated in that zone, the aquifer will be reached. These zones are called subcrop or downdip regions and represent a medium level of hazard since the aquifers could be reached by a drilling operation or the site could be located at the recharge zone of the aquifer.
- Low: are the zones where major or minor aquifers are absent on the surface and subsurface. If a triggering even occurs, the aquifer is not going to be directly affected because is not in contact with the wellbore. However, a minimum hazard level is considered for this state, given that any triggering event could reach a stream or water body that contributes to the recharge zone of any major or minor aquifer.

Surface Water (W)

The surface water bodies represent areas with a particular environmental and social sensitivity for placing a rig site. These concerns are related to accidental oil spills, waste water disposal, water depletion and wildlife conservation (Vidic et al. 2013; Brittingham et al. 2014). The hazard related to the surface water bodies can be defined by their setback distance from the O&G wells, but no current federal regulation exists that can be used as a norm for defining these buffers. In Texas the Oil and Gas Division of the RRC, the primary regulatory jurisdiction over oil and gas issues, does not stipulate specific limitations about the distance of the wellheads to the surface water bodies. However, local cities such as Fort Worth mention either restrictions for issuing permits to gas wells drilled within any floodplain or floodway identified by the Federal Emergency Management Agency (FEMA) and have defined setback distances from protected buildings or protected areas of 100m (Forth Worth City Council 2009). A regulatory ordinance in Coppell City also requires minimum setback distances of 100m from non-residential areas if it is approved by two thirds of the City Council and if they reach unanimous consent of the property owners within a 333 m radius (City of Coppell 2013). In other cases, local regulations require larger setbacks, such as the town of Flower Mound; in its Ordinance N° 29-11 (Council of the Town of Flower Mound 2011), the municipal government prohibits issuing well permits closer than 500m from parks, residences, fresh water wells and other official or habitable buildings. Due to the lack of regulation of setbacks from water bodies, the authors consider that the current protocols designed for urban infrastructure could be used as a reference for the definition of hazard levels on this model.

Therefore, the hazard to water bodies associated to the placement of O&G wells and its supplementary infrastructure installation was defined as:

- High: one hundred meters (100m) from a water body.
- Moderate: one hundred to five hundred meters (100m – 500m) from a water body.
- Low: more than five hundred meters (500m) from a water body.

The data was retrieved from the United States Geological Survey (USGS 2010). According to the USGS feature directory for national hydrography datasets, stream/river, perennial stream, inundation areas, perennial lake/pond larger than 2,500 m^2, swamp/marsh and reservoirs (artificial basins for accumulating liquids) larger than 2,500 m^2 were selected for preparing the surface water variable. The selected minimum areas of surface water bodies was considered by the authors as a reasonable criteria to reduce the dataset to a manageable size without compromising the significance of the results.

Ecoregions (E)

The ecoregions are defined as areas where the ecosystems possess similar types, quality and quantity of natural resources (US EPA 2011). This map was developed under the hypothesis that ecological regions can be categorized due to the combination of different natural expressions such as geology, physiography, vegetation, climate, soils type, land use, wildlife and hydrology. The level IV ecoregions map was used for this study (Scale 1:250,000) and was retrieved from the U.S. Environmental Protection Agency (EPA) website for Texas and Oklahoma states. The hazard levels recognized for this variable were defined by the authors using the following criteria:

- High: are areas with elevated precipitation levels where the soils possess a high capability to hold nutrients and the vegetation is abundant, including wooded forests. Placing a rig site in this zone requires clearing arboreal vegetation, causing an important negative footprint impact, and representing a potential threat for the water quality on the area.
- Moderate: are isolated wooded areas on sandstones and shale beds with irregular topography with a history of O&G production. The soil does not hold many nutrients but the placement of a well site in these areas might lead to logging activities and flattening the surface, which denotes a moderate footprint impact.
- Low: are either dry badlands, flat prairies with lower variety and quantity of vegetation, or even sandy / acidic soils that are unable to support an extensive ecosystem. These conditions allow the threat to have a low environmental impact given that the vegetation density is low and few water bodies are present.

Land Use / Land Cover (L)

This variable represents a description of the land surface in terms of the type of soil and vegetation present and the particular use given to it. Urban areas, wetlands and agricultural lands are all delineated in this classification system. These data were retrieved from the U.S. Department of Agriculture (NRCS-USDA 2007) website at a scale of 1:24,000. The spatial distribution of the hazard for this variable is based on the presence of important features that could cause a higher ecosystem footprint when the land is altered and if a potential accidental spill occurs. The description of the hazard levels were defined by the

authors using a professional judgement, which is consistent with a previous approach used for cataloging environmental sensitivity of the land performed by Jensen et al. (1998).

- High: are agricultural lands with low sparse grasslands, conifer forests, wetlands, lakes, reservoirs and beaches. The hazard is considered higher when an area is currently less affected by human activities, e.g., wild lands.
- Moderate: are composed of urban areas, croplands, savannas and rangelands. The impact of placing a rig site in these areas depends on the intervention to the land that has already been modified, but that can affect the air quality or water bodies used for residents on the vicinity or by the wild local species.
- Low: are urban industrial lands, sandy areas other than beaches, strip mines quarries and gravel pits. Since these areas are already highly modified by anthropic intervention, the environmental impact due to O&G practices is considered lower than in natural wild lands or water bodies.

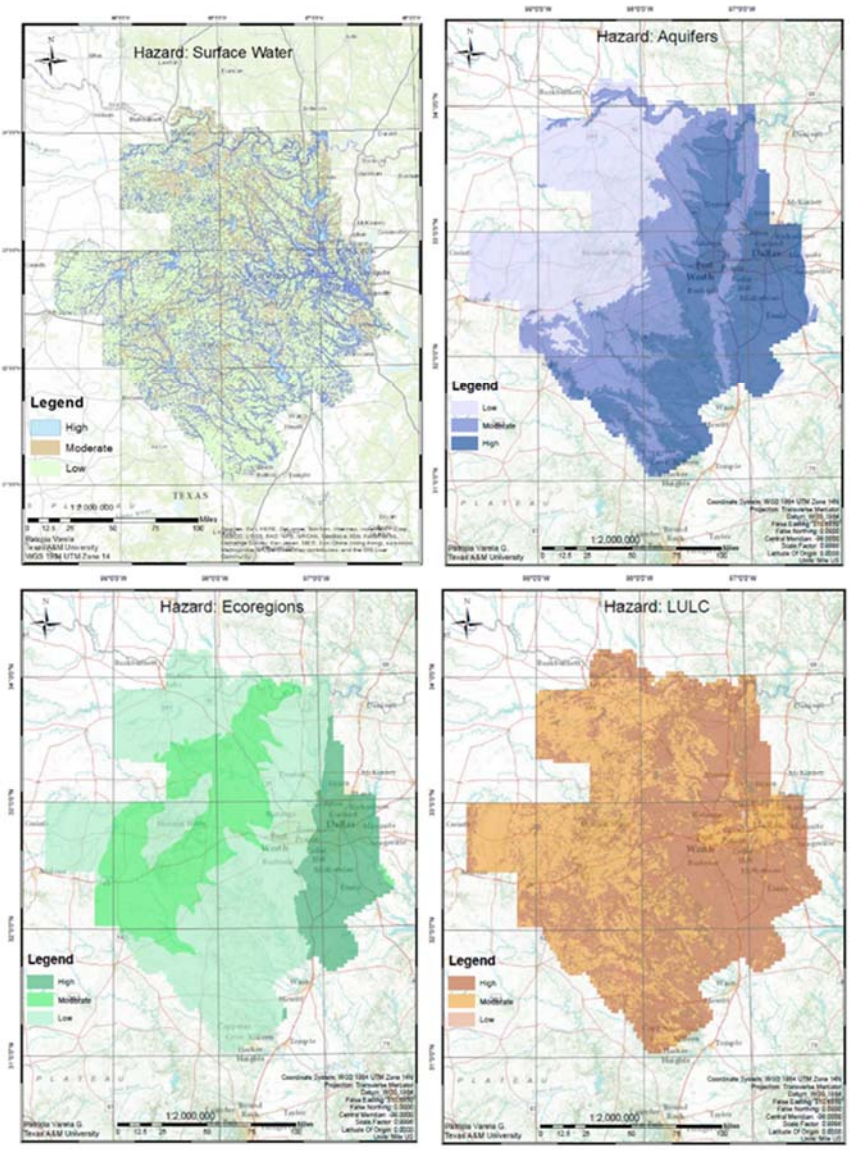

Fig 2.7 Maps of Parent Nodes. Initial condition of threat intensity levels.

Results

As a preliminary approach for illustrating the applicability of the *BN+GIS* tool, the model was implemented using a grid size of 5 km and a buffer sampling radius of 10 km (as illustrated in Fig. 3b). However, any combination of these parameters can be used by the

user through an interactive window launched from ArcMap's toolbox. The fixed probability of *ES* to be used during the diagnostic analysis ($P'(x_n)$ in Eq. 2), was ES_{High} = 0.2, $ES_{Moderate}$ = 0.3, and ES_{Low} = 0.5, yielding a Risk index of 0.35 (Eq. 2.3).

Prognosis

The four parent nodes have a visible and important impact on the patterns observed in the prognosis maps for the *ES* node. The influence of aquifers and ecoregions input maps show marked elongated clusters northeastward that can be observed on the three *ES* maps and in the risk index map (Fig. 8). The scattered appearance of *W* and *L* maps gives the results a more disperse pattern than the observed on the highly clustered maps *A* and *E*. Some of the most important lakes in the surface water bodies' map are delimitating a local increase of the risk index. Since the *ES* maps sum to one, it can be seen that the areas where the ES_{Low} map present higher probabilities, ES_{High} depicts lower probability values, while the ES_{Mod} map complements the two extremes.

The risk map (Fig. 2.8 - bottom right) shows an important influence from the input variables, as a result of the implementation of the utility function (Eq. 2.3) from the *ES* distribution. Given the occurrence of a triggering event, the areas with risk indexes ranging between 0.8 and 1.0 are located at the eastern extreme of the Barnett Shale. Its lateral extension is approximately 60 km wide by 140 km long, occupying the settlements of east Dallas, Lancaster, Ennis, Midlothian, Ennis, Milford, Itasca, north Hillsboro and Hubbard. This area coincides with a cluster of major rivers, a major aquifer outcrop, the most sensitive prairies, abundant lakes and cropland zones. The highest risk index value is 0.88 at the Lake Ray Hubbard, and the intensity of the risk is dissipated westward, reaching the

lowest intervals in the northern and western sections of the Barnett Shale counties (Albany and Lueders). The areas with the lowest risk indexes correspond to zones where the surface water is not abundant, aquifers are absent, the ecoregions are mostly semi-arid prairies, and the *L* variable is mostly composed by moderate hazard state rangelands.

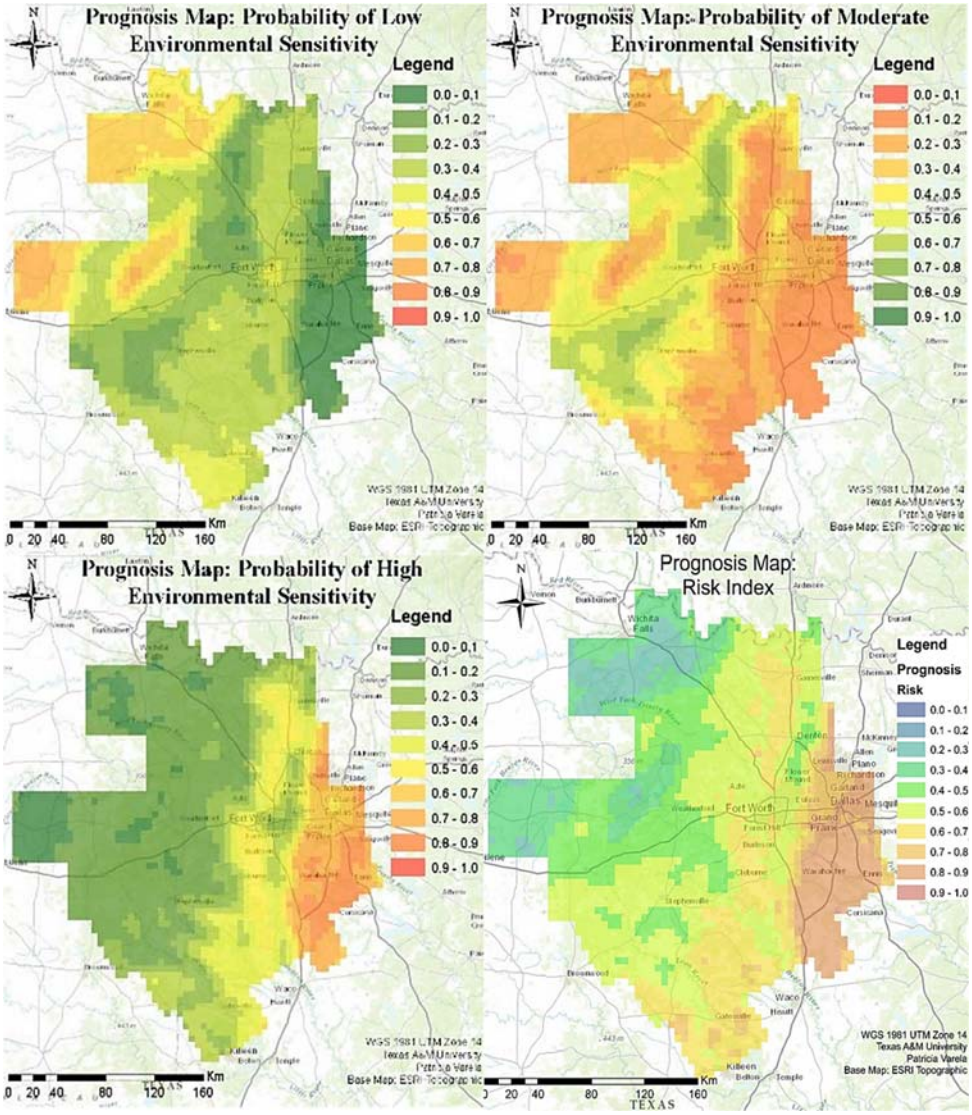

Fig 2.8 Result Maps of Prognostic Analysis.

Diagnosis

The results of this diagnostic analysis are 12 maps (Figs. 2.9 and 2.10) representing the updated probability of the four parent nodes (hazard) given a prescribed state of risk of 0.35. The diagnosis analysis indicates that the variability of the fixed risk index does not affect the general clustering or patterns of the parent nodes. However, the transition zones between hazard levels (high – moderate - low) are the most sensitive, showing updated values different from the initial parent node's states. This is observed by contrasting the original and updated maps of less clustered maps such as surface water and land use/land cover with maximized transition zones between node's classes. Conversely, sites 100% within a class produce the same probability distribution than before the diagnostic analysis. This effect is more evident for largely clustered parent nodes such as aquifers and ecoregions, where little differences can be observed between the updated maps and the original conditions. These observations lead to deduce that the diagnostic reasoning's results are sensitive to the clustering patterns of the parents' maps. The implications of this observed relationship for diagnostic analysis implies that management decisions made to improve the current state of risk using the proposed methodology are going to have a higher influence in transition zones between the node's states.

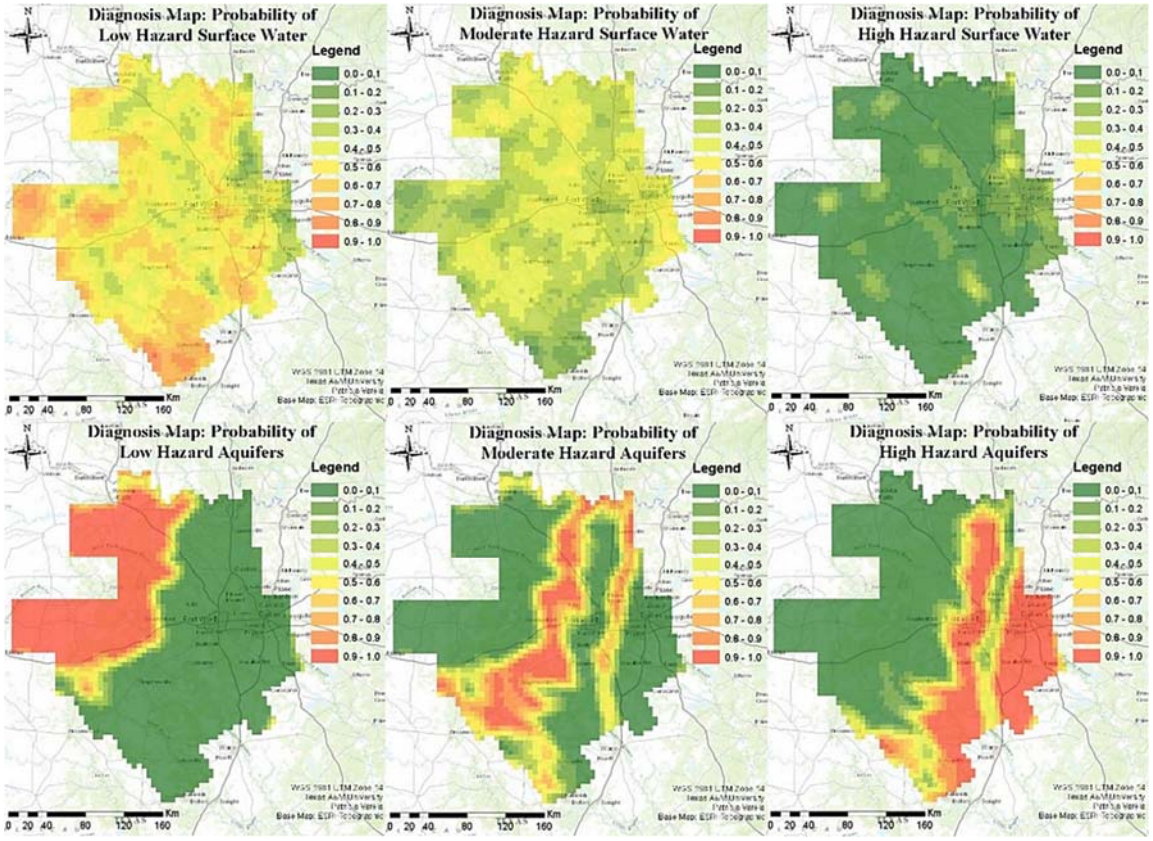

Fig 2.9 Result maps of diagnostic analysis. Updated probability of Surface Water (top) and Aquifers (bottom) hazards.

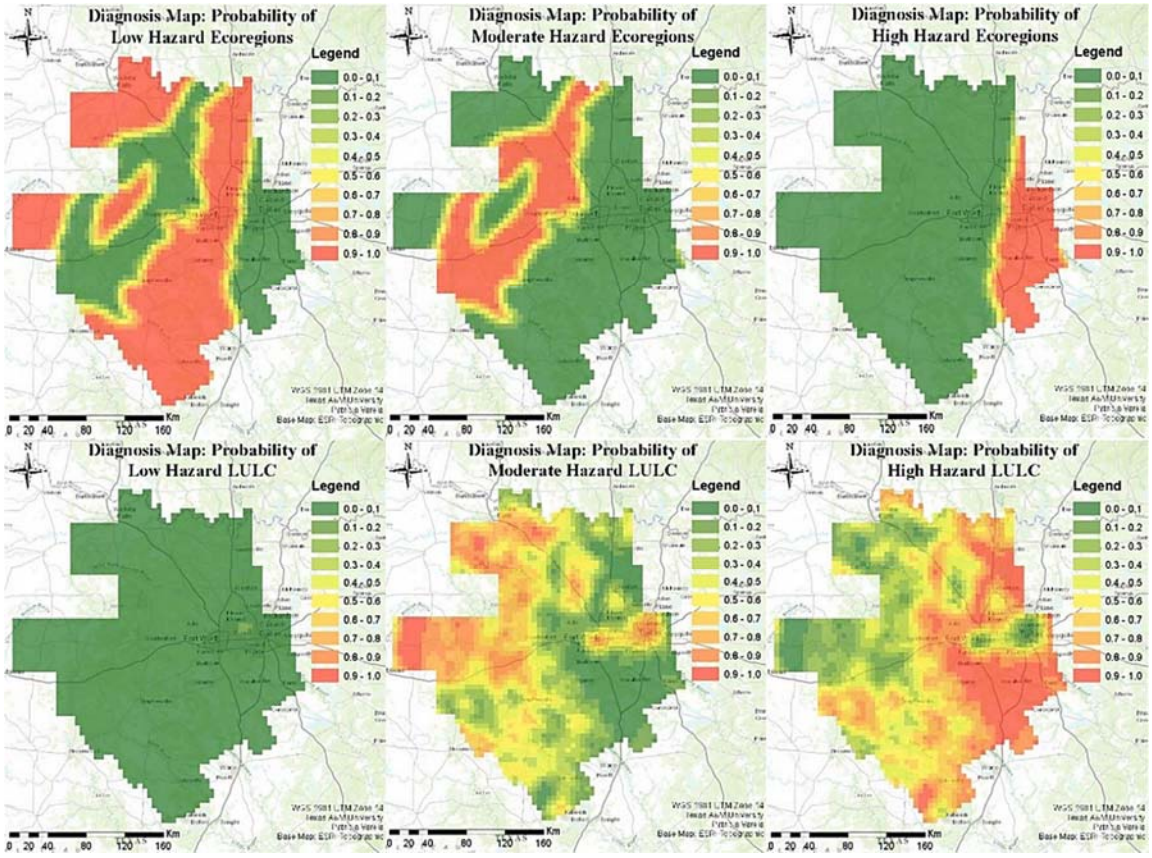

Fig 2.10 Result maps of diagnostic analysis. Updated probability of Ecoregions (top) and Land Use/Land Cover (bottom) hazards.

Analysis and Discussion

The use of the proposed *BN+GIS* methodology is designed to facilitate the decision making process based on a probabilistic assessment of the risk. The results obtained by the proposed benchmark model represents a symbolic magnitude of the environmental risk that has been constrained between 0 and 1. In a temporal stand, this analysis can be performed prior to the development of a specific project to predict future scenarios that can help with the engineering design for vulnerability mitigation and improved reliability. However, when this analysis is made posterior to the development of a project, this tool

can provide a quantification of the present state of risk that can be used for monitoring, maintenance planning or remediation purposes.

A posteriori analysis of the state of risk of the Barnett Shale's well placements was performed with production data gathered from the DrillingInfo (2015) online repository between January 2000 and January 2015 in shapefile format. The selected wells from this search were targeting the Barnett Shale Formation in any of the following categories: active permit, gas producer, oil producer, injection well or permitted oil and gas well. They sum to a total of 20,017 wells, and their location was contrasted with the risk index map (Fig. 2.11). It is observed that given the occurrence of a triggering event less than 1% of the well placements are located on a risk index zone of less than 0.3; 2% are between 0.3 and 0.4; 7% are within 0.4 and 0.5; 53% are in the 0.5 and 0.6 range; 34% are between 0.6 and 0.7; and 4% present a risk index higher than 0.7. These results show that 87% of the wells present a risk index between 0.5 and 0.7, distinguishing a Gaussian behavior on the frequency plot with mean risk index of 0.58 and a standard deviation of 0.07.

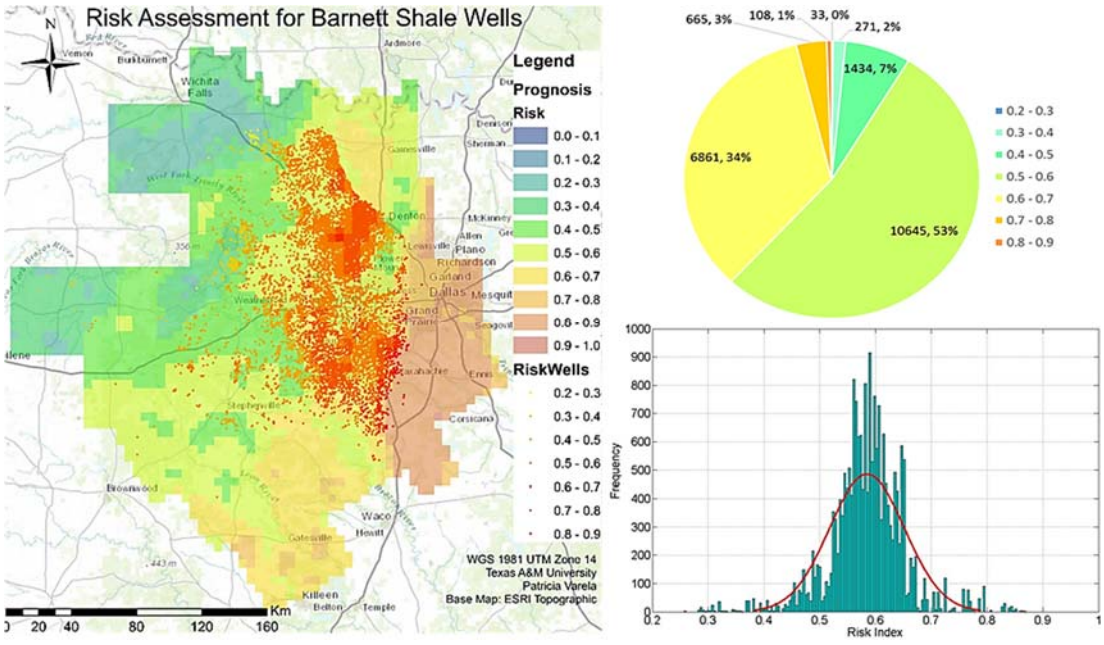

Fig 2.11 Location of production wells and their correspondent Risk index. The pie diagram (top right) shows the proportion of the Risk index for the production wells (left). A frequency histogram of the risk index of production wells (bottom right) is modeled with a normal distribution with a mean of 0.58.

The diagnostic analysis provided a visualization of the updated probabilistic scenarios of the hazards (parent nodes) for a risk index fixed by the user. With this tool, decision makers can identify the well placements that can be intervened with sustainable vulnerability management practices. Likewise, learning about the required initial conditions necessary to achieve a specific risk value contributes to an improved management of the engineering design of new site developments.

The Tobler's first law of geography, which states that closer objects are more related to each other than distant objects (Tobler 1970), is a principle that addresses the natural spatial similarities between geographical attributes. The sampling methodology proposed in this study computes a marginal probability at each individual grid element, and it is

inferred that the overlapping effect between neighboring sampling buffers accounts for Tobler's law. This overlapping effect provides a spatial dependency that can be quantified with a parametrical sensitivity analysis of the results.

The grid size used to discretize the study area represents a spatial simplification made to optimize the computational time of the script and to provide a global visualization of the environmental risk. However, as an epistemic uncertainty, this effect can be reduced by defining a grid with a higher resolution to the cost of larger computational times. In such a case, the resolution of the proposed grid should not be finer than the resolution of the maps used to define the parent nodes.

Oreskes et al. (1994) discusses that a model, which can be validated, "does not contain known or detectable flaws and is internally consistent" (p. 642). Hence, if the model follows a logical sequence of thoughts then it can be validated. Although some assumptions were made to simplify the model, the reasoning behind the BN used in this work follows a logical sequence of cause and effect, given the natural dependencies of the processes addressed. Additionally, the authors agree that the definition of the hazards for the parent nodes also follow a coherent reasoning. Therefore, this benchmark model can be validated by an expert granted that the results are interpreted as an illustration of the joint state of evidence provided by the selected input variables.

The compatibility between Python 2.6 and ArcGIS (ESRI 2012) provided an important connection between Bayesian Networks and GIS. This compatibility acted as a bridge to link the spatial data with the Bayesian probabilistic method. However, the code was designed so that the geoprocessor (an object that executes ArcMap's toolbox) was used

outside the section that loops through all of the 2,360 grid elements in this study case. This measure was implemented given that the process tended to delay more time to complete each time the geoprocess was repeated.

Conclusions

The benchmark Bayesian Network model proposed in this study was able to recreate multiple environmental risk scenarios following a probabilistic approach in a spatial domain due to the potential occurrence of a triggering event related to O&G infrastructure installation and operations. When this analysis is performed prior to the design of a well development, these maps can be used to find the most suitable place to drill and operate, based on the variables provided by the model. If the analysis is made a posteriori to the development of a site, this tool can aid with the risk quantification of the existent infrastructure, which can be used for monitoring design, maintenance or reduction of the site's vulnerability through risk management practices. One of the most important contributions of this work is its potential application for economic or societal risk assessment. For instance, the same methodology proposed in this work can be implemented using spatially sensitive societal and economic variables that can also converge into social and economic risk indexes, respectively. Furthermore, these potential assessments can also be used for the evaluation of a robust risk index that unifies the environmental, societal and economic conditions using *BN+GIS*. Considering all the potential applications of the proposed methodology and its implementation for prognostic

and diagnostic analysis, it is considered that this study provides a systematic and comprehensive tool for improved decision-making and risk assessment.

The surface water bodies, aquifers, ecoregions and land use / land cover maps used as input variables of the proposed model provided satisfactory results that were capable of assessing the Environmental Sensibility of the Barnett Shale counties. The maps produced by *BN+GIS* are symbolic representations of the environmental risk based in the geographical distribution of the selected hazard's features. Even though the results are symbolic and is not possible to physically measure risk on the field, the definition of the conceptual model and the methodology followed lineaments suggested in the literature for best BN modeling practices and it can be validated by experts.

The risk assessment methodology provided an appropriate tool to be coupled with the proposed BN, where the parent nodes are defined as hazards. The conditional probability table of the *ES* served as the vulnerability of the modelled system, and the utility function provided a dimension of the consequences. When these results were compared to the actual location of the well placements in the Barnett Shale Play, it was possible to quantify the state of risk of the existent infrastructure given the potential occurrence of a triggering event.

Prognosis and diagnosis types of reasoning were implemented in this study, resulting in a set of four maps when solving the forward problem and 12 maps when solving the inverse problem. The resulting maps showed patterns, clustering and geographical patterns that are visibly inherited from the parent nodes. The risk index fixed during the diagnostic analysis (fixing the *ES* node) does not significantly impact the general shape of the updated

hazard maps. However, those areas showing a visible effect on the diagnosis results are the transition zones between node's states of each parent node. Therefore, when this type of diagnostic analysis is made prior to the development of a site, land management decisions are going to have a higher impact on the mitigation of the risk if these practices are implemented in transition zones between the parent node's states.

As a preliminary approach, the proposed methodology captured different elements of risk assessment, but further parametrical analysis is required to better understand the effect of this type of modeling on the decision-making process.

CHAPTER III

PARAMETRIC SENSITIVITY ANALYSIS OF ENVIRONMENTAL RISK MAPPING FOR THE BARNETT SHALE PLAY

Introduction

A parametrical sensitivity analysis is critical for model validation, and can be used to identify variables that require further investigation for epistemic uncertainty reduction, model simplification, or estimation of correlation structures between model's inputs and outputs (Hamby 1994). In this paper, a parametric sensibility analysis was conducted as a statistical approach to maximize the number and quality of inferences derived from the user-defined parameters of a Bayesian network (BN) model coupled with GIS, referred by Varela (2013) as *BN+GIS*. This model was defined to map the environmental risk due to oil and gas (O&G) site developments. Coupling BN, risk assessment, and GIS enables an efficient synthesis of spatial evidence that can be used for improved and informative decision-making (Varela 2013; Medina-Cetina et al. 2017). The proof-of-concept network proposed in their work uses maps classified in levels of threat intensity to aquifers (*A*), surface water bodies (*W*), ecoregions (*E*) and land use/land cover (*L*) as model's inputs. These input variables are denoted in the BN nomenclature as **parent** nodes (Korb and Nicholson 2010). The joint probability distribution of these four parent nodes are represented by a **child** node that embodies the environmental sensibility (*ES*) of a specific site. The probability of *ES* is used to assess a risk index (*RI*) symbolizing the desirability

of the model's outputs, and allows the modeler to map the risk given the occurrence of a triggering event that could jeopardize the integrity of the parent nodes. The implementation of this BN within a risk assessment framework consisted on (1) quantifying the probability of a **threat** intensity embodied by the parent nodes, which is known as **hazard** (UNDRO 1979), (2) considering the conditional probability between parent and child nodes as a measure of the **vulnerability**, and (3) using a utility function to represent the **risk** in a unit that can be used for decision-making purposes (UNDRO 1979, Medina-Cetina and Nadim 2008, Varela 2013). The spatial sampling methodology used to define the marginal probabilities of the parent nodes depends upon the modeler's choice of sample interval (grid size-*g*) and realization's plot size (buffer distance-*b*). The combination of these two parameters can influence the *BN+GIS* results, and affect the significance of the decisions derived from the modeling process. Given the ability of BNs to integrate different sources of information with different resolution and accuracy, the spatial sampling methodology could be influenced by the heterogeneity of the spatial observations. Hence, quantifying the spatial correlation structure of the risk maps generated by *BN+GIS* can help the decision-maker to select adequate parameters to populate the most informative maps.

BNs are defined as directed acyclic graphs representing the causal relationship of variables or nodes connected by arcs. Each node denotes the probability distribution of a random discrete or continuous variable, and the arcs represent the conditional probabilities relating the variables. Bayes' theorem of conditional probability is used to propagate the information across the network using two types of reasoning: (1) forward modeling,

referred in this work as prognosis, and (2) inverse modeling, denoted as diagnosis (Korb and Nicholson 2010). The prognostic type of reasoning (1) uses the evidence of the parent nodes to estimate the joint probability distribution of the child nodes, mapping the influence of the causes on the effects. Conversely, the diagnostic modeling (2) is used to fix an anticipated condition of a child node to update the probability of the parent nodes, estimating the probable causes of a prescribed effect (Korb and Nicholson 2010; Medina-Cetina et al. 2017). Numerous authors concur on their acceptance of BNs as a suitable tool for risk assessment and decision-making due to its capability to integrate different sources of evidence such as data, model predictions, and expert's educated beliefs considering the causal relationship between variables (Kiiveri and Caccetta 1998; Grêt-Regamey and Straub 2006; Medina-Cetina and Nadim 2008, Liu et. al. 2015).

The BN examined in this work is designed to estimate *RI* values based on the spatial configuration of the input maps in prognostic modeling. Additionally, *BN+GIS* also performs a diagnostic analysis designed as a policy-making tool to assess the required initial conditions necessary to achieve a prescribed *RI*. Expressly, fixing the probability of the child node *ES* and solving the inverse problem, the model returns the **updated** probabilities of the parent nodes *A*, *W*, *E*, and *L* (hazard maps). This work aims to estimate the spatial influence of the prescribed probability of the child node on the updated parent nodes during the diagnostic modeling, and to understand the effect on the uniformity of that distribution on the updated results. Conditioning the diagnostic tool to a diverse set of policies allows an understanding of the model's response to different scenarios that can be used to improve the state of knowledge of stakeholders.

Given these considerations, the objectives of this study are: (1) to identify the parameters that contribute to higher variability on the environmental risk maps, (2) to identify the conditions that lead to its increased uncertainty, (3) to define a methodology to be used by future *BN+GIS* users to select suitable spatial sampling parameters, and (4) to analyze the effect of the selection of prescribed environmental risk indexes on the updated maps of the parent nodes (risk threats), and its significance on the decision-making process. To achieve these goals, the authors consider that a factorial experimental design can be utilized to assess the sensitivity of *BN+GIS* given a set of values for *g* and *b*, and a set of probability distributions of *ES*. It is hypothesized that using *BN+GIS* with an optimal combination of spatial sampling parameters allows the extraction of substantial information that can increase the confidence on the inferences derived from the results. A better understanding of the policy-making mechanism (diagnosis) used in this model and its limitations is regarded by the authors as a valuable and important aspect to consider for maximizing the applicability of the updated hazard maps for informed decision-making.

Scientific inference is linked to different types of uncertainty. Aleatoric uncertainties on *BN+GIS* are derived from the irreducible and inherent random nature of the input variables, while epistemic uncertainties could potentially be mitigated or managed at different stages of the modeling process (Helton et al. 2006; Matthies 2007). The selection of quality data, the expert's model validation, and the use of calibration methods to assess the influence of each input variable on the results are considered by the authors as acceptable mechanisms to reduce the epistemic sources of uncertainty. Yet, this work focuses specifically on the identification and reduction of the uncertainties derived from

the choice of *b*, *g* and *ES* as an approach to enhance the understanding of the methodology proposed by Medina-Cetina et al. (2017).

Hamby (1994) summarized a comprehensive description of methods used for sensitivity analysis, such as differential sensitivity, one-at-a-time sensitivity, factorial design, sensitivity index, and other approaches that include the use of random sampling techniques. These methods rely on differential analysis to estimate the variabilities of the model's responses given the influence of the selected inputs, according to a specific type of experimental design. Saltelli et al. (2000) provided important contributions on the use of sensitivity analyses as part of the modeling process, discussing the use of variance-based techniques such as extended Fourier Amplitude Sensitivity Testing (FAST), and the method of Sobol' (Saltelli et al, 1999; Sobol' 1993). They suggest that these type of approaches offer advantages such as taking into consideration the probability density function of the inputs, and the independence of the sensitivity technique to the model's structure. The implementation of these random techniques often requires the use of Monte Carlo methods that are considered to elevate the dimensionality of the analysis that can be particularly useful for modeling the behavior of multiple continuous variables. For this particular study case, the authors consider that a basic approach such as a factorial experimental design and a differential analysis can provide simple answers to solve the proposed uncertainty problem. Consequentially, the set of tools available in most GIS software packages can be used to map these uncertainties across the spatial domain and observe patterns and clusters of higher variance.

Multiple sensitivity analyses can be found in the literature for modeling natural processes in a spatial domain. Daniel McKenney (1999) conducted a one-at-a-time sensitivity analysis technique of a spatially distributed solar radiation model in Canada to estimate the parameters with the highest influence on the model's outputs. Among a set of five variables, it was possible to conclude that the amount of effort invested on defining atmospheric parameters such as cloudiness and sunshine fraction (in relation to hours of sunlight per day) should be more thorough than for other parameters of the model. Bou-Zeid and El-Fadel (2004) performed a sensitivity analysis to identify the most significant parameters necessary for the assessment of leachate migration and transport from a landfill site to the nearest groundwater source. That study suggested that dispersivity and aquifer hydraulic conductivity are among the most important parameters affecting their modelled transport mechanism. Estimates of evapotranspiration and pan evaporation on the Yangtze River were mapped by Xu et al. (2006), followed by an analysis of seven cases of varying meteorological variables, concluding that the model is most sensitive to relative humidity and net total radiation. In such cases, the implementation of an experimental design that compares the model predictions for a set varying input parameters was a successful approach for estimating the most sensitive variables. However, little effort have been made on mapping the uncertainty and discussing the conditions that lead to higher sensitivity of a variable across the spatial domain.

The implementation of any type of sensitivity analysis on BNs that have been scaled to a spatial domain using GIS is a practice that is sparsely found in the literature. Some of these efforts include the use of software based entropy reduction analysis (Smith et al.

2007 and McCloskey et al. 2011), and analysis of variance (Stelzenmüller et al. 2010). In these cases, the sensitivity analysis was oriented to study the influence of the network's conditional probability tables on the outputs, and not to examine the method used to extract spatial information to populate the model.

Efforts to develop analytical methods to compute sensitivity values on BNs (Spiegelhalter and Lauritzen 1990; Laskey 1995; Castillo et al. 1997, Coupé and Van Der Gaag 2002) have focused on the influence of the conditional probabilities and the probabilities of parent nodes on the model's outputs. These methods include uncertainty quantification using a Bayesian statistical paradigm (Spiegelhalter and Lauritzen 1990) and symbolic propagation methods where conditional probabilities can be expressed as ratios of a polynomial function (Castillo et al. 1997). The use of algebraic structures testing the methods to define marginal probabilities, their dependence, and their joint distributions are focused on understanding the propagation of uncertainty across the model introduced by the combination of expert's opinions, model predictions and samples from a user-defined dataset. More recently, evolutionary algorithms were employed to simplify and optimize BNs by excluding connectors or dependencies, and therefore avoiding biases or errors on the definition of large conditional probability tables (Aitkenhead and Aalders 2009). The variety of sensitivity analysis methods found in the literature suggests that a well-documented and a comprehensive understanding of the influence of marginal and conditional probabilities on the results exists. It is important to highlight that this work is not aimed to study the effect of the uncertainties derived from the marginal and conditional probability distributions, but to assess the effect of the user-defined parameters of *BN+GIS*

on the results. In other words, this work focuses on the sensitivity of the results to the spatial sampling methodology and to the diagnostic reasoning proposed during the coupling process between BN and GIS, as suggested by Medina-Cetina et al. (2017).

BN+GIS

The BN model illustrated in Fig. 3.1 was implemented by Medina-Cetina et al. (2017) as the simplest conceptual model used to assess the environmental risk of the Barnett Shale Play, Texas, given the occurrence of triggering events such as hydrocarbon spills or failure of the borehole casing. The study case was selected due to the intensive O&G development in the area and the importance in the local and national economy of the Barnett Shale Formation (Montgomery et al. 2005). A risk assessment framework commonly used in engineering and described by the Office of the United Nations Disaster Relief Organization (UNDRO 1979) was utilized to design the model. Hence, input variables of the network are classified based on the **threat intensity** to A, W, E and L (as seen in Fig. 3.1), the conditional probability distribution as a measure of the **vulnerability**, and a utility function as a convolution of probability values to a symbolic **risk** index quantifying the desirability of the consequences (UNDRO 1979; Medina et al. 2017). This section summarizes the methodology used by Medina-Cetina et al. (2017) to sample the threat intensity maps in order to retrieve marginal probability distributions from the proposed BN's parent nodes.

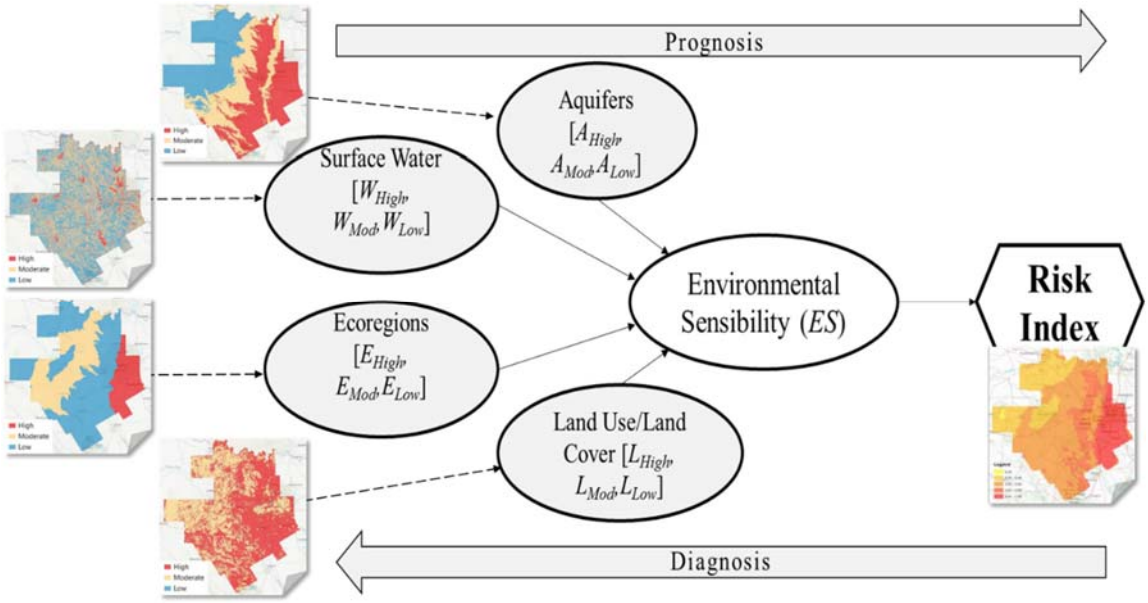

Fig 3.1 BN model for environmental risk assessment.

BN+GIS uses a systematic sampling methodology to extract the spatial information from the threat intensity attributes (low, moderate and high) of the input maps. This information is translated into marginal probability distributions to populate the BN, yielding a quantification of the hazard (UNDRO 1979) to each variable per realization (Medina et al. 2017). *BN+GIS* creates a grid across the study area using square polygons that serve as discrete elements for the computation of the model to complete this task. Let Θ represent the spatial population to be sampled, thus $\Theta = \sum_{i=1}^{n}(polygon\ area)_i$. The distance between centroids of the grid elements serve as sampling interval, and it is denoted as *g*. A buffer of radius *b* around each centroid is used as plot sample to quantify the proportion of each threat intensity class for the four input maps. This proportion is used to populate the marginal probability distributions of the parent nodes in the proposed

BN model, which are posteriorly used by *BN+GIS* script to loop through each *g* and compute a prognostic estimate of *ES* and *RI*. (Medina-Cetina et al. 2017).

The script is also equipped with the ability to perform diagnostic analysis by introducing a user-defined probability of *ES* to back-propagate a fixed desired condition of the posterior and update the state of the parent nodes across Θ. The results of diagnostic *BN+GIS* are used as a policy-making tool to assess the potential original conditions that caused the selected posterior distribution of the model. The selection of the posterior fixed distribution of *ES* represents another parameter used by *BN+GIS* before starting the looping process through Θ, and computes the updated probabilities of the threat intensity to *A*, *W*, *E* and *L* to be high, moderate or low (Medina-Cetina et al. 2017).

Experimental Design

Spatial Sampling Experiment

A factorial experimental design was conducted to test the spatial sampling methodology aiming to achieve the lowest variance and maximizing the significance of the inferences derived from *BN+GIS*. This type of analysis is a one-at-a-time type of experiment that consists on the selection of a number of values for sampling parameters *g* and *b*, and the examination of the results for all possible combinations (Hamby 1994; Hashemi et al. 2000; Franchini et al. 2000). The experimental design used in this work consisted on the use of six grid sizes (g = 2, 4, 6, 8, 10, and 12 km) and six buffer distances (b = 2, 4, 6, 8, 10, and 12 km). This configuration yields a total of $6^2 = 36$ maps, allowing the observation

of the variation of the *RI* across the selected study area. Note that for larger grid sizes, fewer elements are required to cover Θ, which results in maps with a number of samples (n) inversely proportional to g. A differential analysis using a sensitivity coefficient ($\emptyset$) and a sensitivity index (SI) was implemented to quantify the rate of change of the RI given the variability of b and g (Hamby 1994). The coefficient $\emptyset$ provides a measurement of the variability of the results with respect to the ratio of change of the input parameters, which can be expressed as $\emptyset = \frac{|\partial RI|}{\partial g,b}$. The SI quantifies the difference of the outputs with respect to the maximum and minimum values that can be obtained from all combinations, which can be expressed as $SI_i = \frac{RI_{max_i} - RI_{min_i}}{RI_{max_i}}$, where i accounts for all 36 combinations of g and b (modified from Hamby 1994).

As seen in Fig. 3.2, the relationship between g and b can influence the *RI* estimates and the associated epistemic uncertainty observed across Θ. If b is smaller than half of the grid element's diagonal ($b \leq \frac{\sqrt{2}}{2} g$), then omitted areas are not sampled within each grid element's realization (Fig. 3.2, left). Wang et al. (2012) noted that the uncertainty of the sampling methodology related to the random nature of a given sampling site could be reduced when the full population is surveyed. A 100% coverage of Θ is reached when the grid element is inscribed within the plot area ($b \geq \frac{\sqrt{2}}{2} g$), yielding overlapping areas between contiguous grid elements (Fig. 3.2, right). However, the plot area could potentially get large enough to cover the entire population, in which case Θ would be fully sampled for every grid element, and the variance would be zero. This extreme case would diminish the uncertainty derived from the randomness of the spatial configuration of the

input maps, but would widely overestimate the influence of the spatial relationship between two random locations.

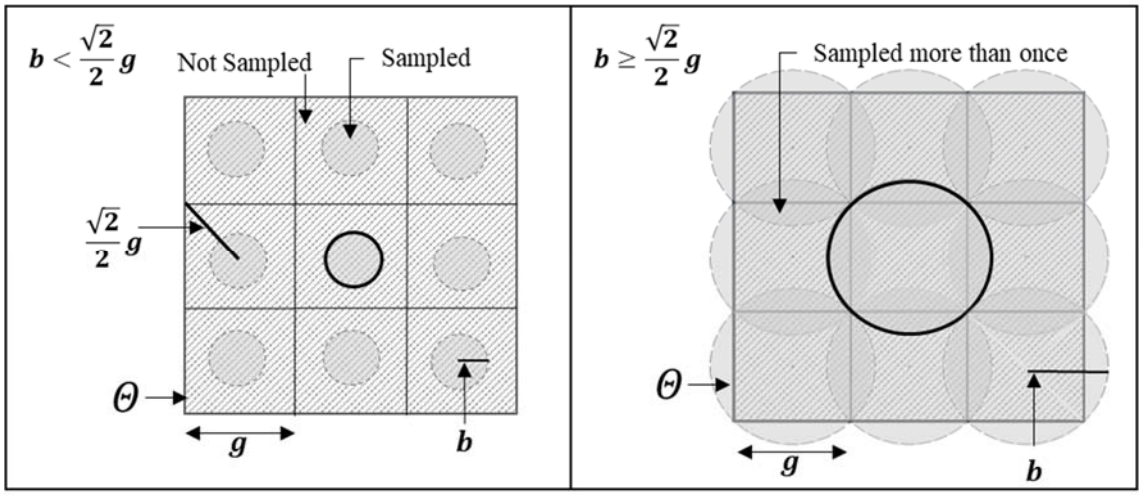

Fig 3.2 Relationship between parameters g and b on sampling methodology.

This spatial relationship principle is commonly referred as Tobler's first law of geography (1970), which states that objects located at a closer proximity are more similar than objects located further apart. Given the proximal spatial relationship of the *BN+GIS* results, a spatial autocorrelation analysis of the risk index maps was conducted to estimate the optimum distance (plot size b) for all realizations in Θ. As a simple approach to assess and quantify the strength of the linear association between the output's attribute and its spatial proximity, an autocorrelation plot using Parson's correlation coefficient was examined (Haining 1991; Hauke and Kossowski 2011). Let $RI(X)$ be a vector with risk index values for all elements X in the study area. For each lag distance k at a given direction, the Pearson's correlation coefficient can be implemented using the expression

$\rho_k = \frac{COV[RI(X),RI(X+k)]}{\sigma_X \sigma_{X+k}} = \frac{E[(RI(X)-\overline{RI}(X))\times(RI(X+k)-\overline{RI}(X+k))]}{\sigma_X \sigma_{X+k}}$ (modified from Haining 1991).

Diagnosis Experiment

As an approach to assess the sensitivity of the diagnostic feature of *BN+GIS*, four probability distributions of the *ES* node and their influence on the updated maps of *A*, *W*, *E* and *L* are tested. The four conditions (C1, C2, C3 and C4) of *ES* observed in Fig. 3.3 were used. These combinations depict two opposite risk conditions (C1: *RI* = 0.2 and C4: *RI* = 0.8) and two combinations yielding a *RI* = 0.5 with different probability distributions of the *ES* variable (C2 and C3). C1 and C4 were tested to examine the impact of extreme policies on the decision making process, while C2 and C3 were selected to study the influence of different uncertainty levels on the model's inferences.

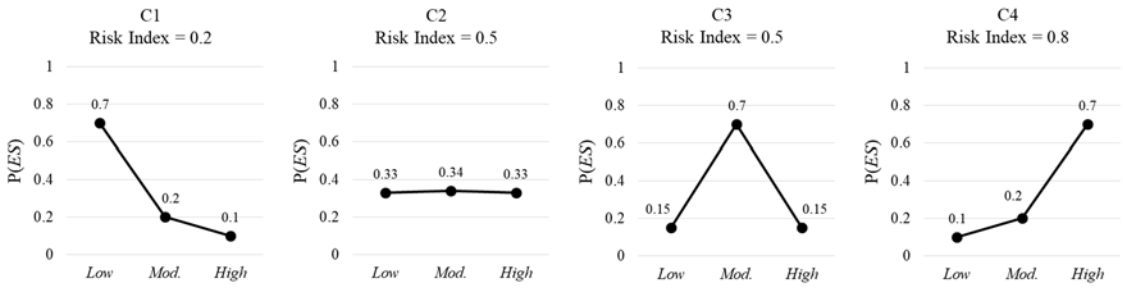

Fig 3.3 Four combinations of fixed probabilities of ES. Posterior distributions tested for inverse modeling.

Results

Spatial Sampling

The first approach to observe the influence of b and g on the output consisted on the contrast of the empirical density functions of the prognostic RI maps ($EDF = {frequency}/{n * bin\ size}$) for each combination of the experimental design with a bin size of 0.02 (Fig. 3.4). This assessment illustrates that the general trend of the output presents a consistent trimodal behavior, typically with a predominant mode around a RI value of 0.5, and two subordinated modes around 0.23 and 0.85. This behavior can be attributed to the influence of the low, moderate and high intensity states of the probabilistic input variables of the BN model. It is observed that the RI does not reach either of the extremes of the domain (0 or 1) for any of the tested b and g combinations. Empirical density functions of smaller g are observed smoother than the curves of larger grid elements, which can be attributed to the influence of larger numbers of samples (n) for a thinner grid.

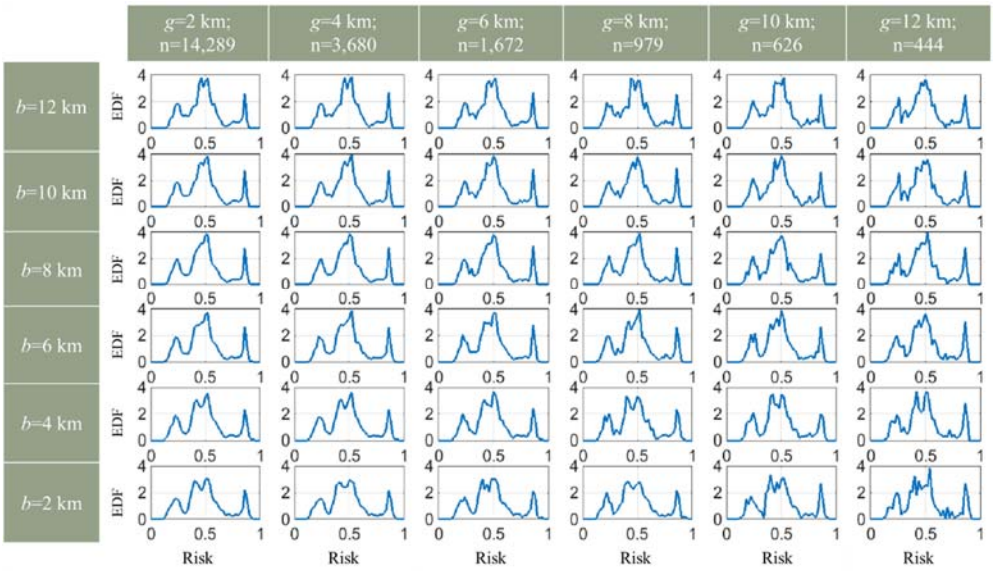

Fig 3.4 Empirical density functions (EDF) of the RI maps for each combination of g and b.

Since very little variability is observed on the behavior of the empirical density functions of all combinations of sampling intervals and plot sizes, further analysis was performed on the quantification of the first order statistics derived from this experiment. Plots of the mean and standard deviation (σ) of the *RI* values of all the elements on the study area for all b and g combinations is observed in Fig. 3.5. It is observed that the mean *RI* shows little variation with values between 0.485 and 0.489, representing a sensitivity of 0.4% of the complete risk index domain [0,1], with slightly higher values for smaller buffer sizes. The σ plot shows that the systematic sampling methodology present a higher sensitivity to the size of b than to g, and it is clearly observed that the standard deviation decreases for all tested grid sizes with larger b distances. This trend can be interpreted as a response to wider sample sizes with large overlapping areas resulting on lower overall uncertainties. Still, a slight trend of lower standard deviation values for smaller g is also observed, which

could be accredited to the influence of larger numbers of sampling points as the sampling interval decreases.

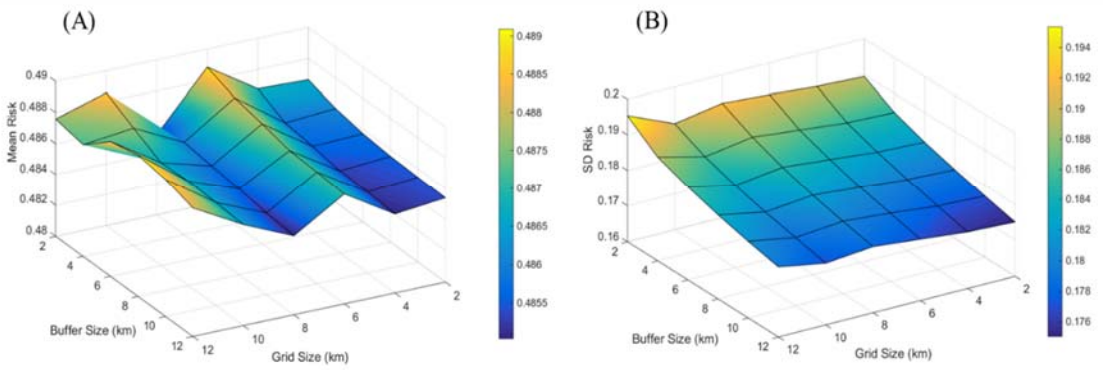

Fig 3.5 (A) Mean and (B) standard deviation of RI for 36 combinations of g and b.

The sensitivity coefficient ($\emptyset$) and sensitivity index (SI) computed during this experiment provided more information about the behavior of the model's outputs given different sampling parameters. As mentioned before, the coefficient $\emptyset$ is the ratio of change of the outputs given a change of the input parameters. Expressly, for a fixed b it is possible to compute a value of $\emptyset$ per-grid element of the RI for a set of varying values of g, such as $(b02g02 - b02g04)/2$, $(b02g02 - b02g06)/4$, and so on. Likewise, testing the sensitivity of the outputs to changes of b requires the calculation of $\emptyset$ ratios for fixed values of g. The results, shown in Fig. 6(A), display the mean values of $\emptyset$ for b and g differentials. It is observed that the range of the sensitivity coefficient shows less variation to the change of grid size than to the plot size, and that lower sensitivity coefficients are achieved as the differentials of b and g increases.

Moreover, the SI refers to the ratio of change on the range of the RI. Higher SI values are portrayed by combinations from the experimental design returning wider ranges of the

RI domain, defined between 0 and 1. The resulting *SI* for each tested combination, as observed in Fig. 6(B), shows that the range of risk index values presents a stronger dependency on b than on g. The result obtained using the smallest grid and buffer size returns the highest *SI*, hence, the combination $b02g02$ returns the most informative output given that it presents the widest range of Risk Index values.

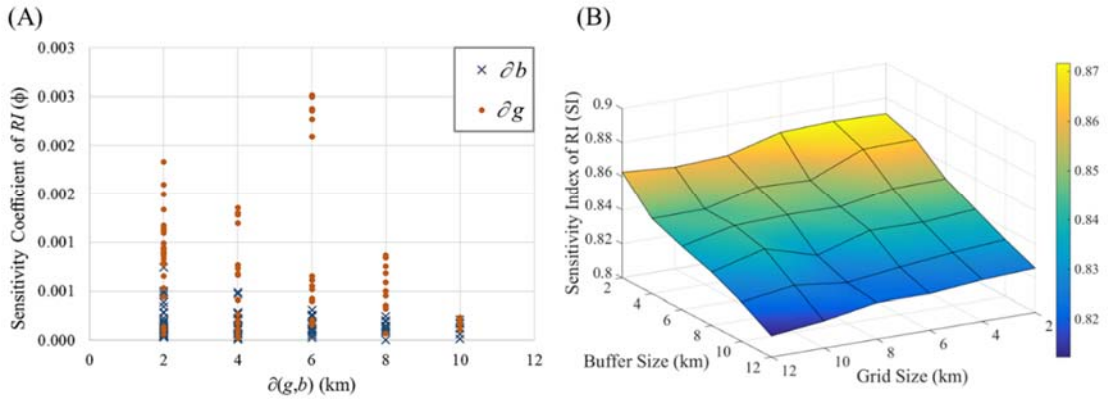

Fig 3.6 (A) Sensitivity coefficient (∅) and (B) sensitivity index (SI) of Risk Index (RI) for different sizes of g and b.

A set of maps was prepared to examine the influence of b and g on the variability of the results across the spatial domain (Fig. 3.7). Each map is the representation of the σ per spatial element of the *RI* for the 6 cases where the value of g or b remains constant (e.g. $\sigma(b02) = \sigma(b02g02,\ b02g04,\ b02g06,\ b02g08,\ b02g10$ and $b02g12)$. Comparing these results with the features observed in the input maps allows one to identify clusters of higher standard deviation values located in regions where contrasting classes of *A*, *W*, *E* and *L* are. It is also observed a decrease of the standard deviation's color intensity as the buffer size increases, which is consistent with the results observed in Fig. 3.5(B). The

observed σ values show distinctive patterns and clusters for smaller grid sizes, also following the preferential arrangement of the input variable's threat intensity classes.

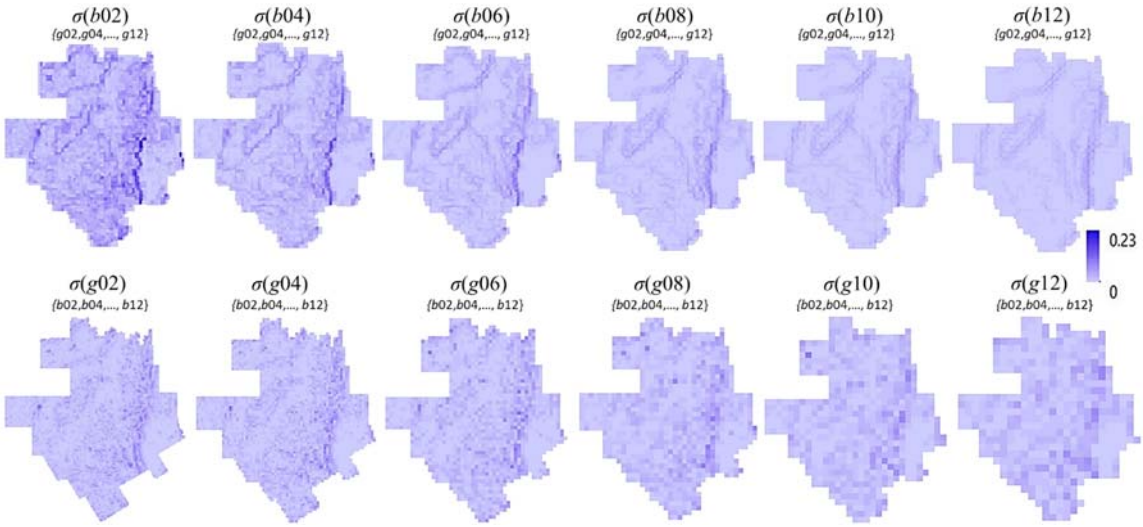

Fig 3.7 Standard deviation (σ) of RI across study area for selected sizes of g and b.

Following up with the trend suggesting that larger plot sizes imprints on the results a decrease of the uncertainties levels, a spatial autocorrelation analysis was implemented to assess the optimum distance to account for spatial relationships during the sampling process. This analysis was conducted using the smallest grid and plot size ($b02g02$) in order to maximize the spatial resolution and minimize the overlapping effect on the results. The spatial autocorrelation was determined by the computation of the Pearson's correlation coefficient in the west-east (WE) direction and north-south (NS) direction (Fig. 3.8). A curve fitting procedure was utilized to estimate the correspondent lag distance for a desired level of spatial correlation on the estimation of *RI*. The lag distance can serve the same purpose as the plot size b utilized for the spatial sampling methodology, which is directly related to the extent of a realization's area.

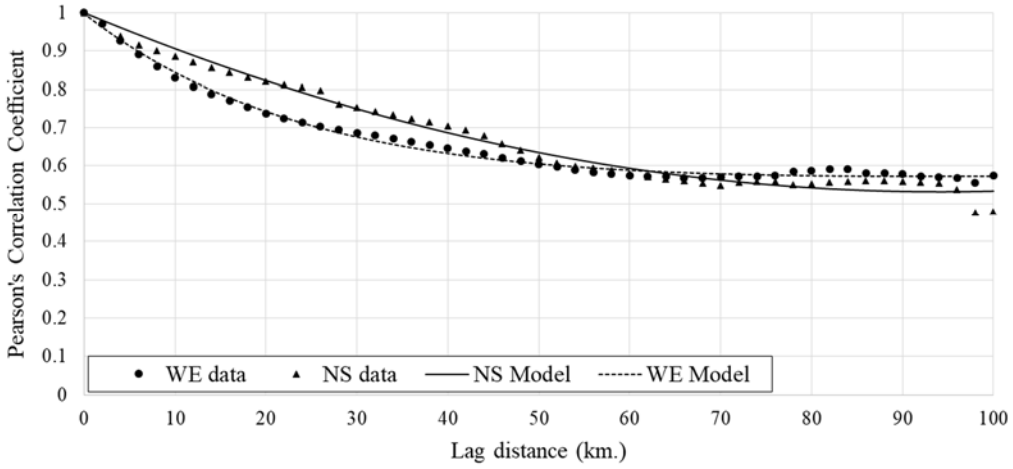

Fig 3.8 Directional Pearson's autocorrelation coefficients and fitted curve for RI map for sampling parameters b02g02.

The results of the autocorrelation analysis can be summarized in Table 3.1, which can be used by the modeler's to select the required level of spatial relationship.

Table 3.1 Pearson's correlation coefficients for NS and WE directions, for lag distances 1 to 15 km.

Lag Distance (km.)	Direction NS	Direction WE
1	0.9901	0.9794
2	0.9803	0.9618
3	0.9707	0.9449
4	0.9611	0.9286
5	0.9516	0.9130
6	0.9423	0.8981
7	0.9330	0.8837
8	0.9239	0.8699
9	0.9148	0.8567
10	0.9059	0.8440
11	0.8971	0.8319
12	0.8883	0.8202

Diagnosis

The diagnostic analysis was performed using the maximum resolution from the selected parameters of the experimental design ($g = 02$), and a NS and WE correlation of 0.91 and 0.84, respectively, equivalent to $g = 10$. A set of 12 maps is returned each time the model is executed in diagnosis, corresponding to three probabilistic states of the threat intensity levels defined to the four input variables. Testing four probability distributions (C1, C2, C3 and C4) used to propagate the diagnostic message returns a set of 48 maps. Hence, the updated condition of each input variable produces a subset of 12 maps of three threat intensity levels given the four diagnostic distributions used in this experimental design (see Fig. 3.9 to 3.12).

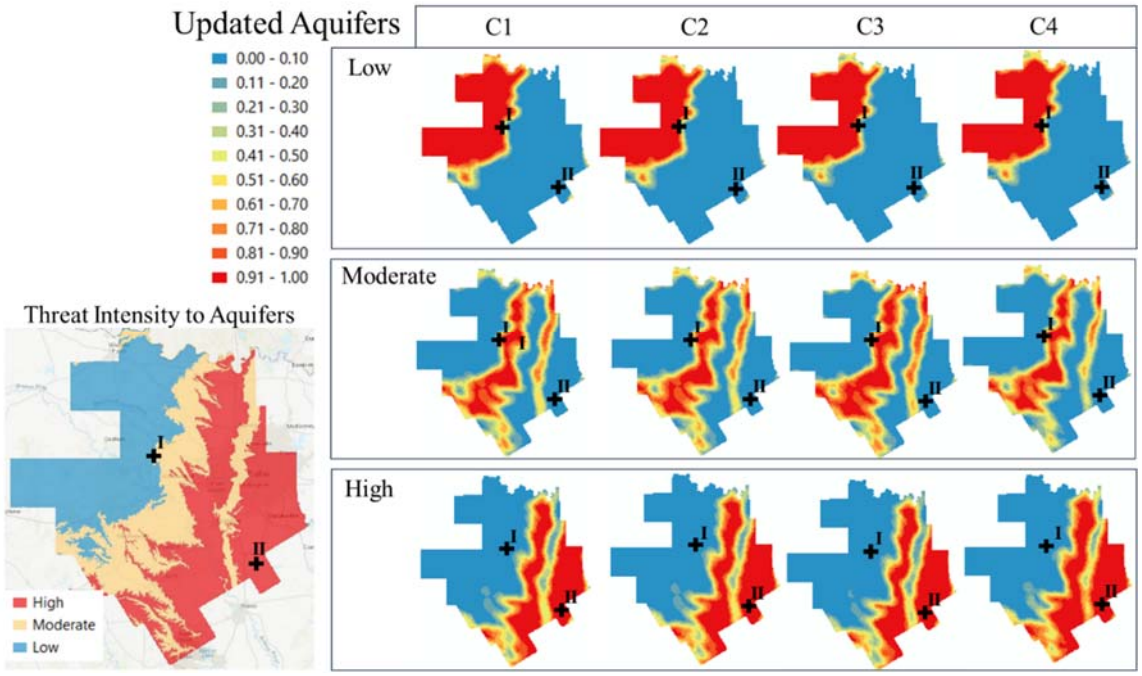

Fig 3.9 Updated hazard to *A* using fixed diagnostic messages C1, C2, C3 and C4.

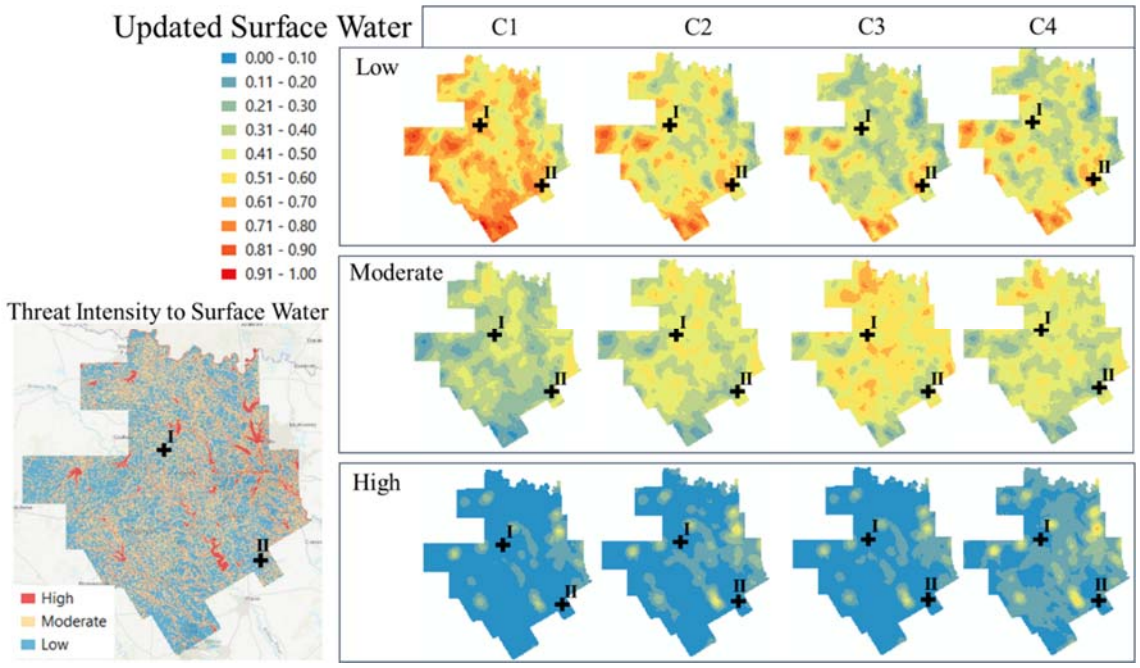

Fig 3.10 Updated hazard to *W* using fixed diagnostic messages C1, C2, C3 and C4.

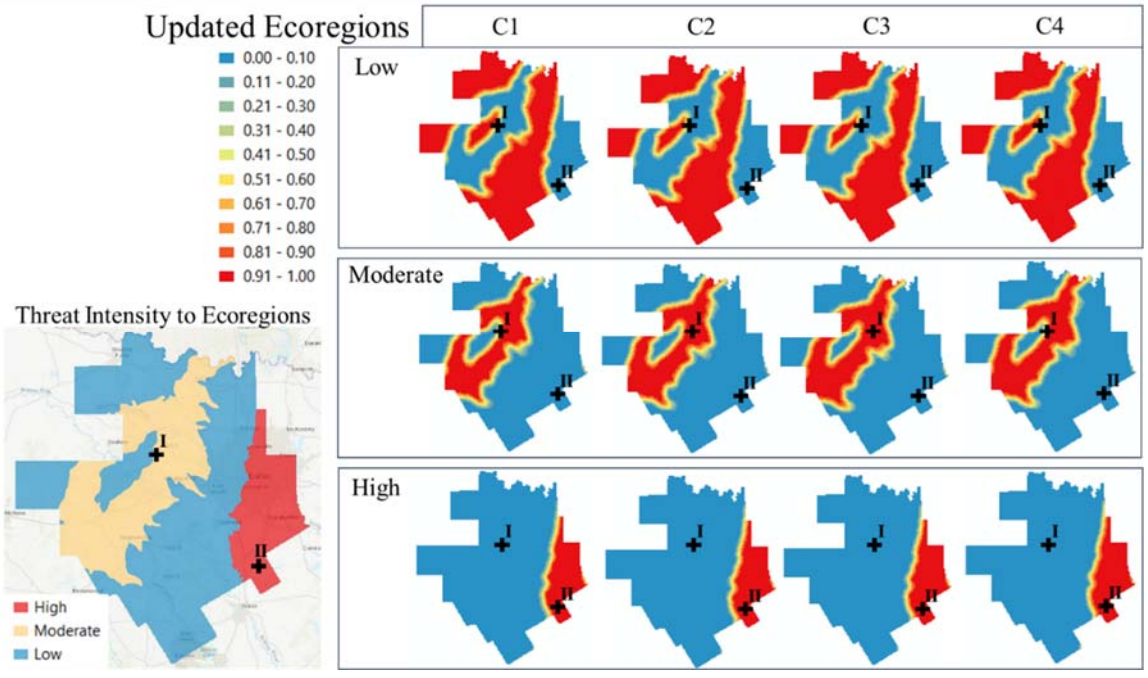

Fig 3.11 Updated hazard to *E* using fixed diagnostic messages C1, C2, C3 and C4.

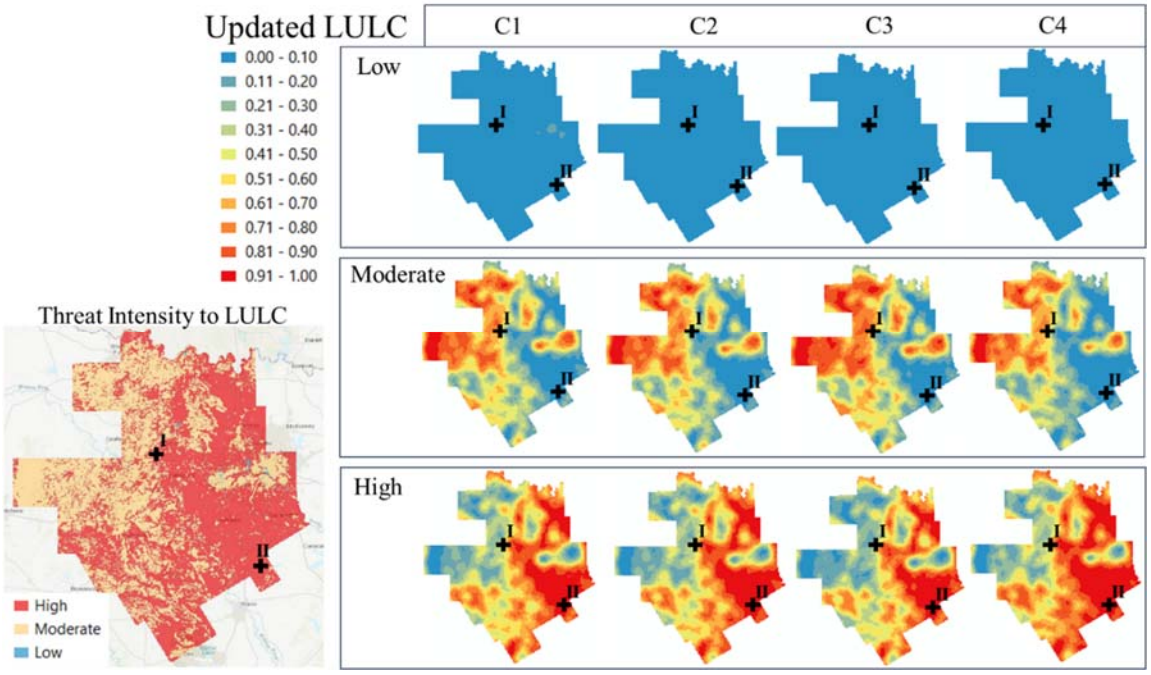

Fig 3.12 Updated hazard to *L* using fixed diagnostic messages C1, C2, C3 and C4.

The points designated as "I" and "II" in figures 3.9 to 3.12 have been individually examined to illustrate the model's response in diagnosis. These points were arbitrarily selected to analyze the influence of the skewness of the marginal probability distributions for different threat intensity levels. Explicitly, the *A*, *W*, *E* and *L* marginal probability distributions in point I are less skewed than the distributions observed in Point II, as seen in table 3.2.

Table 3.2 Marginal probability distributions of points I and II.

Point I	Point II
$P(A_I) = \begin{Bmatrix} Low: 80.83\%, \\ Moderate: 19.07\%, \\ High: 0.10\% \end{Bmatrix}$	$P(A_{II}) = \begin{Bmatrix} Low: 0.00\%, \\ Moderate: 0.00\%, \\ High: 100.00\% \end{Bmatrix}$
$P(W_{II}) = \begin{Bmatrix} Low: 76.86\%, \\ Moderate: 18.46\%, \\ High: 4.68\% \end{Bmatrix}$	$P(W_I) = \begin{Bmatrix} Low: 89.75\%, \\ Moderate: 8.47\%, \\ High: 1.78\% \end{Bmatrix}$
$P(E_I) = \begin{Bmatrix} Low: 20.51\%, \\ Moderate: 79.49\%, \\ High: 0\% \end{Bmatrix}$	$P(E_{II}) = \begin{Bmatrix} Low: 0.00\%, \\ Moderate: 0.00\%, \\ High: 100.00\% \end{Bmatrix}$
$P(L_I) = \begin{Bmatrix} Low: 0.03\%, \\ Moderate: 81.51\%, \\ High: 18.46\% \end{Bmatrix}$	$P(L_{II}) = \begin{Bmatrix} Low: 0.00\%, \\ Moderate: 0.08\%, \\ High: 99.92\% \end{Bmatrix}$

The updated probabilistic values of *A*, *W*, *E* and *L* are listed in table 3. It is observed that the selection of a fixed P(*ES*) responds differently to contrasting skewness of the marginal probability distributions. At point I, a fixed condition favoring low states of *ES* (C1) returns updated probabilities of low hazard higher than the fixed condition favoring high states of *ES* (C4) for all four variables. For this point, the influence of a predominant mode on the fixed distribution C3 produced changes on the updated probabilities of low hazard up to 9% lower than the results obtained for low updated hazard using C2, even though both distributions return the same *RI* = 0.5. However, it is observed that the updated probability distributions of *A*, *E*, and *L* show no-changes with respect to its marginal probabilities in point II for all diagnostic messages, suggesting that higher skewness of marginal probabilities decreases the sensitivity of the BN to diagnostic analysis.

Table 3.3 Updated Probabilities of A, W, E and L given a set of diagnostic messages C1, C2, C3 and C4 for points I and II.

Point I						
Condition	**State**	**P(*ES*)**	**Updated P(*A*)**	**Updated P(*W*)**	**Updated P(*E*)**	**Updated P(*L*)**
C1	Low	0.70	0.72	0.73	0.39	0.00
	Moderate	0.20	0.27	0.24	0.61	0.35
	High	0.10	0.01	0.04	0.00	0.64
C2	Low	0.33	0.63	0.67	0.30	0.00
	Moderate	0.34	0.35	0.29	0.70	0.37
	High	0.33	0.01	0.04	0.00	0.63
C3	Low	0.15	0.55	0.69	0.23	0.00
	Moderate	0.70	0.44	0.26	0.77	0.43
	High	0.15	0.01	0.05	0.00	0.56
C4	Low	0.10	0.61	0.68	0.27	0.00
	Moderate	0.30	0.37	0.26	0.73	0.31
	High	0.70	0.02	0.06	0.00	0.68
Point II						
C1	Low	0.70	0.00	0.63	0.00	0.00
	Moderate	0.20	0.00	0.33	0.00	0.01
	High	0.10	1.00	0.04	1.00	0.99
C2	Low	0.33	0.00	0.53	0.00	0.00
	Moderate	0.34	0.00	0.42	0.00	0.01
	High	0.33	1.00	0.05	1.00	0.99
C3	Low	0.15	0.00	0.44	0.00	0.00
	Moderate	0.70	0.00	0.51	0.00	0.01
	High	0.15	1.00	0.05	1.00	0.99
C4	Low	0.10	0.00	0.49	0.00	0.00
	Moderate	0.30	0.00	0.43	0.00	0.00
	High	0.70	1.00	0.08	1.00	1.00

However, the influence of the diagnostic tool have a wide variety of responses when it is tested on random spatial variables. For instance, the updated maps of *A* and *E* show imperceptible sensibility to any of the four back propagated probabilities in diagnosis, while more significant changes can be appreciated on the updated maps of *W* and *L*. Considering that the four input variables have the same weighted influence on the results, as designated in the conditional probability table, this observation allows to deduce that the diagnostic type of reasoning is more significant for maps with higher levels of dispersion, and less with clustered spatial features. However, the updated *L* map is observed to have a minor sensibility to the diagnostic message propagated from the *ES* node. This effect can be interpreted as the result of having small features of low threat intensity to *L*, resulting in updated maps predicting the behavior of only moderate and high hazard conditions. Given that the results show most significant sensitivity to the diagnostic spatial analysis of *W*, further description of the experimental outputs is based on the behavior of the updated maps of this variable.

It is observed that the fixed condition favoring ES_{Low} (C1) produces updated maps with larger areas depicting higher likelihoods of *W* classified as a low hazard, as compared to the maps with a diagnostic message favoring ES_{High} (C4). Explicitly, it is predicted that to achieve the fixed condition C1, a 25.14% of the study area should be categorized as low hazard to *W*; while only 4.12% would require to have higher likelihoods of low hazard levels to *W* using the distribution C3. It is observed that using a distribution close to uniform such as C2 produces larger areas with probabilities of updated low and high hazards than the maps derived from the presence of a prominent mode, as depicted by C3.

Comparing the updated hazard maps using C2 and C3 it is deduced that the results are sensitive to the shape of a fixed distribution propagated in diagnosis as long as the variable is not clustered and presents more than two representative threat intensity levels.

Analysis

The relative frequency analysis provided insight to the behavior of the *BN+GIS* tool under varying spatial conditions, as defined during the experimental design. The results showed that the number of categories used to discretize the input variables A, W, E, and L has an important influence on the RI, regardless of the spatial sample parameters selected. This influence is evidenced by the three predominant modes observed in all 36 tested combinations of b and g. It was also revealed that the range of values obtained from the RI maps does not reach either of the extremes of the domain [0,1], which could be interpreted as either (1) no extreme values are found in the study area, or (2) the model requires further calibration. In both cases, given that the predicted values are not a measurable physical or parametrical value, further calibration of this model is not viable. Regardless, the significance of these results rely on the quantification of a symbolic value (RI) that shows relative changes in the spatial domain, and that can aid decision makers in the allocation of resources in areas that show higher sensitivity to the proposed model.

It was observed that these relative changes of the outputs across the spatial domain can differ according to the selected parameters b and g. The maps of standard deviation highlight the location of the most sensitive areas to changes on the spatial sampling

parameters. These higher levels of uncertainty are closely related to the location of the zones of contrasting threat intensity levels defined for the variables *A*, *W*, *E*, and *L*.

The differential analysis implemented by computing a sensitivity coefficient and a sensitivity index helped to exhibit how the spatial sampling parameters can affect the results. In this study case, higher levels of model sensitivity to *b* and *g* are considered to be a desirable condition given that the process is capturing a wider response from the model. The ∅ and SI evidence obtained during the experimental design was used to infer that the sensitivity of the model decreases as *b* and *g* increases. However, figures 3.5 and 3.7 suggest that larger *b* and *g* reduces uncertainty of the RI maps, and that the standard deviation is more sensitive to *b* than to *g*. Based on these observations, it is presumed that small grid sizes are most appropriate to maximize the sensitivity of the results without engaging to significantly higher levels of uncertainty.

Yet, the selection of the most suitable and significant buffer size was not answered by the examination of sensitivity measurements and standard deviations. Identifying the optimal distance to sample a geographical population required the quantification of the spatial correlation structure of the results. The autocorrelation analysis using Pearson's coefficient provided a criteria to select a lag distance that can be used as a proxy to buffer sizes. It is observed that the combined spatial influence of the input variables *A*, *W*, *E* and *L* returns *RI* maps with a stronger autocorrelation in the NS direction than on the WE direction for lag distances shorter than 60 km. These analysis can be used to select the level of relevance of the spatial sample with respect to each discrete element.

The diagnostic tool proved to be sensitive to the skewness of the marginal probability distributions of the network. This is interpreted as marginal probabilities depicting 100% certainty of a particular state showed to return full certainty of the updated variable to be the same. The uncertainty level reached with less skewed marginal probability distributions allow the diagnostic tool to return different updated probabilities. This observation is consistent with the response of the *BN+GIS* model given different levels of spatial clustering. Highly clustered variables such as *A* and *E* present large areas with marginal probability distributions depicting 100% certainty that a sample is located within a single threat intensity level, showing the least visible sensitivity to any of the fixed diagnostic messages. In contrast, the updated hazard states of surface water, a less clustered variable, showed to be the most sensitive to the prescribed diagnostic distributions. The updated *W* maps exhibited higher sensitivity in the proximity of the major water bodies located in the study area. The variability observed on the updated diagnostic maps show the areas where the implementation of policies towards the improvement of the vulnerability of the input variables are located. It is observed that higher sensitivity levels are located in zones with contrasting states of threat intensity, such as point I.

Conclusions

The sensitivity analysis implemented in the *BN+GIS* tool provided information about the assumptions made by modelers in the search of an improved decision making tool. The spatial sampling methodology showed that the use of higher resolution (small grid size)

provided results with less uncertainty and higher levels of sensitivity. Lower uncertainty levels are also achieved with larger buffer distances, however, the authors conclude that to select the most appropriate plot size, it should be taken under consideration the spatial autocorrelation of the results. Examining the Pearson's correlation coefficient in NS and WE directions showed to be a useful mechanism to quantify and select a desired level of spatial relationship during the sampling process. Following the methodology suggested in this work, the *BN+GIS* modeler is capable of having an informed criteria to select the desired level of uncertainty and spatial autocorrelation of the results.

The diagnostic reasoning performed by this tool was designed to guide policy makers in their task of selecting the areas that require further investment of resources to reach a desired condition. In the case illustrated in this study, the results could represent the protection of the endangered elements in zones of high probability of updated high threat intensity. The sensitivity analysis performed in this study was used to examine the benefits and limitations of using the *BN+GIS* methodology in diagnosis. It was learned that the diagnostic tool is limited to interpretations on spatially disperse variables with maximized perimetral contact between three or more discrete states, such as surface water bodies. This variable is observed to be less clustered than other variables and presented the highest sensitivity to the selection of different diagnostic messages. Under these type of variables, the tested examples provided insights about the influence of the policy-making criteria on the results. Policies requiring low impacts (C1) provided maps highlighting large areas where resources for active counteractions need to be allocated. Likewise, if policy-makers are willing to assume higher levels of risk (C4), the *BN+GIS* diagnostic tool returns

smaller areas of updated threat intensities that would require less intervention. Testing constant values of *RI* with contrasting shapes of the *ES* message resulted in maps that show visible differences favoring larger areas of updated low hazard states for a uniform distribution.

BN+GIS users can maximize the significance of their results to optimize the allocation of resources for future development projects, as well as making informed decisions of maintenance and monitoring campaigns in existent infrastructures by replicating the methods used in this work.

CHAPTER IV

RISK ASSESSMENT FOR LANDSLIDES USING BAYESIAN NETWORKS AND REMOTE SENSING DATA*

Introduction

Landslides are considered to be among the most damaging natural disasters in the US, with the Pacific Mountain System and the Appalachian Mountain region being among the most susceptible areas within the contiguous United States (Smith et al. 2014). Multiple methods have been implemented for landslide hazard assessment and management. The rise of publicly available remote sensing datasets such as spectral imagery and LiDAR point clouds, along with the increment of software with computational capabilities to manipulate them, have helped researchers to develop new techniques applicable to a wide spectrum of spatial disciplines (Jaboyedoff et al. 2010). As a result of the manipulation of LiDAR point clouds it is possible to obtain a series of surfaces such as Digital Elevation Models (DEM), Digital Terrain Models (DTM) and Canopy Height Models (CHM). Although this evidence does not substitute a detailed field survey, it can provide significant information for large areas with difficult or minimum accessibility, and has

*This chapter is reprinted with permission from ASCE. Modified from "Risk Assessment for Landslides Using Bayesian Networks and Remote Sensing Data" by Patricia Varela Gonzalez and Zenon Medina-Cetina, 2017. Geo-Risk 2017 Conference, GSP 285, 113-123, Copyright 2017 by ASCE. This material may be downloaded for personal use only. Any other use requires prior permission of the American Society of Civil Engineers.

consistently proven to be a successful baseline for landslide applications (Jaboyedoff et al. 2010).

The use of LiDAR for landslide investigations was broadly divided in four main applications by Jaboyedoff et al. (2010) as: landslide detection-characterization, hazard and susceptibility mapping, modelling and monitoring. Mapping landslide susceptibility using remote sensing techniques is a practice that has been implemented using qualitative and quantitative methods that range from visual interpretation of landslide features to statistical and probabilistic techniques. For instance, the Oregon Department of Geology and Mineral Industries (DOGAMI) has developed a protocol for the mapping of landslides using LiDAR derived models, aerial photography, landslide inventories and geologic maps (Burns and Madin 2009). This protocol serves as a detailed description of the methodology to be followed for the visual cataloging process of landslide features such as sediment deposits, scarps, delineation of flanks, adjacent slope angle, type of movements and the level of confidence the interpreter has with the potential identification of a landslide. Other approaches rely on mathematical or probabilistic methods such as Logistic Regressions, Weights of Evidence, Frequency Ratio, Receiver Operating Characteristics, Hierarchy Processes, among others (Lee and Min 2001; Cepeda 2010; Prahdan 2010a; Pourghasemi et al. 2013; Cerovski-Darriau 2016; Gorsevski et al 2016; Mahalingam et al. 2016). This remote sensing information has also been used on more elaborated modeling methods such as Artificial Neural Networks (Biswajeet and Saro 2007; Lee 2007; Brown 2012; Bui et al. 2012; Mahalingam et al. 2016), Bayesian Networks (Song et al. 2012) and Fuzzy Logic (Pistocchi and Napolitano 2002; Prahdan

2010b; Ercanoglu and Gokceoglu 2012) for landslide susceptibility mapping. All these methods rely on the mathematical relationship between existent landslide inventories (used as samples for training and validation) and physiographical characteristics such as slope angle, aspect, relief amplitude, curvature, roughness, among others. At the same time, researchers have used spectral imagery that results in the identification of land cover features such as vegetation, rivers and roads.

Nevertheless, little progress is observed on combining independent maps and methods to create a robust assessment of the landslide susceptibility that can be replicated not only locally, but on a regional or national scale. The objective of this work is to integrate different sources of landslide threats through the representation of causal relationships on a Bayesian Network (BN) to map the state of risk in prognostic analysis, and to assess the original conditions required to achieve a prescribed risk value in diagnostic analysis. The methodology of integrating spatial variables of a BN in a Geographical Information System's (GIS) platform is described by Varela (2013) and it is referred as *BN+GIS*. One of the most significant benefits of using *BN+GIS* is its capability to be updated with new evidence to account for land cover changes and for the increment of publicly available remote sensing datasets. This method is intended to be used by researchers, land managers and decision makers to quantify the state of risk of landslide occurrence by having a systematic methodology as opposed to subjective visually-based analyses of individual landslide susceptibility maps, if available.

BN and Risk

BNs are defined as non-cyclic graphical models that represent the probabilistic cause and effect relationship (arcs) between variables (nodes) while reasoning under uncertainty (Korb and Nicholson 2010). Each variable is represented by a probability density function, while the arcs or connections are depicted as conditional probability tables. The hazard variables are discretized in classes that in this study are defined using three levels of intensity of the threats: low, moderate and high. Bayes theorem represents a probabilistic inference between a hypothesis (H) and the evidence (E) to assess the posterior conditional probability $P(H|E)$. This relationship is interpreted as a causal dependency between 'parent' and 'child' nodes, through a conditional probability table that allows for transmitting the message through the graphic's arcs. When the message is propagated from parents to child (cause to effect), a prognostic reasoning is in place, and when the message propagates from child to parents (effect to cause), we are reasoning in a diagnostic manner. Fig. 4.1 shows an example of a BN with three independent parent variables (V_1, V_2 and V_3) and one child node illustrating a four variables network (n=4), where each variable is discretized in three classes (m=3). The prognosis message ($\pi(Z)$) is described by equation 4.1, which produces a list of 81 values (m^n) with all the possible combinations of the three discrete states of the four variables. When inverse reasoning is performed, a diagnosis message ($\lambda(Z)$) is propagated from the child node to the parent nodes, which is computed using equation 4.2. The diagnosis message consists of a fixed probability distribution of the child node defined by the user, so the BN can compute the potential scenarios that can cause a specific prescribed outcome.

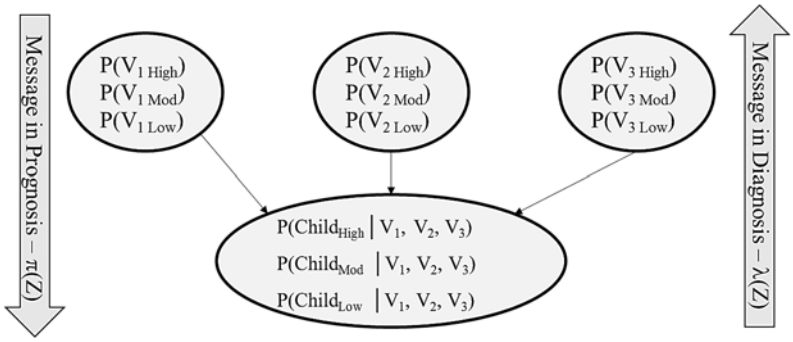

Fig. 4.1 Example of BN showing parent's marginal probabilities and their effect on the child node as a conditional probability.

$$P(Child_i) = \sum_{j=1}^{27} \pi(Z_i) = \sum_{j=1}^{27} P(V_{1i}) * P(V_{2i}) * P(V_{3i}) * P(Child_i|V_{1i}, V_{2i}, V_{3i}) \quad (4.1)$$

$$P(Parent_k) = \sum_{j=1}^{27} \frac{\pi(Z) * \lambda(Z)}{\sum_{l=1}^{81} [\pi(Z) * \lambda(Z)]} \quad (4.2)$$

V: $Parent\ Node$
i: $\{low, moderate, high\}$
j: $\{1,2,\dots,27\}$ $list\ of\ combinations\ where\ the\ Child\ node\ is\ low, moderate\ or\ high$
k: $\{1,2,3\}$ $parent\ node\ index$
l: $\{1,2,\dots,81\}$ $list\ of\ combinations\ for\ three\ classes\ of\ four\ nodes.$

The risk definition used in this study considers the parent nodes as 'Hazard' variables that are combined using equal weights to assess the child node as a measure of the 'Vulnerability', resulting in a probabilistic distribution of the Landslide Sensibility. When the results of the probabilistic distribution of the Vulnerability node are included in the Utility Function ($U(C)$) shown in equation 4.3 a Risk Index that represents a non-probabilistic value that can be used for engineering decision making is obtained. The process as described in equations 4.1 and 4.3 returns the UNDRO (1979) definition of

Risk (equation 4), which has been successfully implemented by Medina-Cetina and Nadim (2006) and by Gardoni, P., and LaFave. (2016).

$$U(C) = 1 * P(Child_{High}) + 0.5 * P(Child_{Mod}) + 0 * P(Child_{Low}) \quad (4.3)$$

$$Risk = [Hazard] * [Vulnerability] * [Consequences]$$
$$= [P(V_{1i}) * P(V_{2i}) * P(V_{3i})] * [P(Child_i|V_{1i}, V_{2i}, V_{3i})] \quad (4.4)$$
$$* [U(C)]$$

Case Study

To achieve this goal a case study was analyzed in a 19.5 km^2 area located in the Oregon Coastal Range, within the Elliott State Forest in Coos County se Fig. 4.2). The area was selected due to the presence of a geomorphology dominated by hillslopes, with the availability of point cloud data and the presence of a database with historical landslides that can be used for the validation and calibration of the proposed risk analysis. The geologic unit that outcrops in the area is the Tyee Formation formed by marine sedimentary rocks (Smith et al. 2014) that have been weathered degrading into a clayey and silty residual soil of variable thickness (USDA 2013).

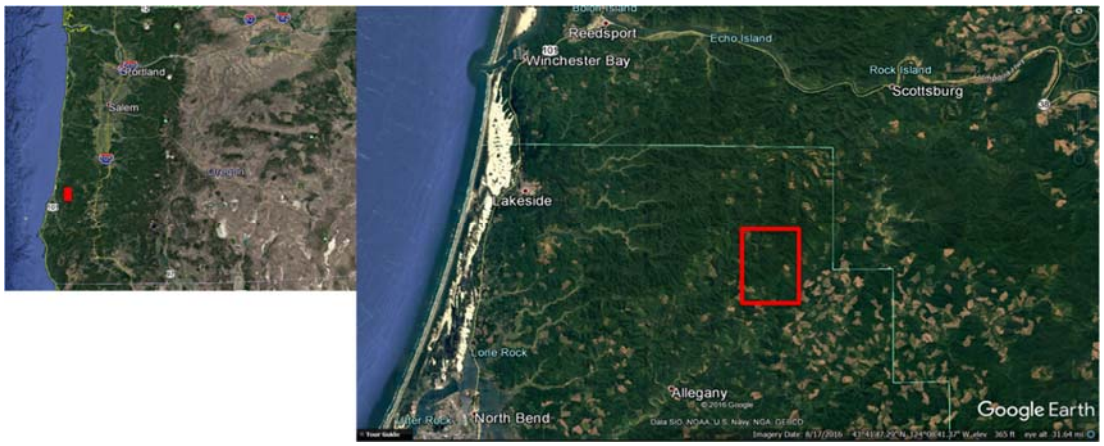

Fig. 4.2 Study area. Modified from Google Earth.

In order to assess the hazard of the study area, a set of four input variables (maps) that represent different criteria for measuring the landslide sensibility of a specific site was defined. All the hazard variables have been developed using remote sensing LiDAR data. The variables are: SLIDO Landslide Susceptibility (SLIDO), a Safety Factor obtained from a physical infinite slope model (Physical Model), Density of Trees (Vegetation Density), and a Compound Topographic Index (Wetness Index). The prototype BN defined for this study can be seen in Fig. 4.3.

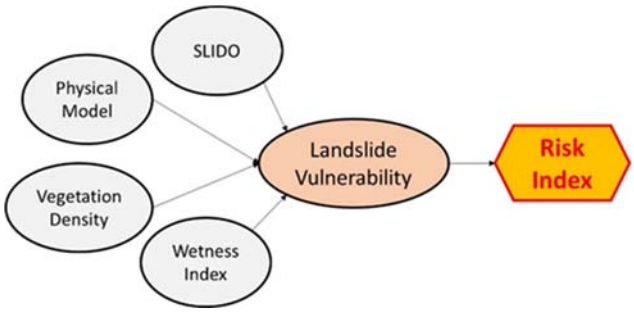

Fig. 4.3 BN model proposed for integrated landslide risk mapping.

The datasets used in this study are observed in table 4.1. All the data was projected to NAD 1983 Oregon Statewide Lambert. A 10 m DEM was obtained from the point cloud using Quick Terrain Modeler software, which represented the best estimate of the terrain without sharp spikes due to the influence of the vegetation. A 1 m resolution CHM was also obtained using this software. The DEM was processed with a "fill" tool in ArcGIS to eliminate potential local peaks or sinks.

Table 4.1 Data sources for the definition of hazard variables.

Dataset	Source	Author	Data Type	Other Information
Airborne LiDAR Point Cloud	OpenTopography – Public Domain	DOGAMI	Point Cloud (.las)	Survey Date: 03/15/2007 - 09/03/2010 Point Density: 8,34 points per m^2
SLIDO Susceptibility Map 3.0 and Historic Landslides	DOGAMI – Public Domain	DOGAMI	Raster (.tiff) Vector, point (.shp)	Update Date: February 2016 Resolution: 10 m
Soil Types of Coos County, OR	Web Soil Survey SSURGO (Soil Survey Geographic Database) – Public Domain	USDA, Natural Resources Conservation Services	Vector, polygon (.shp)	Publication Date: Sept, 2015

State of parent nodes

SLIDO

SLIDO is a susceptibility map developed by the Oregon Department of Geology and Mining Industries that discretizes the Oregon State in four main classes: low, moderate, high and very high. These maps were generated using a geologic map, historic landslide

inventories, and a slope map (Burns et al. 2016). Based on this information, they developed a 'Landslide Density' layer that was generated by computing the mean (μ_{dens}) and standard deviation (σ_{dens}) of the percentage of the landslide coverage area for each generalized geologic unit. They discretized the Landslide Density maps in three states according to the following statistical criteria: Low Density ($< \mu_{dens} = 7\%$), Moderate Density ($>7\%$ and $< \mu_{dens} + \sigma_{dens} = 17\%$), and High Density: ($>17\%$). Their method of defining the thresholds for this variable is not only based on statistical markers such as mean and standard deviation of their inventory, but are also consistent with other national thresholds considered in their literature review. Burns et al. (2016) also produced a 'Slopes Prone to Landslides' layer by computing the slope statistics such as mean (μ_{slope}) and standard deviation (σ_{slope}) within the landslide polygons in relation to the geologic units. The discretization of this layer was defined as: Low (slopes $< \mu_{slope} - \sigma_{slope}$ of slopes found within the landslides per geologic unit), Moderate (slopes $> \mu_{slope} - \sigma_{slope}$ and slopes $< \mu_{slope}$), and High (slopes $\geq \mu_{slope}$). 'Landslide Density" and 'Slopes Prone to Landslides' layers were combined (see Fig. 4.4) to define the susceptibility map as follows: Low (Landslide Density and Slopes Prone to Landslides low), Moderate (Landslide Density low or moderate and Slopes Prone to Landslides low or moderate), High (Landslide Density high with Slopes Prone to Landslides moderate or low, or Slopes Prone to Landslides high with Landslide Density moderate or low), and Very High (existing landslides). In the selected study area, it is observed that the SLIDO susceptibility hazard states are Moderate, High and Very High.

Graphic display of how data sets are combined to create the final landslide susceptibility zones.		Landslide Density Combine: ❶ Generalized Geologic Map + ❷ Landslide Inventory			Landslides ❷ Landslide Inventory
	Class	Low (less than 7%)	Moderate (between 7% and 17%)	High (greater than 17%)	Existing Landslides
Slope Prone to Landsliding Combine: ❷ Landslide Inventory + ❸ Slope Map	Low (less than 1 STD)	Low	Moderate	High	Very High
	Moderate (between the mean and 1 STD)	Moderate	Moderate	High	Very High
	High (equal to or greater than mean)	High	High	High	Very High

Fig. 4.4 SLIDO method for susceptibility mapping using "Landslide Density" and "Slope Prone to Landslide" maps.

Physical Model

A simplified infinite slope model was implemented for a prescribed landslide failure depth (H) of 1 m with a constant water depth of 0.5 m below surface. The equilibrium forces considered in this model are Weight (W), Shear Force (T), Normal Force (N), pore water pressure (u), and Seismic Force using a pseudo-static seismic coefficient (K_h*W) as illustrated in Fig. 4.5 (Briaud 2013). The slope angle was obtained from the DEM. Soil parameters such as unit weight and friction angle were estimated based on the soils unit map, and additional information provided by the SSURGO that include Atterberg limits and sieve analysis on representative samples of each soil unit. The analysis was developed considering normally consolidated cohesionless residual soils. A Factor of Safety (FS) was computed for each pixel of the DEM by calculating the ratio between the resistant and sliding shear stress. The threshold defining the 'High' hazard class was selected at the

limit state where FS≤1. The authors defined the inferior limit of the 'Low' hazard state under the assumption that the global stability of the slopes should have at least the same FS as a structure designed to retain it. A Geotechnical Design Manual (Oregon Department of Transportation 2015) developed by the Highway- Geo-Environmental Section of the State of Oregon recommends the use of the AASHTO LRFD Bridge Design Specifications (AASHTO 1998) as a reference, which suggests a minimum FS = 1.5 for the global stability of a critical support structure. Consequently, the physical model hazard was defined as: Low: FS ≥ 1.5, Moderate: 1<FS<1.5, and High: FS≤1.

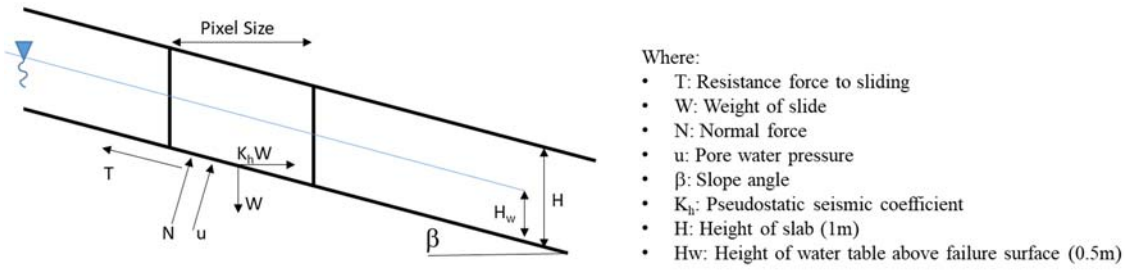

Fig. 4.5 Simplified Infinite Slope Model

Vegetation Density

The influence of the vegetation root system is known to provide additional strength to the soil, and to reduce the probability of failure of landslides (Miles and Swanson 1986, Rickli et al. 2001). This variable was obtained using a CHM derived from the LiDAR point cloud, which provides a surface of the top of the tree canopy without the influence of the terrain's relief. The CHM was manipulated in ArcGIS to obtain an estimate of individual stems per area using local maximum heights that was later used to define the density of the trees. A

cumulative density function of the resulting density was plotted to extract the hazard thresholds for this variable: Low (< 33%), Moderate (>33% and < 67%), and High (>67%).

Wetness Index

This is a secondary terrain attribute that is defined as a steady state value to predict zones of saturation (Gorsevski et al. 2006) that can be interpreted as an index that reflects the likelihood of a pixel of capturing water due to the physiographical configuration of the terrain. Slope angle, flow direction and flow accumulation raster layers were obtained from the DEM. The index is computed using the specific catchment area ($As = [FlowAccumulation_{raster} + 1] * cell\ size$) divided by the tangent of the slope angle (Beven and Kirkby 1979). A cumulative density function of the resulting wetness index was plotted to extract the hazard thresholds for this variable: Low (< 33%), Moderate (>33% and < 67%), and High (>67%). Still, the riverbed pixels were manually modified to a low threat intensity to adjust the significance of this variable and its influence on the occurrence of landslides.

The four spatial hazard variables are illustrated in Fig. 4.4.

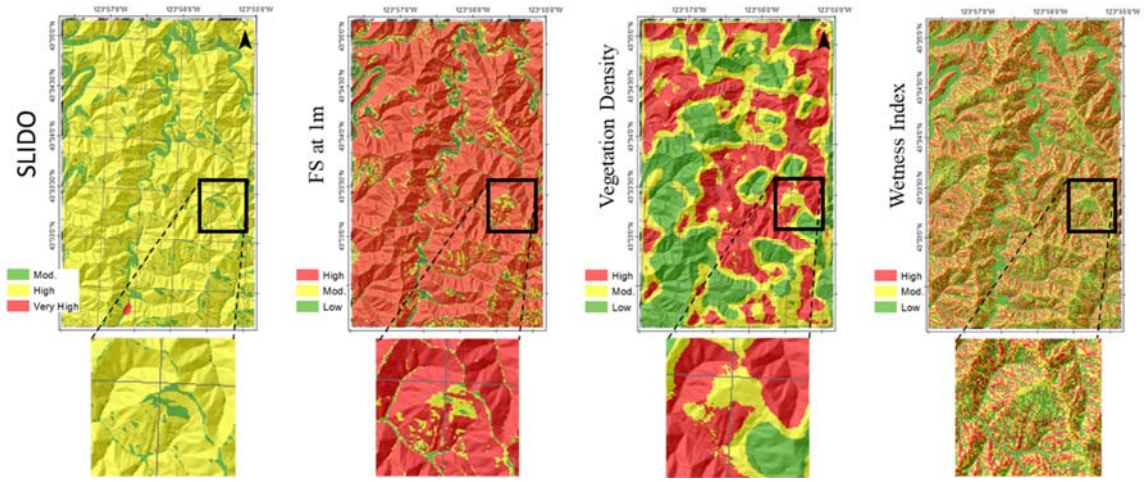

Fig. 4.6 Threat intensity maps over Hillshade.

Results and Analysis

A preliminary set of results using 20 m grid size was used to identify the optimum plot size during the sampling process considering the directional spatial autocorrelation of the results. Fig. 4.7 illustrates the Pearson's correlation coefficient obtained in a WE and NS direction of the preliminary results of risk index values. In this study, a plot radius of 20 m was selected, which embodies a WE autocorrelation value of 0.91 and a NS autocorrelation value of 0.88.

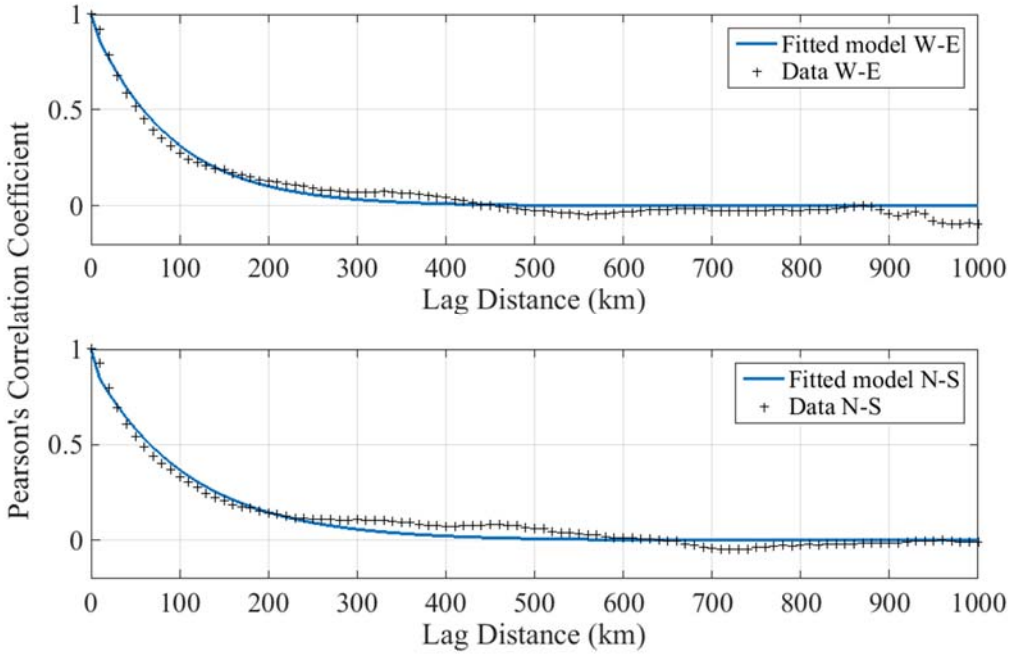

Fig. 4.7 WE and NS spatial autocorrelation curves of preliminary risk index values

The *BN+GIS* system produced a set of four maps that reflects the prognosis analysis (Fig. 4.8) defined by "Probability of High Landslide Vulnerability", "Probability of Moderate Landslide Vulnerability", "Probability of Low Landslide Vulnerability" and by "Risk Index for Landslide", as described in the BN model presented in Fig. 4.3. The vulnerability maps highlight the state of each probability level across the spatial domain, and for each pixel, the sum of each map values is equal to 1. The risk index map shows a strong influence of the vegetation density hazard variable since the zones defined in SLIDO and FS hazard maps are depicting almost a single hazard state, providing little variability to the results. The wetness index provides a set of finer polygon clusters with varying risk

index values within slope faces, accounting for a physiographical response to the capability of the terrain to capture water.

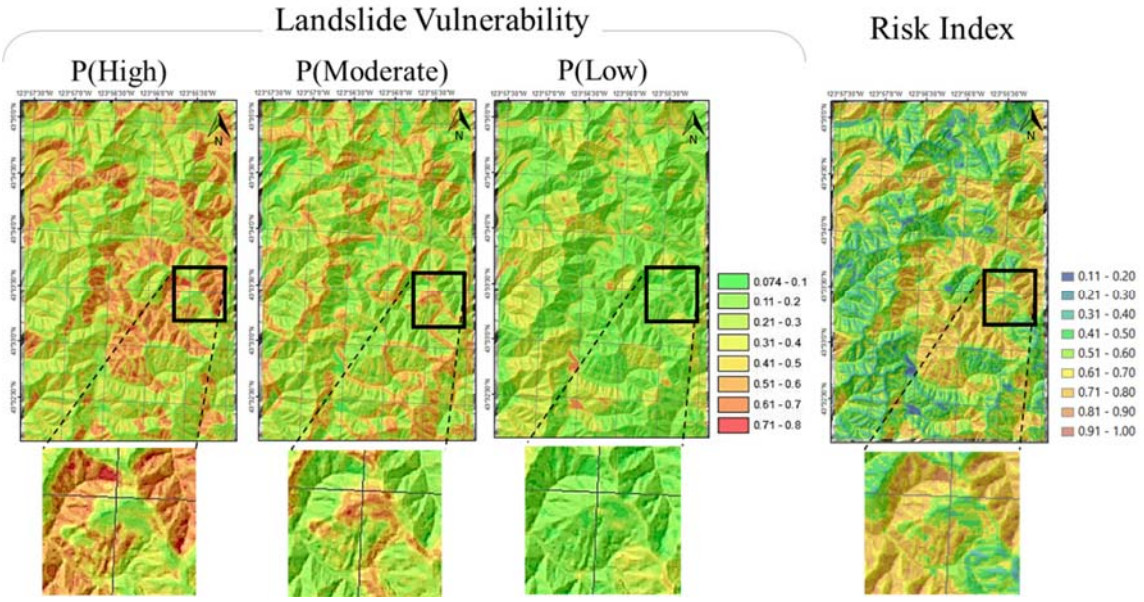

Fig. 4.8 Prognostic maps of probability of landslide vulnerability, and risk index over hillshade.

The infrastructure observed in this study area consists of rural roads that represent potential social, environmental and economic risks in the case of a triggered landslide. The location of 2,341 road points downloaded from the US Census Bureau (2013) were overlaid with the resulting risk index map in order to quantify the potential impact of a landslide on the present infrastructure to aid with a more effective decision making process. Fig. 4.9 (top right) shows the relative frequency plot of the points sampled across the existent roads, along with a fitted normal density function. The mean risk index value for these roads is 0.52 with a standard deviation of 0.13. These results are considerably less conservative than the SLIDO susceptibility and the map depicting the FS of an infinite

slope model used as hazard variables of the BN, due to the influence of the vegetation density and the wetness index effect.

A validation analysis was performed by comparing the 110 historic landslides for depth of 1 m or less reported by DOGAMI's database with the risk index value obtained during this prognosis analysis (see Fig. 4.9, left). The historic landslides present an average risk index of 0.66, a standard deviation of 0.12 and a bimodal frequency (see Fig. 4.9, bottom right). The modes of these samples are located at Risk Index = 0.53 and Risk Index = 0.78. The proportion of the risk index value for these landslides is: 5% between 0.25 and 0.5, 60% between 0.5 and 0.75 and 35% in the 0.75 and 1.0 range. Considering that the historic landslides are inventories of slopes that have already experienced deformation and find themselves in a post-failure equilibrium state, it is reasonable to infer that these show risk index values smaller than 1. Consequently, the *BN+GIS* risk predictions are expected to have values closer to 1.

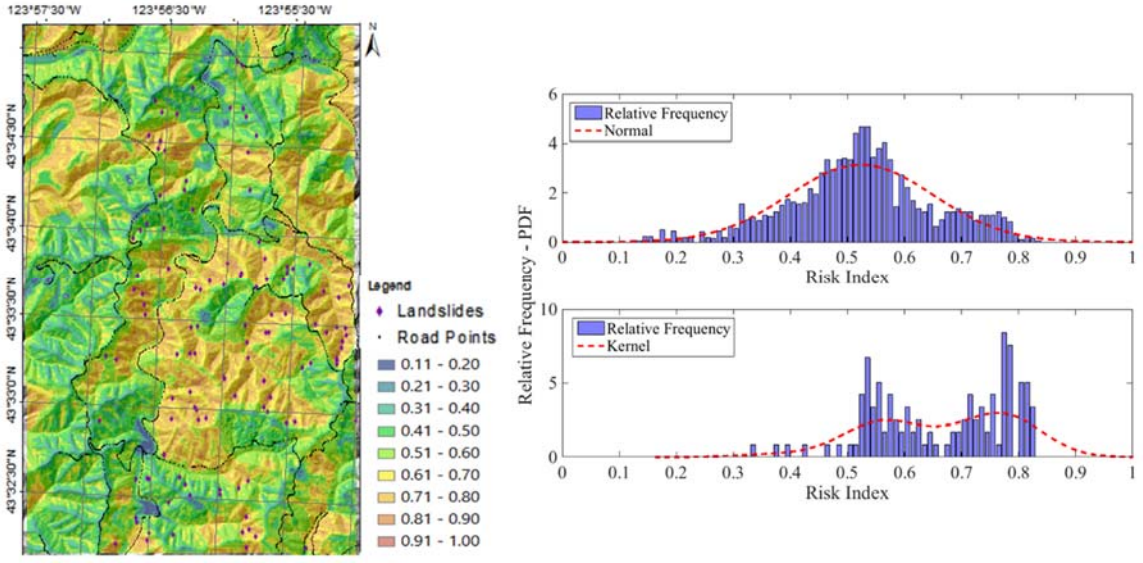

Fig. 4.9 Quantification of risk of landslides on existent roads and historic landslides.

The *BN+GIS* produced as well a set of maps that reflects the diagnostic analysis (Fig. 4.10) where a prescribed condition of the probability of the three states of landslide sensibility was set as: High = 0.3, Moderate = 0.4, and Low = 0.3, which yields a Risk index of 0.5 (equation 4.3). Notice that this probability represents the $\lambda(Z)$ term in equation 4.2. Since all four hazard variables are discretized in three classes, the results of the BN in diagnosis yielded 12 maps. The updated patterns observed on these maps are more sensitive to changes in the transition zones between hazard states such as high next to moderate, moderate next to low, and low next to high. This is due to the fact that a sample polygon with 100% of a specific hazard state will return the same probability on the diagnostic computation. In order to achieve the prescribed risk index of 0.5 across the complete study area it is necessary to implement the correspondent counter-measurements required to achieve the updated hazards state depicted by the diagnosis maps. For instance, the low vegetation density zones representing high updated hazard states can be reforested using species to strengthen the soils on those particular slopes.

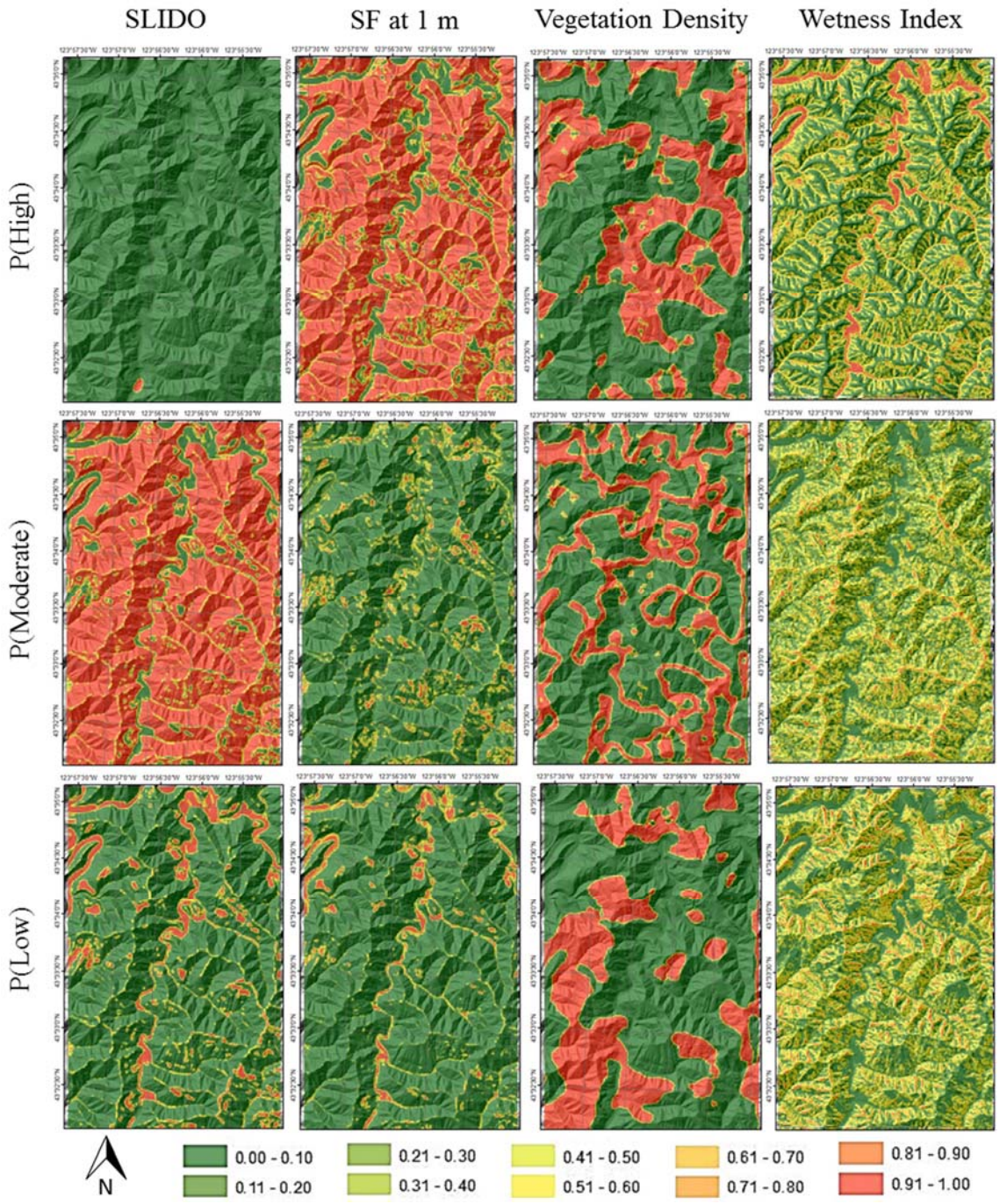

Fig. 4.10 Diagnostic maps of updated probability of hazard levels for 1 m sliding mass.

Conclusions

This study is a preliminary approach to map the hazard, the vulnerability and the risk based on a probabilistic approach capable of integrating different sources of information. This methodology can be updated as more LiDAR datasets are available for public domain, and later compared for analyzing land cover changes. The results of this analysis show that by integrating different approaches for landslide susceptibility, the BN+GIS tool is already capable of predicting the state of hazard, vulnerability and risk without training data. Future work will focus on the integration of historic landslides for training the conditional probability table to have a better estimate of the vulnerability. The validation analysis provided a quantification of the model's accuracy, resulting on 95% of pre-existing landslides having a risk index larger than 0.5 with a mean of 0.66. Comparing the input maps with the risk index map it is observed that the integration of multiple hazard variables derived mostly from LiDAR data, reduces significantly the amount of high risk scenarios, showing a less conservative depiction of the risk. This allows for the narrowing of the spatial domain that needs to be treated, especially when contrasted with the existent infrastructure, which represents a more efficient and improved decision making process. The maps obtained during the diagnostic analysis portray the required initial conditions necessary to achieve the prescribed risk scenario of 0.5 in the whole study area (notice that other risk scenarios can be formulated). Therefore, the updated hazard maps allow for the identification of the changes that can to be made in order to obtain that specific risk index value. It is important to highlight that the decisions based on the diagnosis analysis is applicable for variables that measure a state that can be modified by human intervention.

In this case, the variable that better fits this condition is the vegetation density. In order to take actions to modify the physical initial conditions of the SLIDO susceptibility, the FS map, or the wetness index, is necessary to change the shape of the topography, which, although not realistic in a large scale, it is achievable for specific slopes or small sites.

Disclosure

This chapter is an updated version of a final draft proceedings article published by ASCE at the GeoRisk Conference, Denver, CO. on May 2017. The link to the bibliographic record of the published version in the ASCE Library or Civil Engineering Database is <**https://doi.org/10.1061/9780784480724.011**>.

CHAPTER V

BAYESIAN MODEL CALIBRATION OF SUBMARINE LANDSLIDES

Introduction

Offshore integrated site characterization is conducted to plan and design for the installation of infrastructure such as wind farms, telecommunication cables, hydrocarbon pipelines, and oil and gas production infrastructure. Most of the geotechnical aspects considered for the development of an offshore project are related to the identification of potential hazards and the definition of soil properties to predict their behavior as it interacts with the installed infrastructure. Some of the challenges faced during an integrated site characterization include the understanding of the geological conditions and processes reigning the environment, the spatially variable stratigraphy and the heterogeneous nature of the soil properties in place. However, the financial cost required to complete surveying offshore campaigns force geoscientists and engineers to develop techniques that maximize the amount of inferences derived from the data that can be collected (Young et al. 2011). Masson et al. (2016) describes submarine landslides as part of the sediment transport mechanism of the continental shelf responsible for damages on offshore infrastructure. The occurrence of marine or inland landslides is frequently used to estimate the strength of the soils and to conduct back analysis to assess their physical properties (Gilbert et al. 1998). However, as pointed out by Duncan (1992), the definition of the landslide failure

mechanism can be a challenging task, and relying solely on bathymetric data reduces the reliability on such predictions. The Bayesian inference for model calibration and back analysis of physical parameters is described in the literature as a suitable approach to maximize the inferences obtained from the available datasets by means of uncertainty quantification (Gilbert et al. 1998). Moreover, the Bayesian method allows to combine disparate sources of evidence such as available observations, model predictions and educated expert's beliefs (Robert 2007; Ranalli et al. 2013).

In this work, the Bayesian paradigm was applied to a simple physical model to predict the probability of failure of submarine landslides. Bathymetric data, cone penetration tests (CPT), laboratory soil testing, and expert's prior knowledge of geotechnical parameters were used as sources of evidence. The initial state of the submerged and saturated soil unit weight ($\gamma_{sub}, \gamma_{sat}$), thickness of slice ($H$), pseudo-static seismic coefficient (k) and slope angle (α) served as prior probabilities of an infinite slope model to achieve model predictions of probability of failure and their correspondent uncertainty. Previous research conducted by Das (2016) have used this methodology defining the typical behavior of these prior distributions using expert's beliefs for mean, variance and shape of the prior distributions. Relying solely on bathymetric data and expert's elicitation of information, Das' findings comprise the suitability of the Bayesian framework to reduce the uncertainty of the estimated parameters and consequently, of the probability of failure. As a continuation of Das' contributions, this work used informed priors based on bathymetric data (α), CPT logs ($\gamma_{sub}, \gamma_{sat}$), and modeled values of k and H for the selection of the

prior distributions. Furthermore, values of undrained shear strength (S_u) obtained from the CPT logs were used to calibrate the model.

This work was conducted with the purpose of fulfilling the following objectives: (1) extending the methodology discussed by Das (2016) to estimate the calibrated probability of failure of a submarine slope due to static loading conditions, (2) to study the effect of the sediment thickness on the results, (3) to estimate updated probability distributions of the physical parameters of the slope stability model, and (4) to quantify the uncertainty about prior and posterior estimations.

Submarine landslides have been roughly categorized by Masson et al. (2016) according to four distinctive failure mechanisms: (1) *slide* of a coherent mass of sediment with distinctive boundaries, (2) *debris flow* of a cohesive material transported in a laminar flow, (3) *debris avalanche* of rock conglomerates, and (4) *turbidity currents* of sediment particles suspended in a turbulent flow. Slope failures occur due to an increase of loading forces, for a decrease of the resistance of the soil, or given a combination of those two scenarios (Rahman 1994). In marine environments, events such as seismic activity, sedimentary loading, excess pore water pressure, diapirism, tidal scour, currents, cyclic loading, sea level changes, among others, can trigger the occurrence of landslides (Rahman 1994; Masson et al. 2016). All these considerations must be carefully examined in every step of the design and development of offshore infrastructure, and it starts with an integrated geological, geophysical and geotechnical site characterization. This type of analysis is site-dependent, and it requires the collaboration of experts with multiple areas of expertise to produce a comprehensive geohazard and risk assessment. This work is

designed to contribute with a technique that can help to improve the reliability of the design parameters used for offshore infrastructure, given a limited amount of available information.

Methodology

Infinite Slope Model

Based on Spencer's limit-equilibrium analysis (Spencer 1967), this method constitutes the simplest approach to assess the stability of a slope assuming that the failure surface is parallel to the slope surface, and that the mobilized sediment is orders of magnitude thinner than the length of the slope. In other words, the infinite slope analysis assumes that the slope has a relative infinite length (Briaud 2013). The free body diagram illustrated in Fig. 5.1 shows a schematic example of the load vectors applied to a volume of sediment such as horizontal pseudo-static seismic coefficient (k), weight of the volume of soil (W), and undrained shear strength (Su), along with the thickness of the estimated slip surface H, the slope angle (α), and the length of the sliding surface for the studied element (l) with a top view length b.

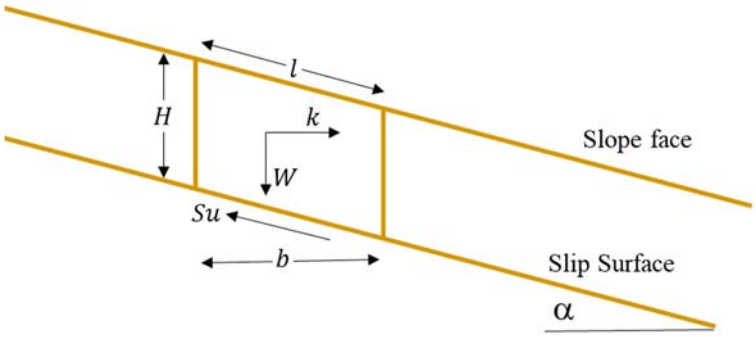

Fig. 5.1 Infinite slope model scheme. Modified from Spencer (1967).

At a limit-equilibrium state the vectors k and W depict loading forces that contribute to the sliding of the sediment wedge, and are equivalent to the resistance provided by the vector Su. This relationship can be expressed as $S_u \cdot l = W' sin\alpha + kWcos\alpha$, where $W = \gamma_{sat} bH$, and $W' = \gamma_{sub} bH$ (modified from Spencer 1967). Substituting l by $b/\cos(\alpha)$ it is possible to estimate that the undrained shear strength required to achieve equilibrium state with the loading forces is $S_u = \gamma_{sub} H \left(\sin\alpha \cos\alpha + k \frac{\gamma_{sat}}{\gamma_{sub}} \cos^2\alpha\right)$ (Haneberg 2012). Hence, the factor of safety (FS) is defined as the ratio between the resisting and the loading forces using equation 5.1 (Bishop 1955).

$$FS = \frac{Resisting\ Forces}{Loading\ Forces} = \frac{S_u}{\gamma_{sub} H (\sin\alpha \cos\alpha + k \frac{\gamma_{sat}}{\gamma_{sub}} \cos^2\alpha)} \qquad (5.1)$$

The Safety Margin ($SM = Resisting\ Forces - Loading\ Forces$) is regarded as the threshold describing the amount of allowed increase of loading forces before failure occurs (Shooman 1968). Assuming that the parameters of this model are regarded as random variables, it is possible to describe the loading and resisting forces as probability density functions. Thus, the probability of failure is expressed as $P(f) = P(SM < 0)$.

Bayesian Probabilistic Calibration

The Bayesian inference is described as an inductive reasoning method based on Bayes' rule ($(P(A|B) = (B|A)P(A)/P(B)$) for updating the probabilistic state of random variables. Consider the parameter space $\Theta = \{\theta_1, \theta_2, \dots, \theta_n\}$ such that is representative of a set of random parameters that allows a function $g(\theta)$ to retrieve the best estimate of a studied phenomenon. The purpose of Bayesian inference consists on learning from Θ and quantifying the reduction of the uncertainty about its statistical properties (Hoff 2009). The probabilities of each element of the sample space $(P(\theta_1), P(\theta_2), \dots, P(\theta_n))$ are considered as *prior distributions* depicting the belief that they are representative of the true population. Let the quantity d_{obs} represent a set of samples derived from experimental observations of Θ, and d_{pred} represent the predictions of the *forward model* g. Using the Bayes' rule, the *posterior probability* $\pi(\theta|d_{obs})$ can be expressed by equation 5.2 assuming that the parameters are collectively exhaustive, where $\pi(\theta)$ is depictive of the priors, and $f(d_{obs}|g(\theta))$ is called the *likelihood function*.

$$\pi(\theta|d_{obs}) = \frac{f(d_{obs}|\theta)\pi(\theta)}{\int_{\Theta} f(d_{obs}|\theta)\pi(\theta)d\theta} = \frac{f(d_{obs}|g(\theta))\pi(\theta)}{\int_{\Theta} f(d_{obs}|g(\theta))\pi(\theta)d\theta} \tag{5.2}$$

The likelihood function is contrasting the model's predictions with the experimental observations. Considering that both sources of evidence (d_{obs}, d_{pred}) are subject to either epistemic and/or aleatoric uncertainties, the Bayesian probabilistic calibration uses a normally distributed likelihood function $N(d_{pred}, \sigma_{d_{obs}-d_{pred}})$ to estimate the probability of the experimental observations to be true given the predictions of the model.

A systematic sampling mechanism such as the Markov Chain Monte Carlo (MCMC) algorithm is used to extract random samples from the probability distribution of the priors and to estimate the posterior distributions. A coefficient of variation (CoV) is used to control the step size of the parameters for each loop. However, to avoid the periodicity of the estimations with every iteration, the proposed methodology includes the use of the Metropolis-Hastings algorithm to test a value that is posing as the current state of evidence with a candidate value. The acceptance or rejection criteria is retrieved from equation 5.3. Let u represent a random sample that ranges between 0 and 1. If $A \geq u$, the posterior of the candidate vector of parameters is accepted and becomes the new current state of evidence, otherwise, the chain does not move and examines a new candidate (adapted from Hoff 2009).

$$A = min\left\{1, \frac{Posterior(candidate)}{Posterior(current)}\right\} \tag{5.3}$$

A vector with the accepted set of parameters is retrieved after the iterative process is finished. Cross plots of the number of iterations vs updated parameters are examined to ensure that the process has captured the best estimates and that the variance remains homogeneous. The iteration number at which the variance curve starts to show a homoscedastic behavior is denoted as the *burn-in point*, and serves to select the set of values of the output vector to discard (before burn-in point), and those used to define the posterior distributions of the analysis. The forward model ($g(\theta)$) is computed using the prior and the posterior state of evidence for comparison, and to determine the reduction of

uncertainty achieved after the model is calibrated. A flowchart illustrating this process is observed in Fig. 5.2.

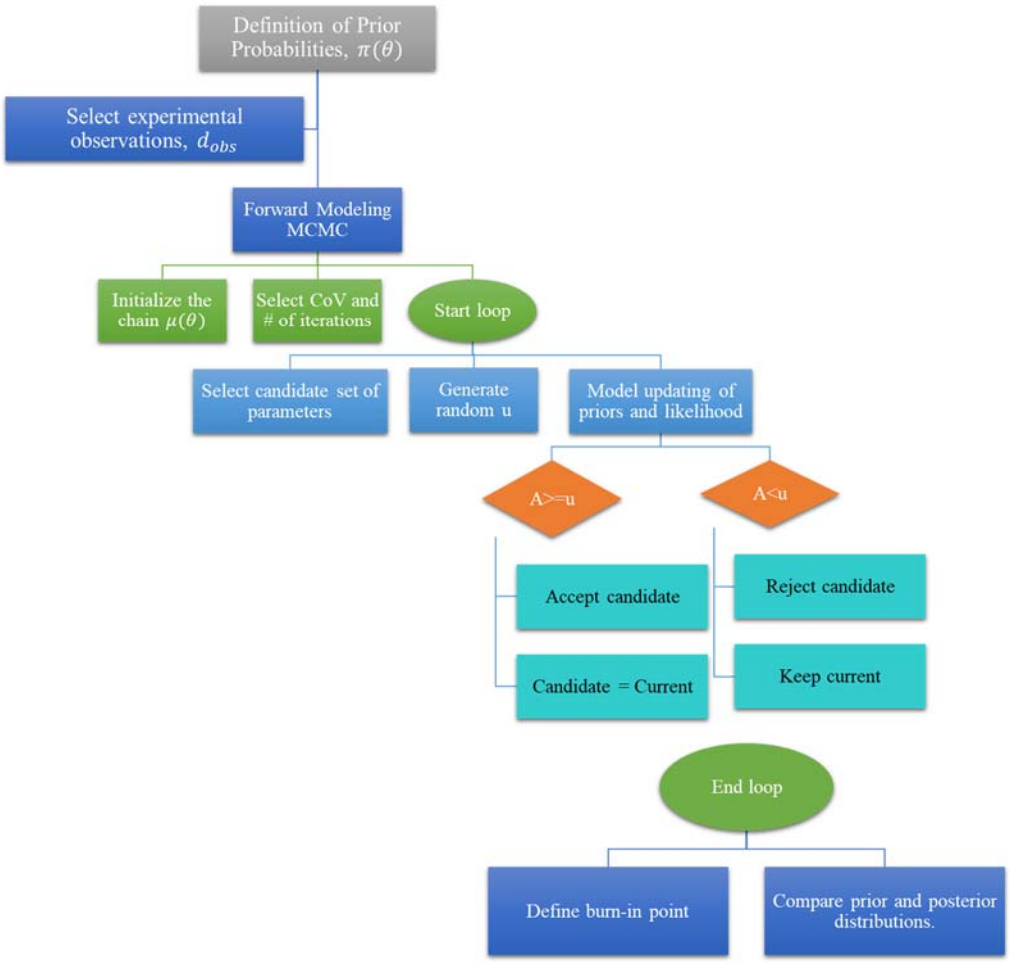

Fig. 5.2 Flowchart of Bayesian model calibration using a MCMC process

In this study, the Bayesian probabilistic calibration method is used to obtain a posterior distribution of the parameters used on the infinite slope forward model to estimate the undrained shear strength (Su) of the soil. Hence, $\theta = \{h, \alpha, k, \gamma_{sub}, \gamma_{sat}\}$ is the set of parameters to be estimated, and d_{obs} are the evidence of Su used to calibrate such

predictions. The computational implementation of the process described in Fig. 5.2 was conducted using a Matlab programming language.

The results of the forward model using the prior and posterior state of evidence are considered to be representative of the expected value of the Su population. A set of random samples are extracted from both estimations, which serve as the mean of the modelled prior and posterior populations of the load using the standard deviation of the measured values of Su. In other words, the loading forces are simulated by the forward model of the prior and the posterior state of Su, and the resistant forces are represented by the population of laboratory tested Su values. Thus, these populations are used to compute the SM and the probability of failure of submarine landslides.

Case Study

The evidence used in this project consists on a dataset of high resolution bathymetry (3m) and 8 CPT logs (see Fig. 5.3-A). The study area occupies 784 km^2 and is located in an offshore location under a water column that ranges approximately between 1,500 m and 1,800 m deep. Features such as NS oriented submarine canyons, and ridges with a NW-SE preferential orientation are observed in the area of interest. Other linear features are interpreted as slip faults oriented in a SW-NE direction, and thrust faults proximal to the observed ridges in a NW-SE orientation. Additionally, a total of 152 (Fig. 5.3-B) mobilized and accumulated sediments were interpreted as submarine landslides that have already surpassed the failure state. The observed displaced sediments are mostly of the

slide type (Masson et al. 2006) suggesting that the infinite slope model could be a suitable method for analyzing the failure mechanisms identified in the dataset.

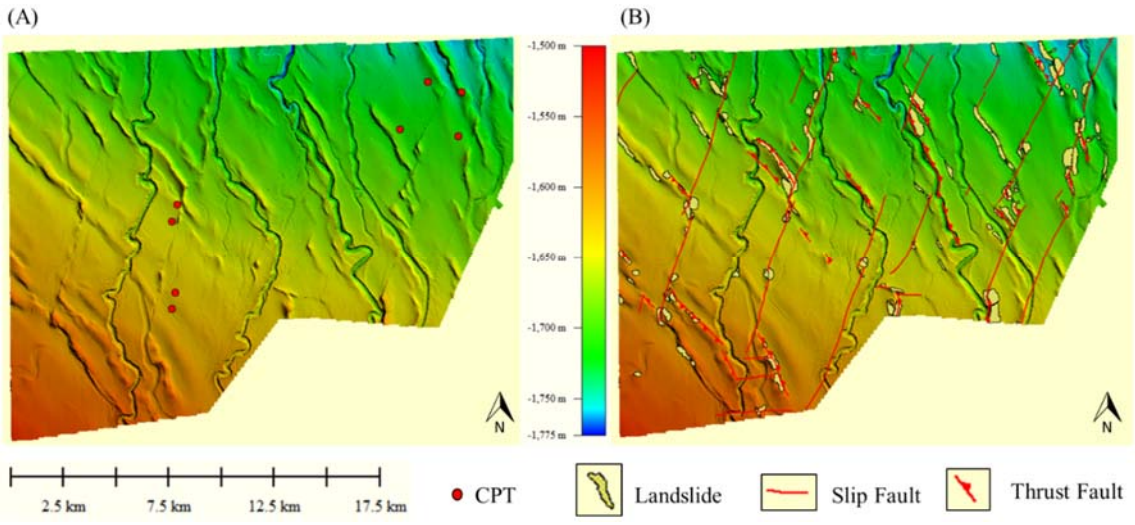

Fig. 5.3 (A) Bathymetry and CPT borehole locations. (B) Bathymetry, interpreted faults and catalogued landslides.

The CPT logs used in this study reach up to 100 m depth that include modeled values of undrained shear strength (Su) obtained from the cone penetration resistance. The models displayed in these logs include the classical approach of empirical cone factor for clays N_{kt} = 15 and N_{kt} = 20 (Rémai 1998), and a method proposed by Quiros et al. (2000) with and without the use of a relationship between undrained shear strength and the pressure water content ratio, labeled as SPW and SP, respectively. The in-situ tests were conducted along with the use of fixed piston samplers equipped with 67 mm inner diameter liner used to obtain soil samples for laboratory testing. Tests to assess values of undrained shear strength (Su) such as torvane, miniature vane (ASTM D4648/D4648M − 16) and

unconsolidated undrained triaxial (ASTM D2850 − 15) are also reported in the CPT logs displayed in Fig. 5.4.

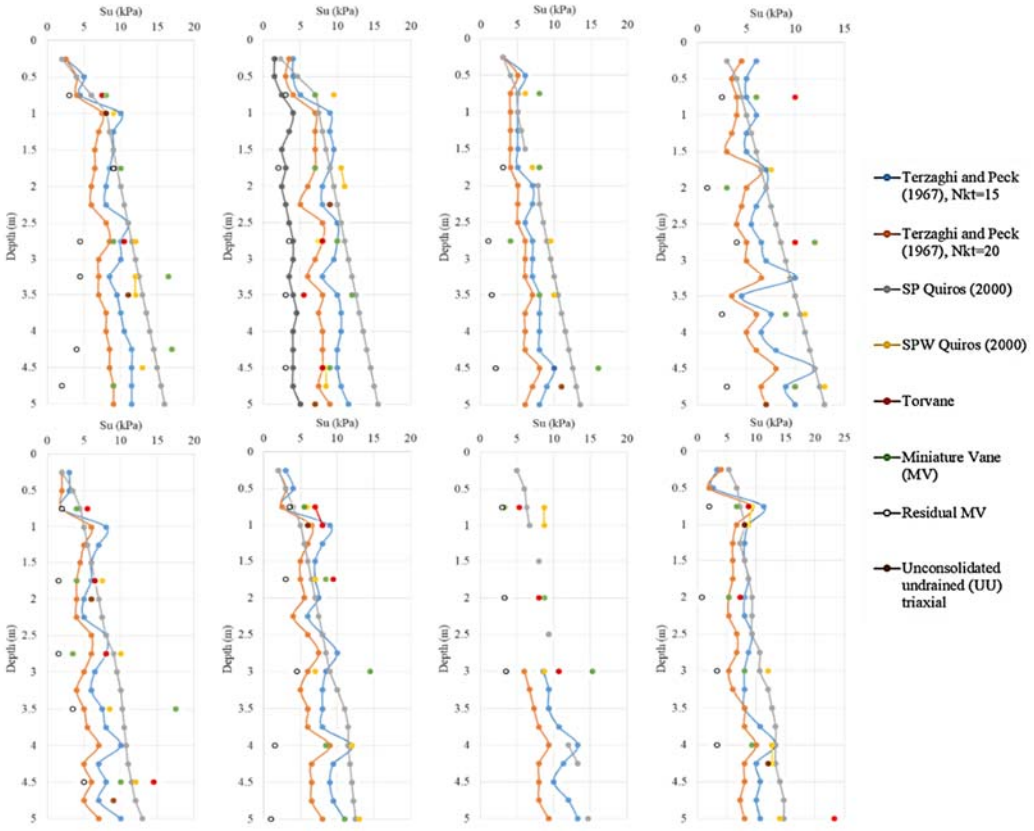

Fig. 5.4 Modeled and measured values of Su (kPa) retrieved from CPT logs.

The soil unit at the top of the surveyed area is consistently described as a very soft olive gray clay, frequently calcareous, with shell fragments, foraminifers, and pockets of organic matter. None of the boreholes reached the base of this unit, suggesting that its thickness is larger than 100m. Yet, the logs indicate that the clay's strength transitions from soft to stiff as the depth increases. Occasional lenses of stratified sand or silt were detected between 9 and 13 m of depth. Classification laboratory tests reported in the CPT

logs include submerged soil unit weight (ASTM D7263 − 09), water content (ASTM D4959 − 16), and Atterberg limits (ASTM D4318 − 17), as seen in table 5.1. All samples present a liquid limit larger than 50% and are positioned above the "A" line of the plasticity chart (see Fig. 5.5), meaning that are classified as high plasticity clays (CH).

Table 5.1 Classification laboratory tests.

Log	Depth (m)	PL (%)	LL (%)	ω (%)	γ_{sub} (kN/m^3)	Log	Depth (m)	PL (%)	LL (%)	ω (%)	γ_{sub} (kN/m^3)
1	1	22	84	75	5	5	0.75	22	60	80	6
	2.75	22	82	70	--		1.75	24	76	80	4.6
	3.25	30	105	98	4		2	--	--	--	5.5
	4.5	25	92	90	4.5		2.75	24	80	80	5.2
2	0.75	20	55	60	5		3.5	34	134	104	3
	1.75	--	--	75	4.25		4.5	29	100	86	3.4
	2	24	75	75	4.5		4.75	--	--	--	4
	2.25	--	--	75	4.75	6	0.75	22	79	79	1.2
	2.75	24	80	75	3.5		1	--	--	73	2.2
	3.5	26	105	90	3.5		1.75	28	84	117	1.7
	4.5	--	--	80	4		3	28	100	112	2.3
	4.75	26	100	95	--		4	22	69	77	3.75
	5	--	--	--	4.5		5	25	92	79	3.8
3	0.75	20	58	58	5	7	0.75	26	77	72	4.6
	1.75	25	76	84	4.5		1	26	72	76	5.2
	2.75	25	80	82	4		2	--	--	--	5
	3.5	27	88	88	4.25		3	28	128	118	3.1
	4.5	--	--	--	3.75	8	0.75	22	64	61	6
	4.75	27	100	95	4.75		1	--	--	--	5.7
4	0.75	20	56	63	5		2	--	--	--	1.8
	2	26	86	80	4.4		3	24	76	76	6
	2.75	23	80	76	4.8		4	--	--	--	7.2
	3.75	23	80	76	4.8		4.25	--	--	--	5
	4.75	--	--	--	5.2		5	24	97	92	4
	5	23	86	76	5.4						

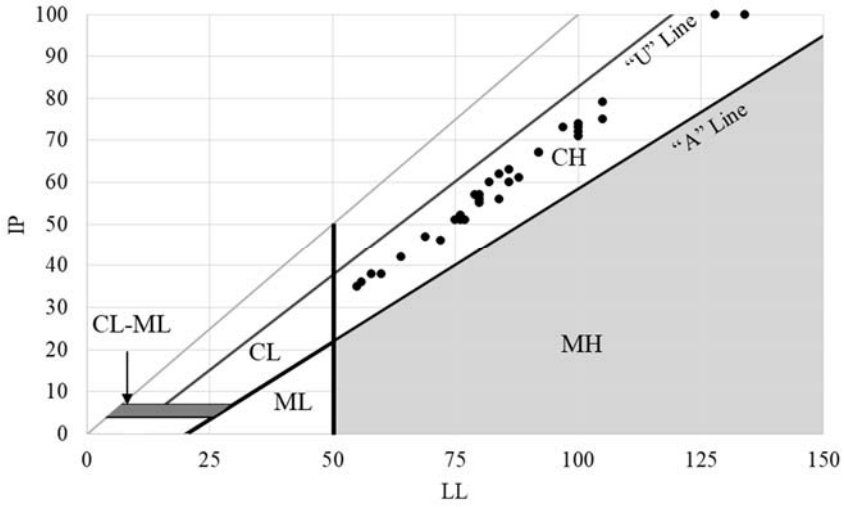

Fig. 5.5 High plasticity clay samples on plasticity chart.

Experimental Design

To estimate the updated geotechnical parameters involved in the infinite slope model and the associated probability of failure through the Bayesian paradigm, the model was tested using two conditions: (1) limit state using a FS = 1, and (2) considering the FS as a random variable ($\mu = 3, \sigma = 1$). With the purpose of quantifying the reduction of the uncertainty on the results given the amount of evidence presented to the model, the quantity of observations (d_{obs}) retrieved from the available Su dataset was also tested using 5 and 20 samples. Ultimately, the dependency of the variables on changes of depth was tested considering the first 5 m of sediment as part of a single population, and other 5 cases with data retrieved from different ranges of depth, as described in Fig. 5.6. A total of 24 experiments were conducted.

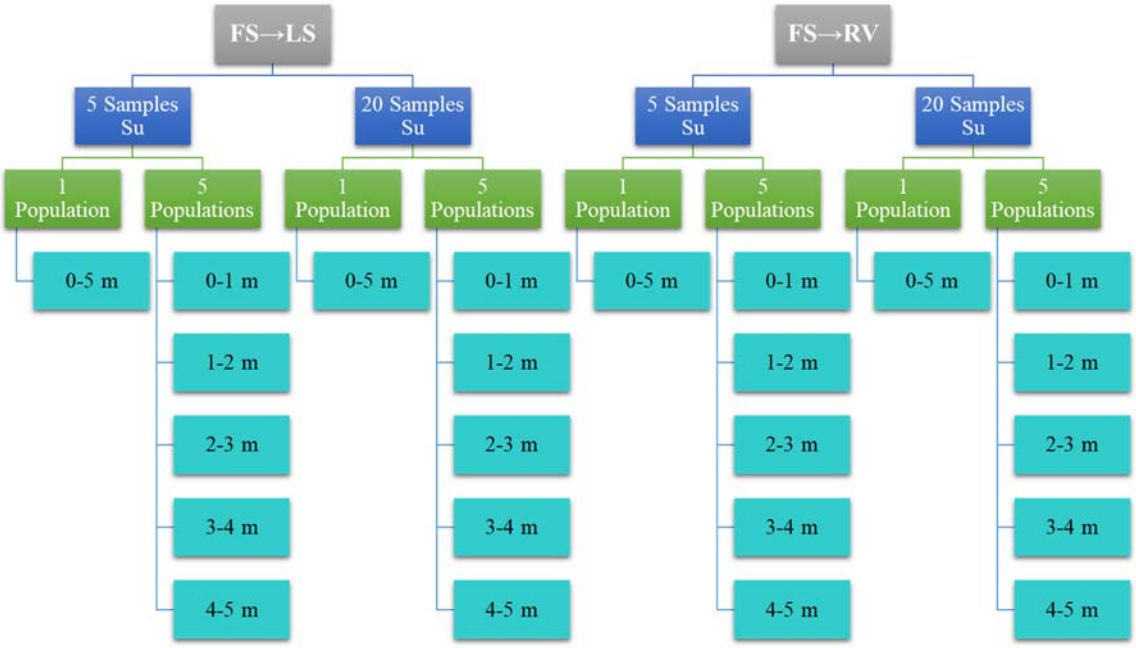

Fig. 5.6 Experimental Design.

Definition of Prior Probability Distributions

Height of Sediment (H)

The occurrence of landslides in the study area offers an important source of information that can be mined for making predictions about future mass movements. It is often necessary to estimate the volume of the displaced material during a landslide, which requires to evaluate the pre and post deformation surfaces of a slope. Völker's (2010) describes a GIS tool that uses the bathymetric information adjacent to observed landslides to model the geometry of the slope prior to failure. The catalogued observed landslides served as a population for the definition of failure mechanisms and geometrical parameters such as height of mobilized sediment (H) and slope angle (α). However, eleven out of the

152 landslides were selected as suitable samples given that they satisfy the following criteria: (1) have a well delimited perimeter boundary that allows for sampling the non-deformed bathymetry around the deformed zone, (2) the type of landslide is representative of the typical failure mechanism in the study area, (3) the landslide is not located in a submarine canyon, and (4) the ridge of the slope has a minimum curvature at least 200 m around the deformation zone. The position of these 11 samples is illustrated in Fig. 5.7. The position of these sampled landslides yielded a spatial distribution that is representative of the area of interest.

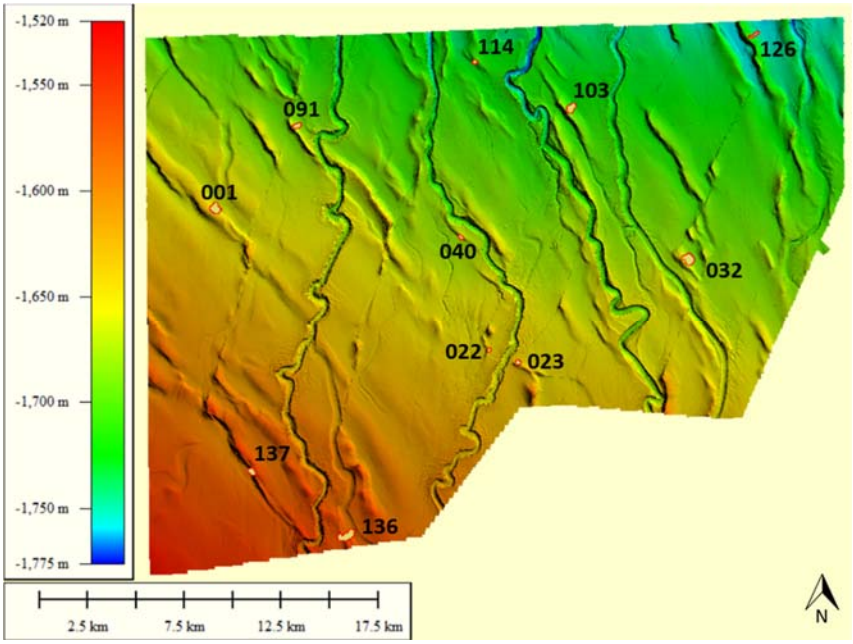

Fig. 5.7 Landslide samples used for geometric analysis of deformation patterns.

The methodology used to define the prior probability distribution of the sediment height consisted on the spatial analysis of the sample landslides and their surroundings, as seen in Fig.5.8. This method consists on the modeling of pre-deformation surfaces that were compared with the current bathymetric configuration to compute mobilized and

accumulated volumes (Völker 2010). Using ArcGIS, buffers of 100 m and 500 m from the polygons that define the boundaries of the sample landslides were used to extract the bathymetric information. These individual areas were posteriorly exported to a point format feature class. The points located outside the perimeter of the displaced sediment mass was used as training samples for a set of interpolated surfaces obtained from the ArcGIS toolbox to model the bathymetric conditions before the failure occurred. The interpolation models used in this stage were:

- Inverse Distance Weighted (IDW): is a deterministic method that produces values according to a weighted average of values proportional to the distance between them (Mitchell 1999).
- Kriging: is a method like IDW where the weights are not only based on the distance between the observations, but also on their overall arrangement using their autocorrelation structure and semivariograms (Mitchell 1999).
- Bayesian Kriging: is a kriging interpolation that considers the semivariogram as a random variable, where the best estimate is determined by the use of a Bayesian paradigm (Mitchell 1999).
- Spline: is a model that fits a mathematical function to a set of nearby samples that passes through the input points while minimizing the total curvature of the surface (Mitchell 1999).
- Nearest Neighbor: is a method that measures the distance between each feature centroid and its nearest neighbor's centroid location. It then averages all these nearest neighbor distances (Mitchell 1999).

- Trend: is an interpolation method that uses a global polynomial interpolation that fits a smooth surface defined by a mathematical function (a polynomial) to the input sample points. A maximum of 12 bends (twelfth order) are allowed in the ArcGIS toolbox (Mitchell 1999).

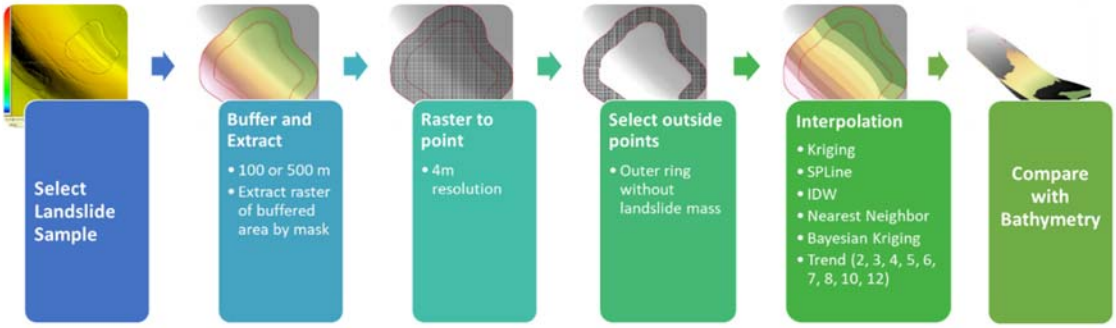

Fig. 5.8 Methodological sequence to obtain sediment height (*H*) at failure.

The six listed interpolation models used, including 9 variants of the "trend" method, yielded a total of 14 models for each of the eleven selected landslide samples. The sampling area serving as buffer distance from the perimeter of the landslide was also tested. The results using a buffer distance of 100 m were not significantly different than the results obtained using 500 m. This observation allows to infer that the quantity of samples on interpolation methods that touch the samples have little influence on the interpolated results, therefore, 100 m was used. A representative example of the results utilized to select the most suitable interpolation method to model the pre-deformation surface of the landslides is observed in Fig. 5.9.

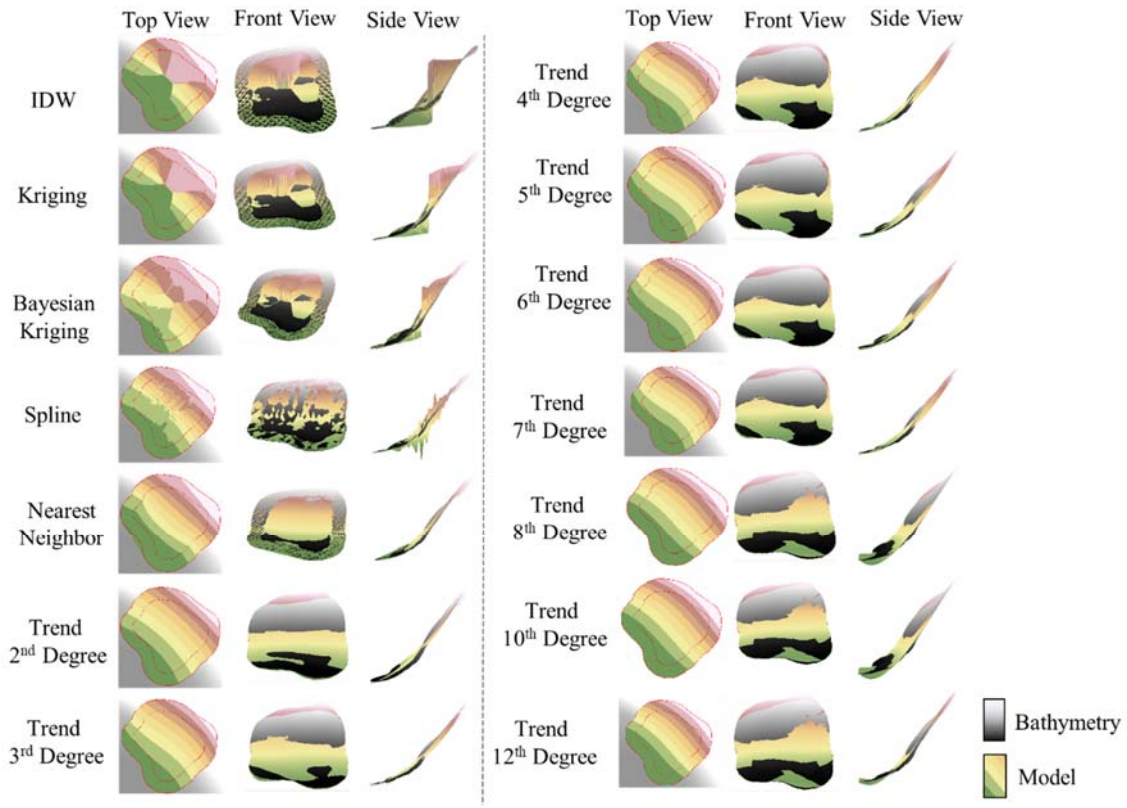

Fig. 5.9 Modeled interpolation surfaces for representative landslide.

From the top, front and side views shown in Fig. 5.9 it is observed that the IDW, Kriging and Bayesian Kriging methods interpolated points with respect to the closest value, creating an un-natural steep surface in the center of the interpolation zone that represents the most unlikely original configuration of the bathymetry before any displacement occurred. Spline returned wobbling features in the interpolation zone that respond to small irregular patterns in the sampling ring, which also produces an unlikely estimation of the original conditions of the slope. The nearest neighbor shows results that represent a qualitatively better approximation to the pre-slide surface since it can be observed a gap of volume on top of the slope (model on top of bathymetry suggesting a mobilized

material), and a small accretion of material at the toe of the landslide (bathymetry on top of model depicting accumulation of sediment). It is also observed that the model is touching the training points that are in the outer ring of the landslide. The trend interpolation series provide smooth surfaces without sharp changes, but does not touch the training points selected in the outside ring of the landslide. In all the front and side views of the trend series it is noticed that the model is beneath the bathymetry surface at the crown of the landslide, above the bathymetry at the middle, and beneath again at the toe. This behavior suggests an alternation pattern of (1) accumulation (top of landslide), (2) mobilization (middle of landslide) and (3) accumulation (toe of landslide), which is not consistent with the physical mechanism of landslides. Therefore, Nearest Neighbor interpolation method was selected to compute the heights of the sliding mass of sediment.

As mentioned before, it is assumed that the depth of landslide failure can be captured by the difference between the original slope configuration (modeled surface) and the post-failure surface (bathymetry) in the mobilized zone, where the volume of sediment is absent. A map algebra tool from ArcGIS was used to obtain this difference between the two raster surfaces, and a point feature class was used to extract the differential values, considered to contain the height of the landslide sediment mass. Fig. 5.10-A shows a relative frequency histogram of 60,559 points within the 11 sampled landslides retrieved using Natural Neighbor interpolation where the model rests above the bathymetry. The exponential shape of the relative histogram is naturally expected, since the depth distance between the model and the bathymetry is zero at the perimeter of the landslide, and it increases towards the center of the landslide, creating a higher frequency of zero height

differences in the samples. However, since the variable *H* is modeled with the purpose of studying landslides, the probability of having a failure with zero depth should be zero. Given this constrain, Wang and Huang (2013) and Das (2016), used a lognormal distribution to describe the behavior of this variable. Hence, a lognormal probability distribution was selected to describe the estimated *H* values, with a mean of 1.47 m, a standard deviation of 1.39 m, and 98.6% of values less or equal to 5 m. An empirical cumulative density function was also used to compare the behavior of the data and the lognormal model (Fig. 5.10-B).

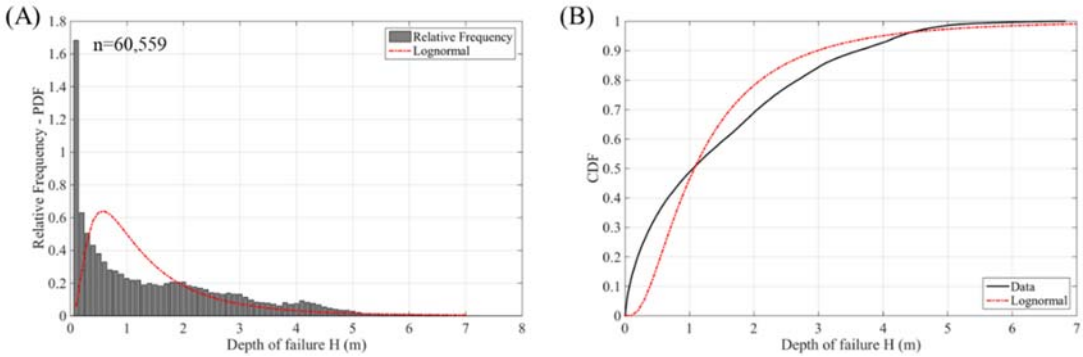

Fig. 5.10 (A) Relative frequency of H, lognormal PDF, (B) empirical and lognormal CDF of H.

For the section of the experimental design where the probability of failure is tested for different depths, the statistical descriptors of the variable *H* were adjusted using the observed mean and standard deviation for each depth interval, as seen in table 5.2.

Table 5.2 First order statistics of H for ranges of depth.

Depth (m)	Mean (m)	Standard deviation (m)
0 – 1	0.35	0.29
1 – 2	1.49	0.09
2 – 3	2.46	0.29
3 – 4	3.45	0.30
4 – 5	4.40	0.07

Slope Angle (α)

The slope of the modelled surfaces of the selected eleven landslides was used to define the probability distribution of the slope angle. Fig. 5.11-A shows the relative frequency of the data, which is a unimodal asymmetric distribution skewed to the right, with 97% of slope angles between 0 and 10 degrees. The mean of the slope samples is 4.23° with a variance of 6.58°. A lognormal probability distribution was used to describe this dataset given the restriction that this parameter requires probability values to be larger than zero. This assumption is consistent with previously implemented approaches (Wang and Huang 2013; Das 2016) for assessing the prior distribution of the slope angle α. The lognormal CDF shows to be closely describing the shape of the empirical data (Fig. 5.11-B).

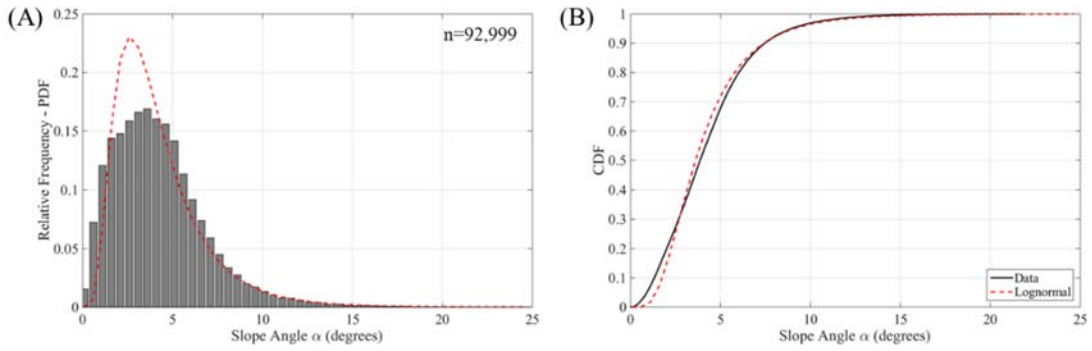

Fig. 5.11 (A) Relative frequency of α, lognormal PDF, (B) empirical and lognormal CDF of α.

Pseudo-static seismic coefficient (k)

The pseudo-static seismic coefficient was firstly proposed by Terzaghi in 1950 as a constant and permanent horizontal force in the failure direction to be included in the limit-equilibrium slope stability analysis due to a potential seismic event (Jibson 2001). He defined k as a horizontal seismic ground acceleration divided by earth's gravity acceleration, g. Hynes-Griffin and Franklin (1984) suggested a conservative adaptation to Terzaghi's method, expressed as $k = 0.5 \times PGA/g$, where PGA is the peak ground acceleration. A more comprehensive method is described by Briaud (2013), which is an adaptation of a technique proposed by Kavazanjian et al. (2011). This method takes under consideration the type of soil, height of landslide and PGA, resulting in a more site-oriented assessment of the seismic coefficient to use for slope stability analysis. Regional information about short and 1 second period spectral acceleration (S_s, S_1), and peak ground accelerations reported in the area were collected from sources such as the Global Seismic Hazard Assessment Program (GSHAP) (Danciu and Giardini 2015), USGS-US Department of the Interior (Jenkins et al. 2010), and USGS (2016) Geologic Hazards Science Center (2016). The gathered information is summarized in table 5.3.

Table 5.3 Peak ground acceleration (PCA), short period spectral acceleration (S_s), and one second period spectral acceleration (S_1) data.

Name and Title	PGA (m/s^2)	PGA (g)	Ss (g)	S_1 (g)
Jenkins et al. 2010. USGS-Seismicity of the Earth 1900–2010	1.6	0.16		
Danciu and Giardini 2015. Global Seismic Hazard Assessment Program-GSHAP legacy	2			
USGS 2016. Worldwide Seismic Design Tool (Beta)			1	0.47
			0.95	0.38
			0.86	0.35
			1.44	0.68
			1.37	0.55

To obtain the estimated value of k using the method described by Kavazanjian et al. (2011), the site was classified as type E due to (1) the high plasticity of the soils, (2) the water content is larger than 40%, and (3) the soil display values of undrained shear strength lower than 25 kPa. The pseudo-static seismic coefficient can then be expressed as $k = 0.5[1 + 0.01h\left(0.5\frac{F_v S_1}{F_{PGA}\times PGA} - 1\right)]\, F_{PGA} \times PGA$, where h is the height of the slope, S_1 is the 1 second period spectral acceleration, PGA is the peak ground acceleration, and F_v, F_{PGA} are site factors (Kavazanjian et al. 2011). The mean values of PGA and S_1, along with the curves shown in Fig. 5.12 were used to calculate the site factors F_{PGA} and F_v.

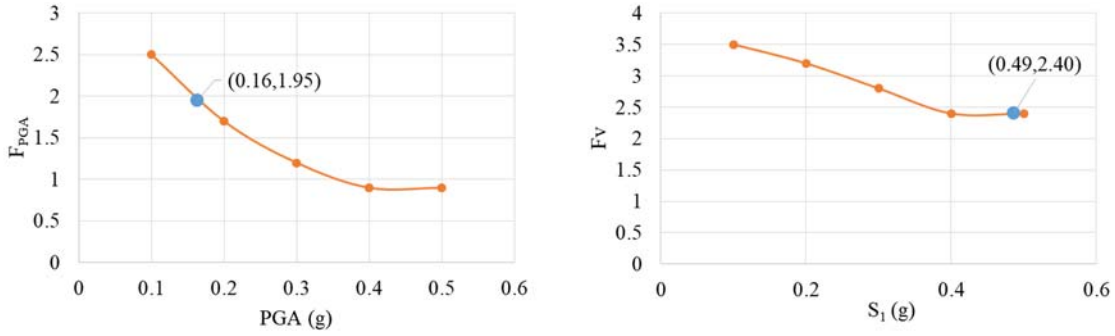

Fig. 5.12 Site factors used on peak ground acceleration estimates for site type E. Adapted from Kavazanjian et al. 2011.

The values of k summarized in table 5.4 display the estimates of the pseudo-static coefficient using the three methods described above. The Kavazanjian method was computed using a variety of slope height h values for every 20 cm up to 5 meters.

Table 5.4 Prior estimated values of k.

Method	***h* (m)**	***k***
Terzaghi (1950)	NA	0.184
Hynes-Griffin and Franklin (1984)	NA	0.092
Kavazanjian et al. 2011	0-1	0.1599*
	1-2	0.1613*
	2-3	0.1626*
	3-4	0.1639*
	4-5	0.1653*

*Averaged values within the interval h.

These values provide a small set of evidence with mean value 0.16 and a standard deviation of 0.014. A lognormal distribution was used to model the prior distribution of this variable, as seen in Fig. 5.13.

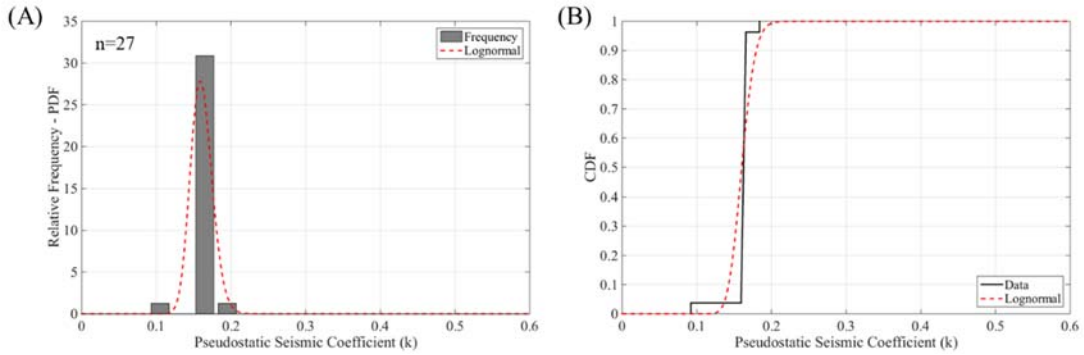

Fig. 5.13 (A) Relative frequency of k, lognormal PDF, (B) empirical and lognormal CDF of k.

Unit Weight (γ_{sub}, γ_{sat})

Values of submerged unit weight (γ_{sub}) are reported on the CPT logs at various depths. The samples used to define the prior distribution of this variable were collected from the top 5 m of sediment given that ~99% of the modeled failure depths occurred in such interval. A total of 47 observations were retrieved from the available dataset. The first approach to assess the behavior of this variable consisted on the examination of its dependency to the depth through the cross plot observed in Fig. 5.14. The response of the variable does not only lacks a trend with respect to the depth of the sediment, but also lacks a distinctive signature for different boreholes, suggesting that it is reasonable to assume that all the samples can be considered as part of the same population.

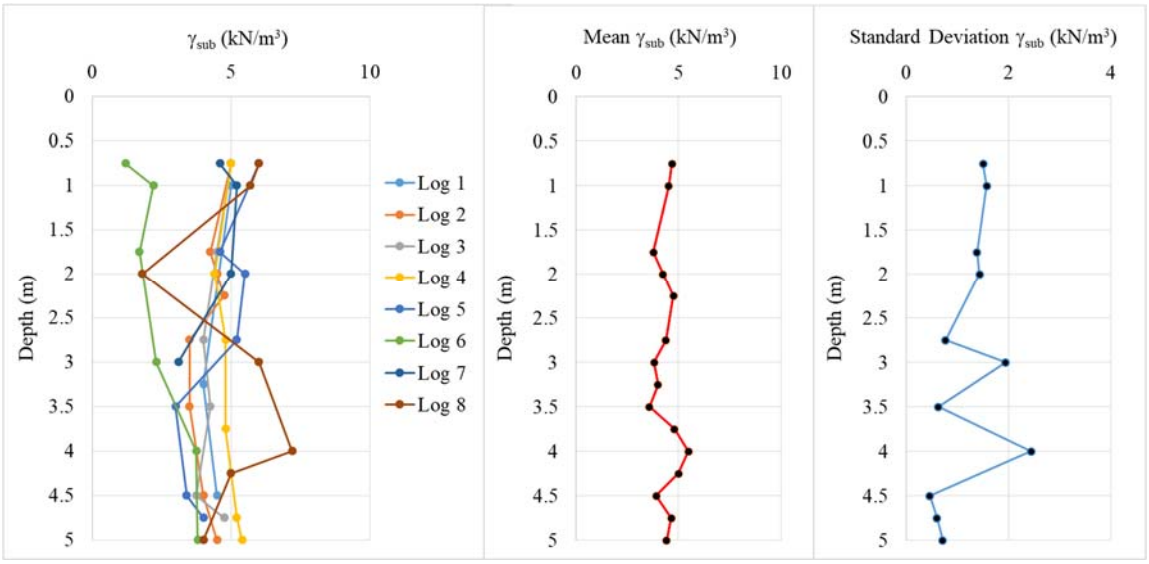

Fig. 5.14 Submerged unit weight (γ_{sub}) with respect to depth retrieved from CPT logs

The prior distribution of γ_{sub} is illustrated in Fig. 5.15, where the relative frequency bar plot shows an asymmetric unimodal behavior with a mean value of 4.33 kN/m^3 and a standard deviation of 1.20 kN/m^3. A lognormal distribution was used to describe this variable given that the unit weight is always a positive value (Wang and Huang 2013; Das 2016).

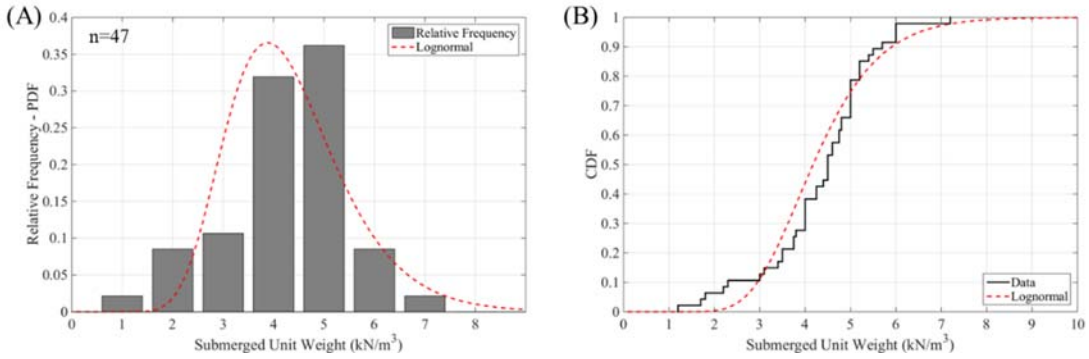

Fig. 5.15 (A) Relative frequency of γ_{sub}, lognormal PDF, (B) empirical and lognormal CDF of γ_{sub}.

Since the submerged unit weight variable can be expressed as $\gamma_{sub} = \gamma_{sat} - \gamma_w$, where γ_w is the unit weight of water (Terzagui and Peck 1967), the prior probability distribution of the variable γ_{sat} was computed based on the available values of γ_{sub}. The relative frequency and lognormal PDF describing this variable are the same as γ_{sub}, but shifted 9.8 units to the right, with mean 14.14 kN/m^3, and standard deviation 1.20 kN/m^3 (see Fig. 5.16).

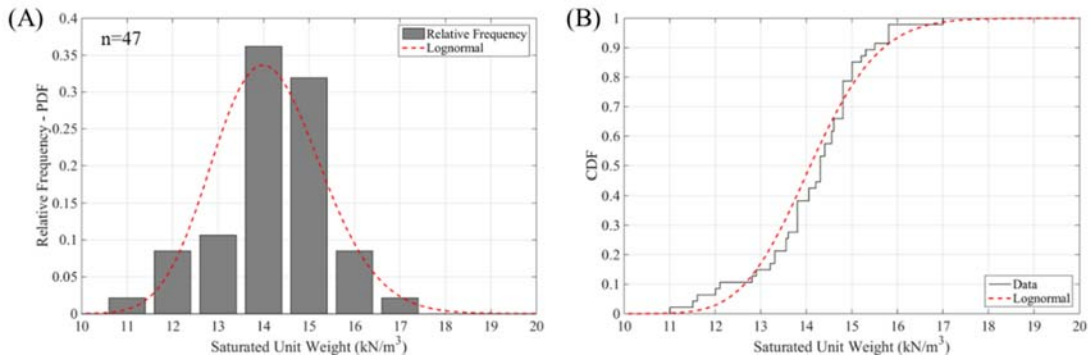

Fig. 5.16 (A) Relative frequency of γ_{sat}, lognormal PDF, (B) empirical and lognormal CDF of γ_{sat}.

Observations of Su

A total of 72 laboratory results of the undrained shear strength were also retrieved from the first 5 m of the soil profile surveyed during the CPT testing, with mean 8.98 kPa and a variance of 12.86 kPa. A lognormal distribution was used to model the behavior of this variable given its non-negative nature (Griffiths and Fenton 2001; Wang and Huang 2013; Jiang et al. 2014, Das 2016). Under the experimental design's assumption that all samples belong to one population, the relative frequency, PDF, and CDF plots observed in Fig. 5.17 were used.

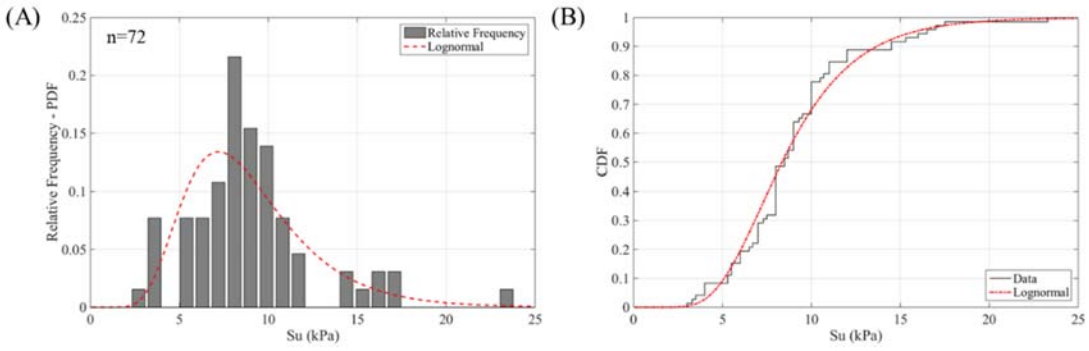

Fig. 5.17 (A) Relative frequency of one population of Su, lognormal PDF, (B) empirical and lognormal CDF of one population of Su.

However, the qualitative description of the soil properties, the modeled Su curves observed in Fig. 5.4, and the laboratory test results suggest that the undrained shear strength of the surveyed soils increases with depth. Fig. 5.18 illustrates the effect of the vertical stress on the Su variable as the modes of the relative frequency and lognormal PDFs shift towards stronger resistance values as depth increases.

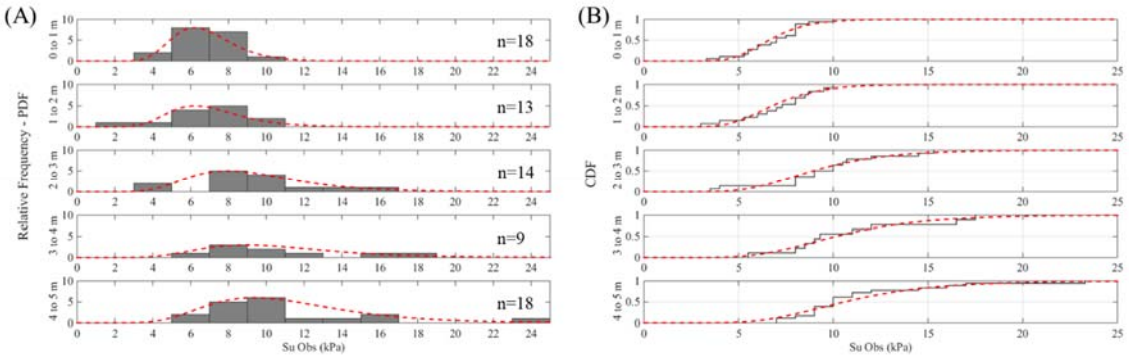

Fig. 5.18 (A) Relative frequency of 5 populations of Su, lognormal PDF, (B) empirical and lognormal CDF of 5 populations of Su.

The parameters used to implement the Bayesian model calibration for 5 populations of Su are summarized in table 5.5.

Table 5.5 First order statistics of Su at varying depths.

Depth (m)	Mean (kPa)	Standard Deviation (kPa)
0 – 1	6.81	1.69
1 – 2	7.06	2.07
2 – 3	9.46	3.30
3 – 4	10.81	3.96
4 – 5	11.27	4.10

Results

One Population 0 to 5 m

A total of 300,000 iterations were required to conduct the Bayesian model calibration at the limit state condition (FS→LS), and 600,000 using the FS as a random variable (FS→RV). A CoV of 0.3 was used in both experiments, with 5 and 20 Su samples as observed in Fig. 5.19. The standard deviation of the 5 and 20 random samples is 3.06kPa and 3.15kPa, respectively.

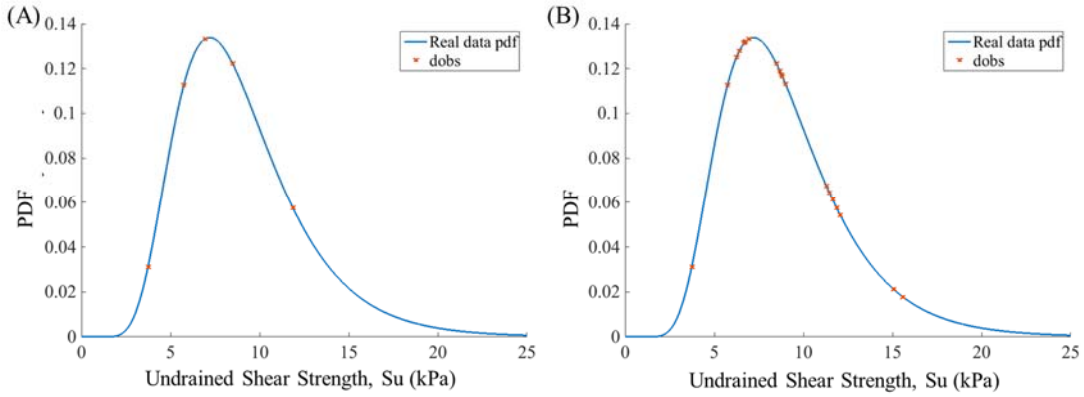

Fig. 5.19 Sampling of measured Su values. (A) 5 d_{obs} and (B) 20 d_{obs}.

FS at Limit State (LS)

As seen in Fig. 5.20, all the parameters of the infinite slope model reach uniform mean and variance values after 200,000 iterations (burn-in point). The proportion of accepted candidates was 20% and 13% for 5 and 20 samples, respectively.

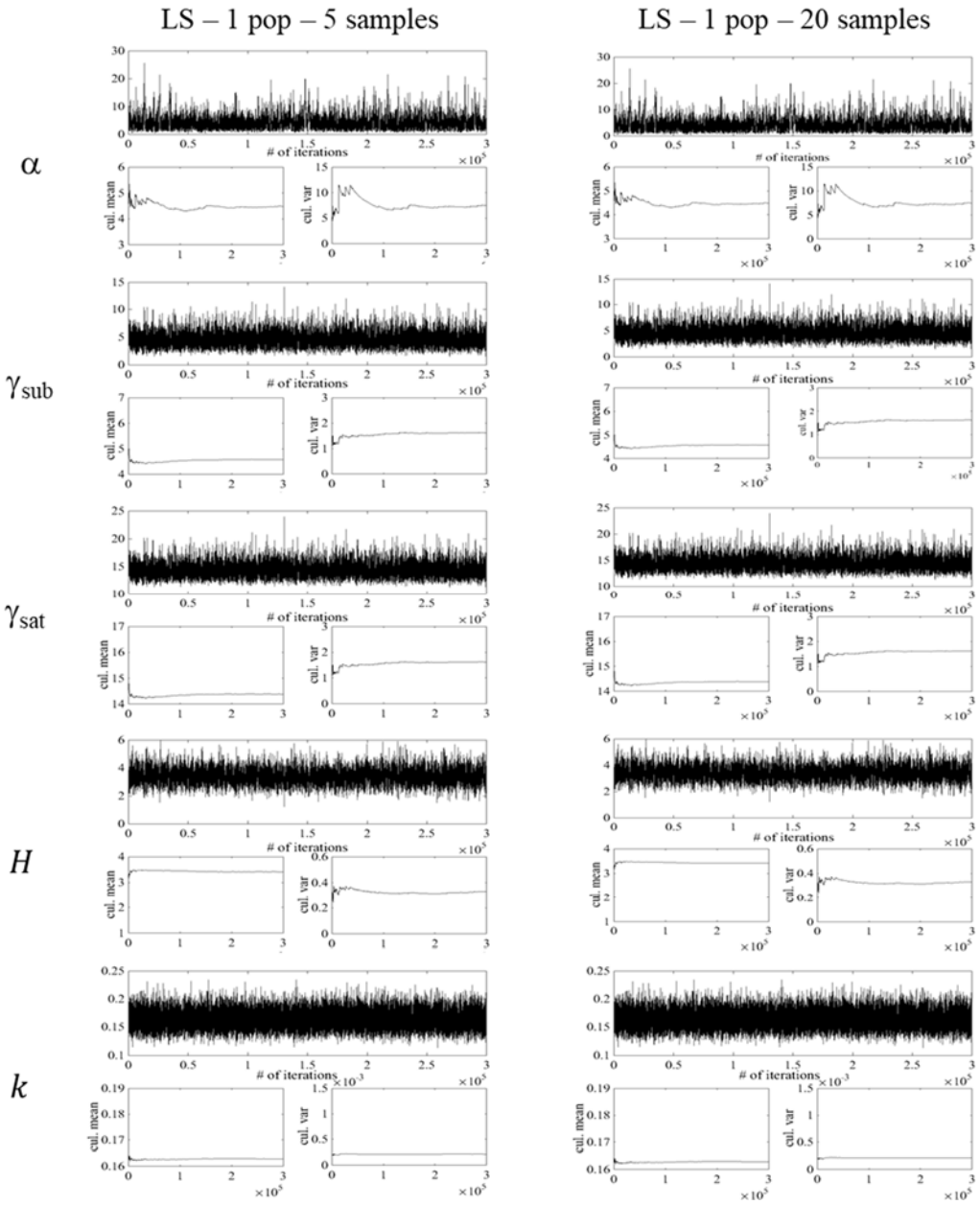

Fig. 5.20 Convergence plots of parameters for a FS at LS between 0 and 5 m depth.

The forward model using the prior set of parameters and the posterior estimates after the model calibration are compared with the experimental observations in Fig. 5.21. As aforementioned, these results are representative of the expected value of the physical

parameter Su estimated in the infinite slope model, and were used to model the prior and posterior populations of the forward model. The parameters using the initial state of evidence return lower values of undrained shear strength, while the results after the model calibration provide values closer to the observed experimental data retrieved from the laboratory tests. The mean Su sampled from the prior forward model is 3.8 kPa, while the posterior results have mean values of 6.7 kPa (5 samples) and 8.93 kPa (20 samples). Considering that the experimental observations yielded a mean value of 8.98 kPa, it is observed that the results obtained using 20 samples provide estimates closer to d_{obs} than the results obtained using 5 samples. Similarly, the standard deviation of the results from the calibrated model are 1.39 kPa and 0.71 kPa for 5 and 20 samples, respectively.

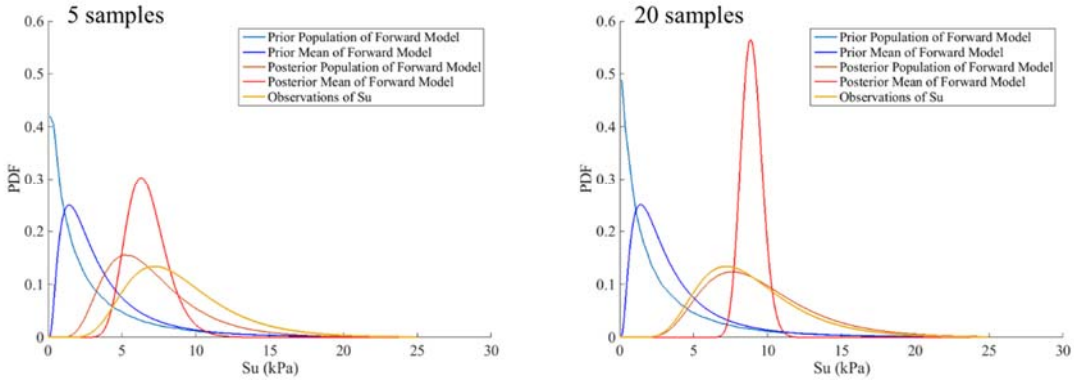

Fig. 5.21 Forward modeling and experimental observations of Su for a FS at limit state between 0 and 5 m depth.

The resulting SM was modeled using a normal distribution to illustrate the behavior of the population before and after the Bayesian model calibration (see Fig. 5.22). In both tested cases using 5 and 20 samples, the posterior SM curve is shifted towards lower domains

yielding higher probabilities of failure than the estimations of the prior forward model ($P(failure_{prior}) = 0.1$). The results using 5 samples provide a posterior probability of failure of 0.33, while the estimations obtained using 20 samples return a probability of failure of 0.54.

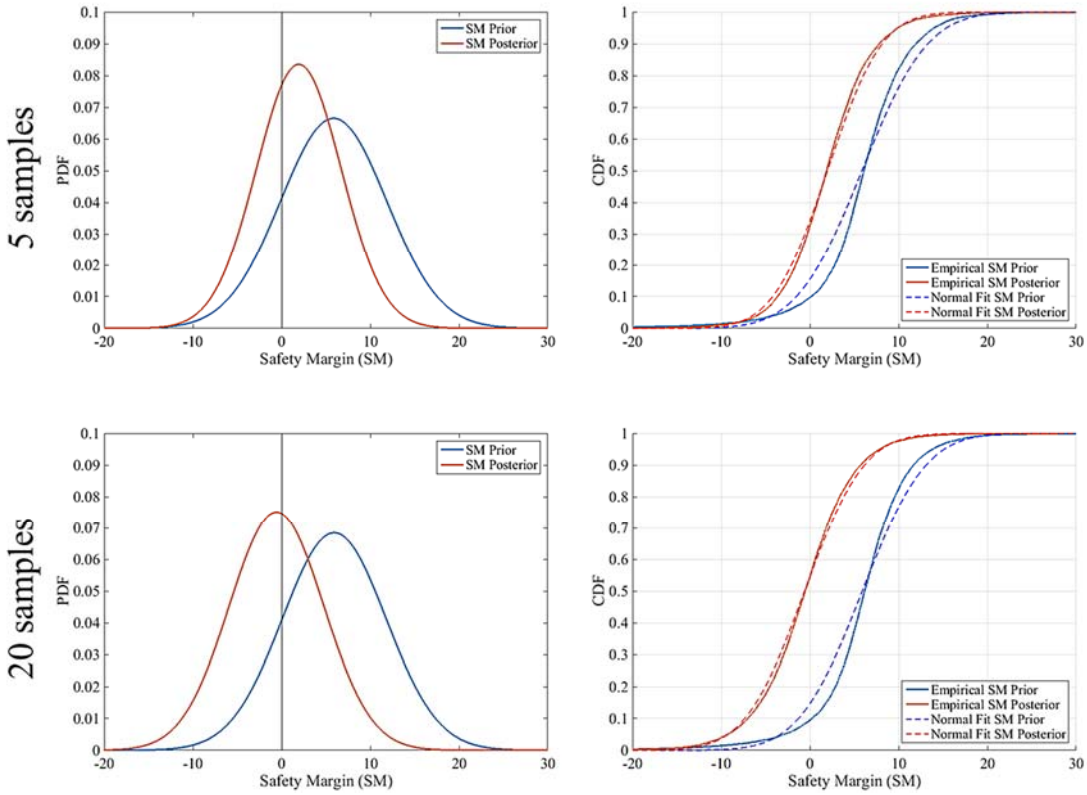

Fig. 5.22 PDF and CDF curves of SM from 0 to 5 m depth and a FS at limit state between 0 and 5 m depth.

Table 5.6 summarizes the first order statistics of the different states of evidence of Su. In both tested number of extracted observations, the results show a significant reduction of the uncertainty of the expected value of the modelled physical parameter with respect to the prior state of evidence without the Bayesian model calibration. The use of 20 samples produced an additional uncertainty reduction of almost half of the standard deviation of

the forward model of posterior Su obtained from taking 5 training points. This trend is not necessarily shown by the SM curves, given that they are extracted from the modelled population with the same standard deviation of the observations of Su.

Table 5.6 States of evidence of Su from 0 to 5 m depth and a FS at limit state.

Depth (m)	State of Evidence	5 Points		20 Points	
		Mean	Standard Deviation	Mean	Standard Deviation
0-5	Observations of Su	8.98	3.59	8.98	3.59
	Forward model of prior Su	3.80	3.66	3.80	3.69
	Population prior Su	3.80	3.59	3.80	3.59
	Forward model of posterior Su	6.70	1.39	8.93	0.71
	Population posterior Su	6.71	3.59	8.93	3.59
	Prior SM	5.86	5.76	5.87	5.79
	Posterior SM	1.93	4.85	-0.60	5.30

The prior and posterior state of evidence of the physical parameters used on the inverse model can be seen in Fig. 5.23 to 5.27. In these figures, it is observed that the most sensitive parameters to the Bayesian model calibration are saturated unit weight and sediment height, since their posterior state of evidence is shifted with respect to their prior distributions. Both of these updated parameters show higher values than initially estimated, given the condition of a factor of safety at limit state. The results are summarized in table 5.7.

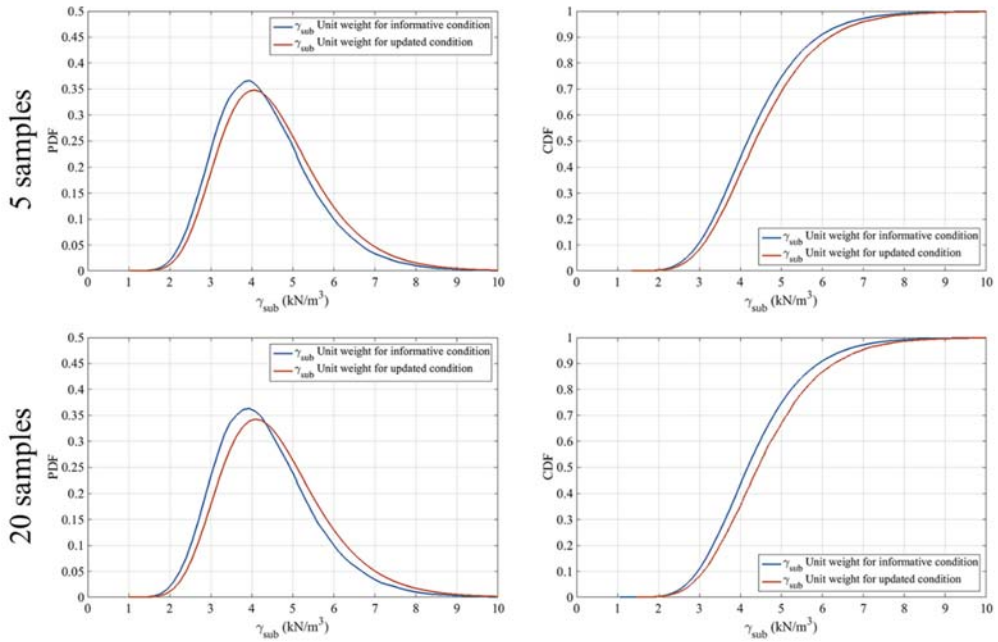

Fig. 5.23 PDF and CDF curves of submerged unit weight from 0 to 5 m depth and a FS at limit state.

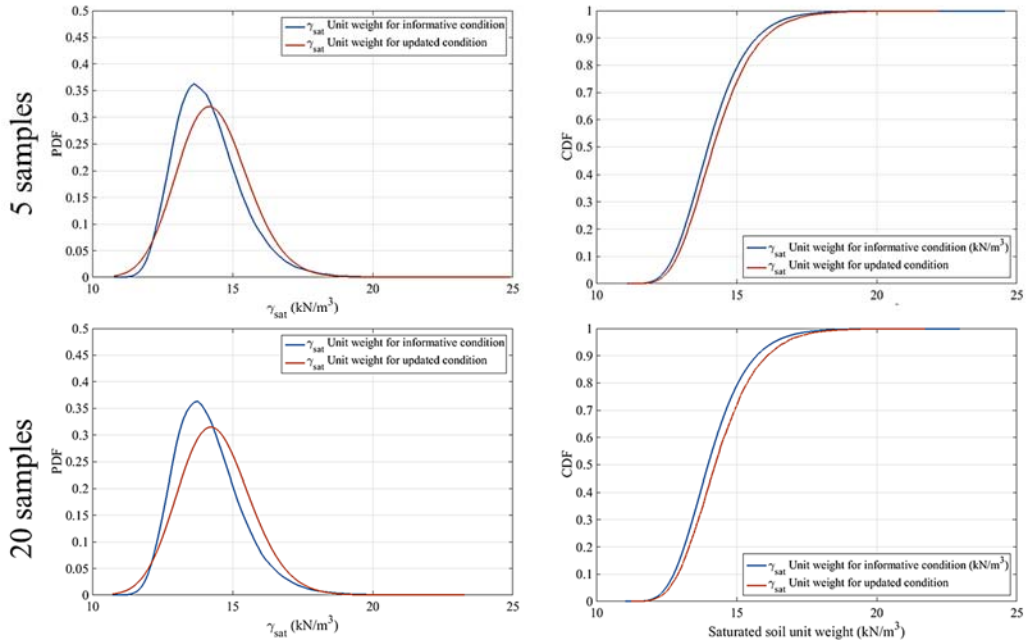

Fig. 5.24 PDF and CDF curves of saturated unit weight from 0 to 5 m depth and a FS at limit state.

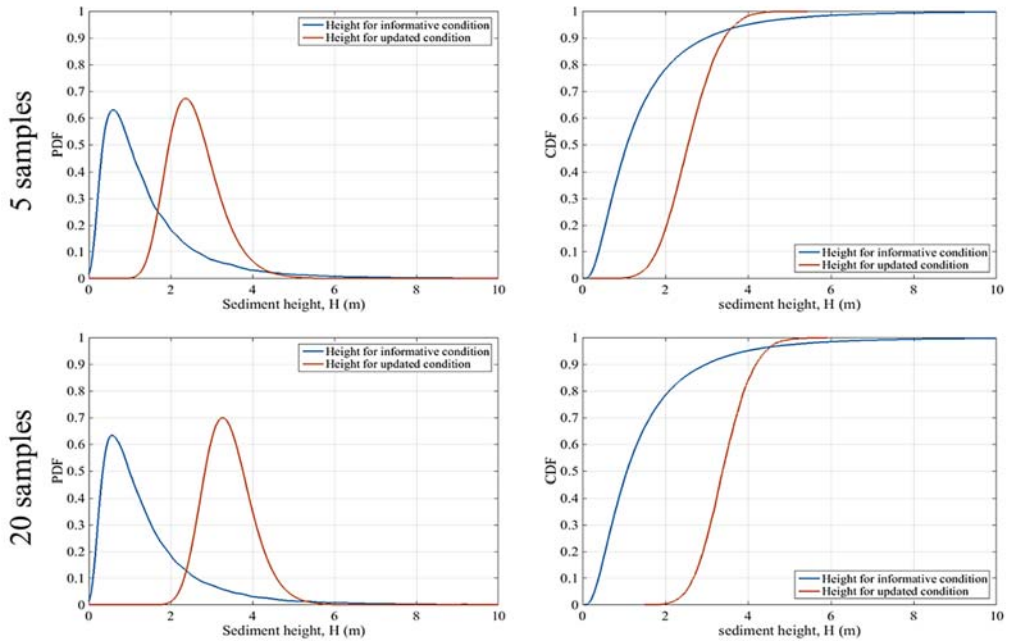

Fig. 5.25 PDF and CDF curves of sediment heights from 0 to 5 m depth and a FS at limit state.

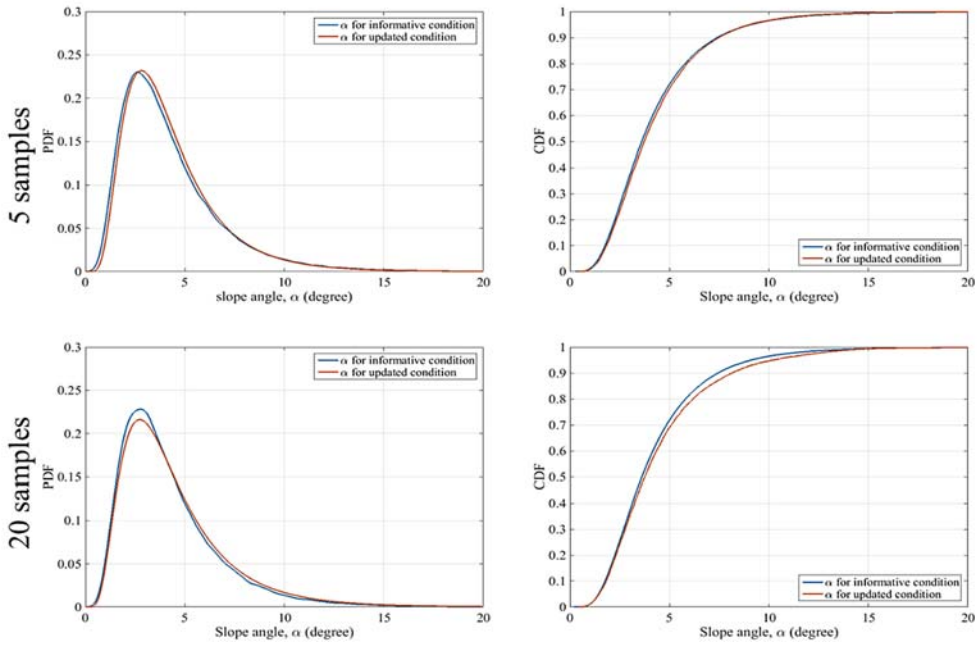

Fig. 5.26 PDF and CDF curves of slope angle from 0 to 5 m depth and a FS at limit state.

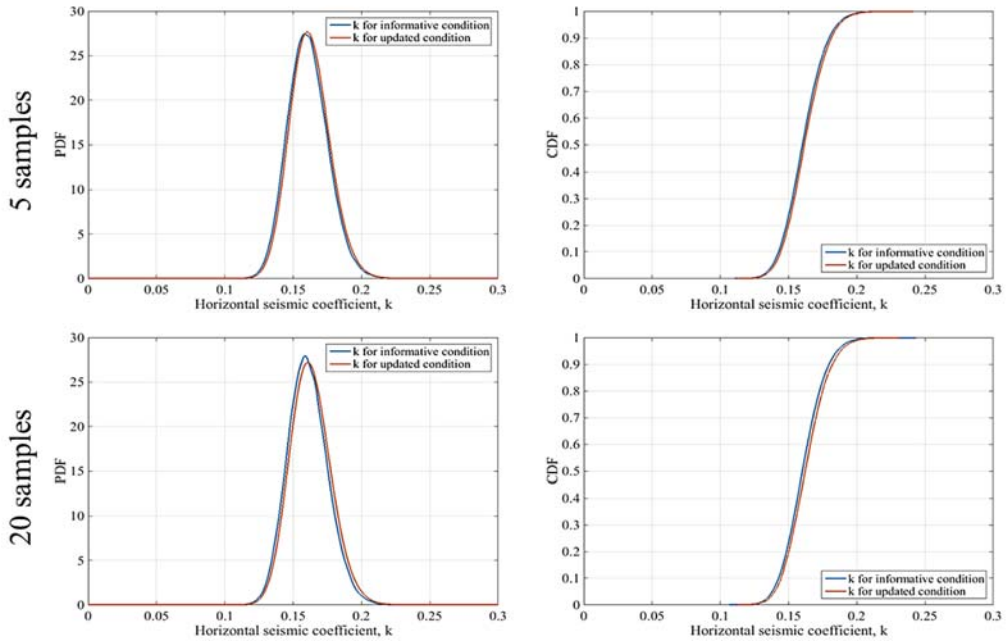

Fig. 5.27 PDF and CDF curves of seismic coefficient from 0 to 5 m depth and a FS at limit state.

Table 5.7 States of evidence of model parameters for 5 and 20 samples using one population and a FS at limit state.

Parameter	# Samples	Evidence	Mean	Standard Deviation
γ_{sub}	5 points	Prior	4.335	1.198
		Posterior	4.527	1.259
	20 Points	Prior	4.329	1.195
		Posterior	4.586	1.279
γ_{sat}	5 points	Prior	14.142	1.198
		Posterior	14.334	1.259
	20 Points	Prior	14.136	1.195
		Posterior	14.393	1.279
H	5 points	Prior	1.476	1.393
		Posterior	2.584	0.638
	20 Points	Prior	1.474	1.379
		Posterior	3.415	0.592
α	5 points	Prior	4.226	2.568
		Posterior	4.301	2.453
	20 Points	Prior	4.235	2.577
		Posterior	4.475	2.788
k	5 points	Prior	0.161	0.015
		Posterior	0.162	0.015
	20 Points	Prior	0.161	0.014
		Posterior	0.163	0.015

FS as a Random Variable (RV)

The experiment considering the FS as a random variable was implemented using 800,000 iterations and a CoV of 0.3, resulting in 9% of accepted candidates using 5 samples, and 5% for 20 samples. In Fig. 5.28 is observed that the samples reach a homoscedastic state after 700,000 iterations.

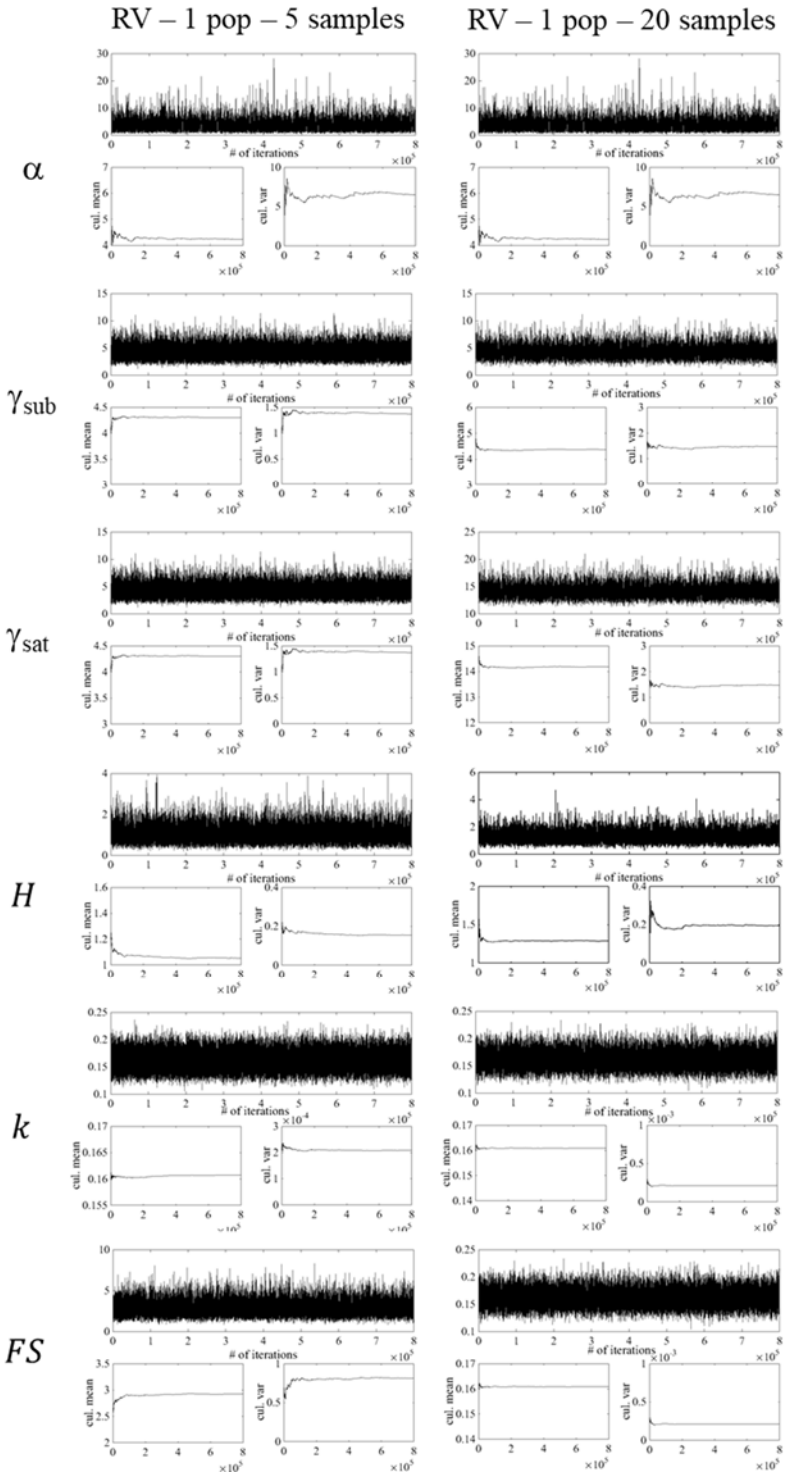

Fig. 5.28 Convergence plots of physical parameters for a FS as a random variable between 0 and 5 m depth.

The model calibration for this experiment shows that allowing the FS to behave as a random variable contributes with a substantial decrease of certainty on the prior's expected value and population of the undrained shear strength (see Fig. 5.29). However, this behavior is not detected on the posterior state of evidence, where it is observed that the inferences are approaching the experimental observations of Su. The standard deviation of the posterior forward model is significantly reduced when 20 samples instead of 5 are used for the calibration, while its posterior population nearly merges with the population of observed Su values.

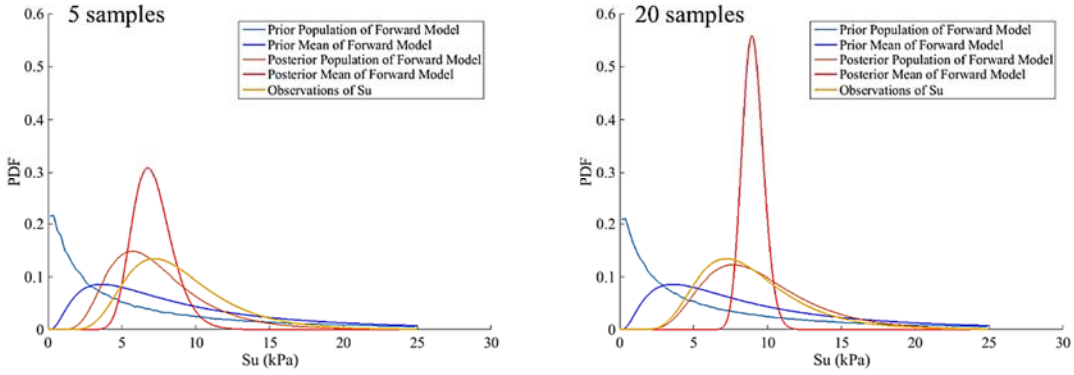

Fig. 5.29 Forward modeling and experimental observations of Su for a FS as a random variable between 0 and 5 m depth.

The increased variance of the expected value of Su before the model calibration returns a set of SM parameters with high levels of uncertainty with respect to the results obtained with the posterior forward model. The prior SM curves present outliers that skew the distribution towards large negative values, and its effect can be observed in the comparison between the empirical CPT curves and the normal distribution plots in Fig. 5.30. The

resulting probability of failure after the model calibration returns 0.37 and 0.55 for 5 and 20 samples, respectively.

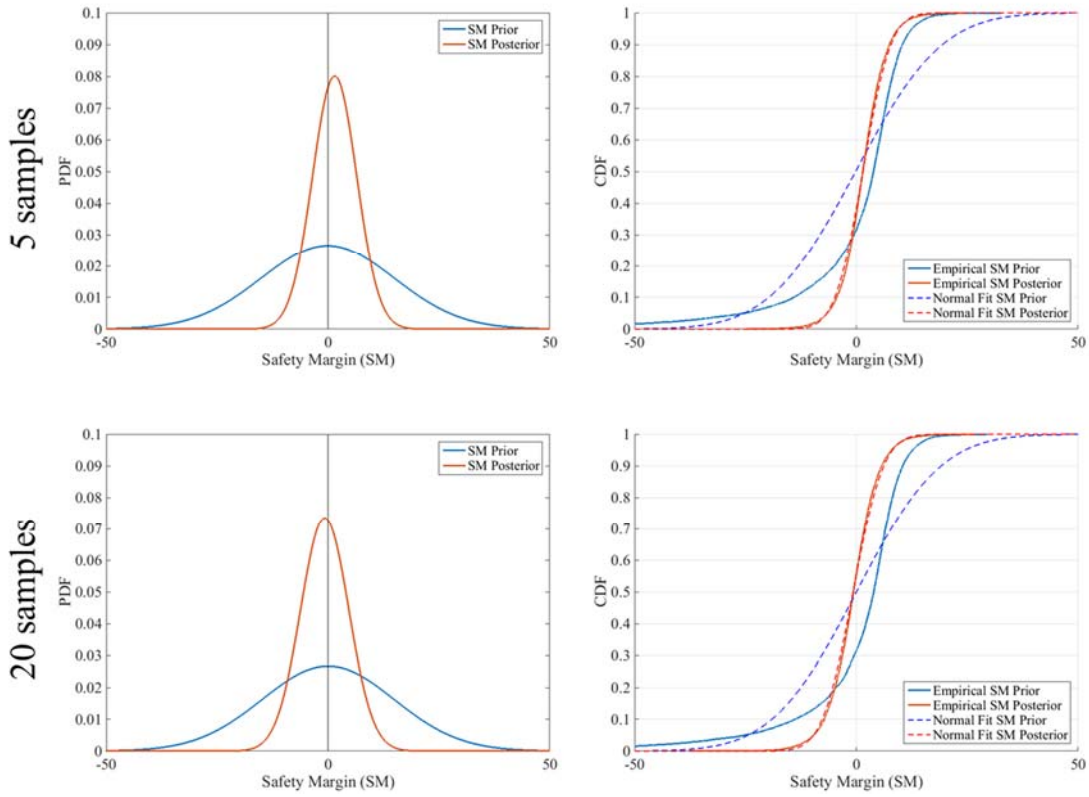

Fig. 5.30 PDF and CDF curves of SM from 0 to 5 m depth and a FS as a random variable between 0 and 5 m depth.

The contrasting behavior of uncertainty of the priors and posterior estimates are summarized in Table 5.8.

Table 5.8 States of evidence of Su from 0 to 5 m depth and a FS at limit state.

Depth (m)	State of Evidence	5 Points		20 Points	
		Mean	Standard Deviation	Mean	Standard Deviation
0-5	Observations of Su	8.98	3.59	8.98	3.59
	Forward model of prior Su	11.37	12.17	11.40	12.24
	Population prior Su	11.35	3.59	11.39	3.59
	Forward model of posterior Su	7.12	1.35	9.02	0.72
	Population posterior Su	7.11	3.59	9.02	3.59
	Prior SM	-0.12	15.28	-0.14	15.34
	Posterior SM	1.46	4.94	-0.69	5.33

The initial and updated states of the model's parameters are illustrated in Fig. 5.31 to 5.36, where it is noticed that the most sensitive variable to the model calibration is the sediment height, and to a lower degree, the saturated unit weight. The changes of the variable H includes an updated mean of 1.04 m (5 samples) and 1.25 m (20 samples), which is lower than the prior's estimation of 1.47 m, and an important reduction of the uncertainty of the variable, as seen in table 5.9. The random variable FS shows an updated condition without changes of mean, but with a slight reduction of its variance. The remaining variables show a minimum effect of the model calibration on their mean and standard deviation.

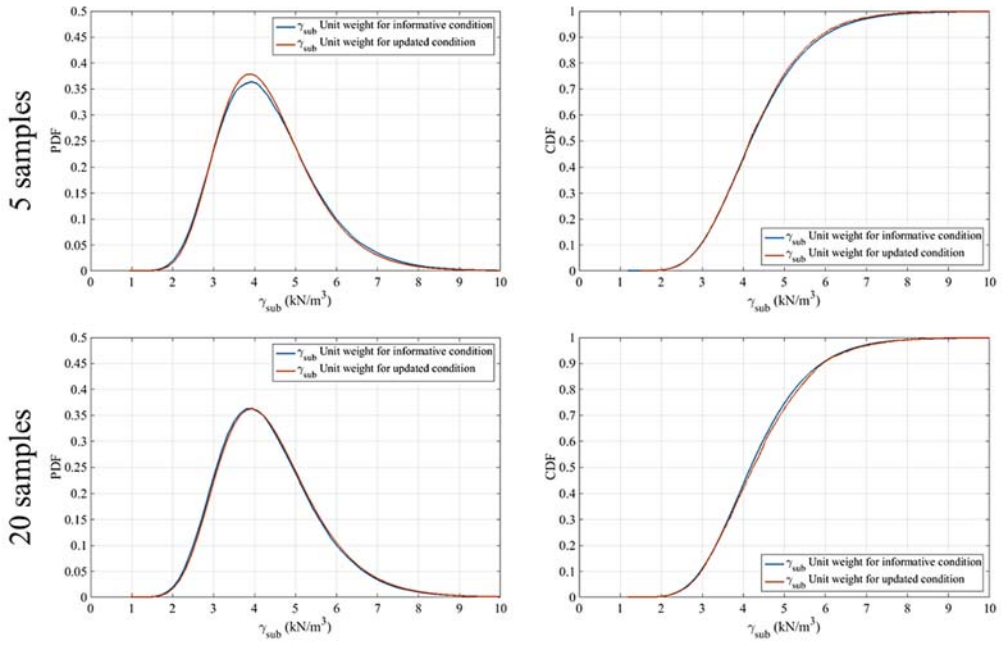

Fig. 5.31 PDF and CDF curves of submerged unit weight from 0 to 5 m depth and a FS as a random variable.

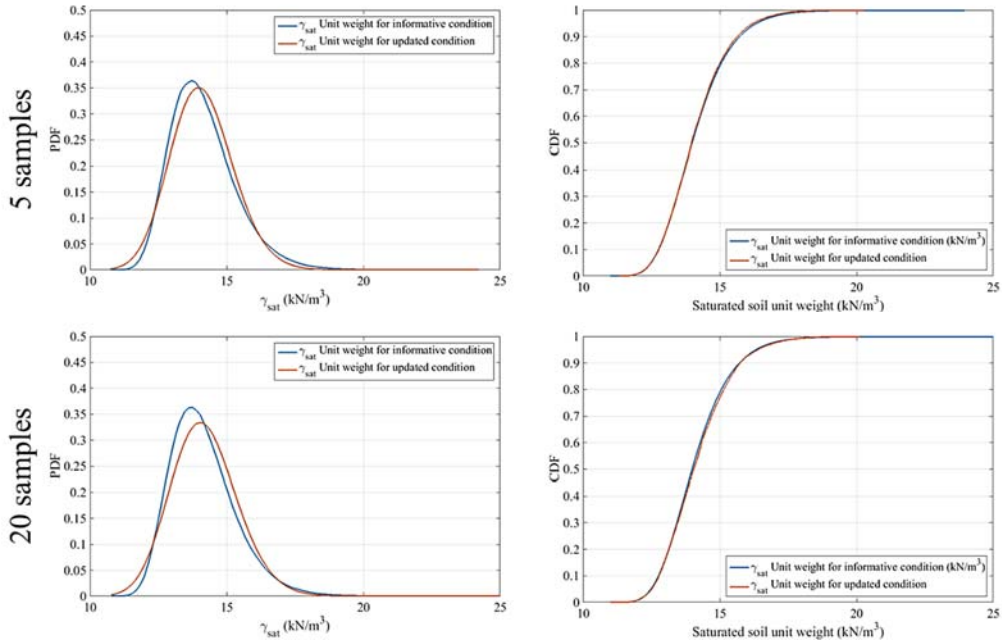

Fig. 5.32 PDF and CDF curves of saturated unit weight from 0 to 5 m depth and a FS as a random variable.

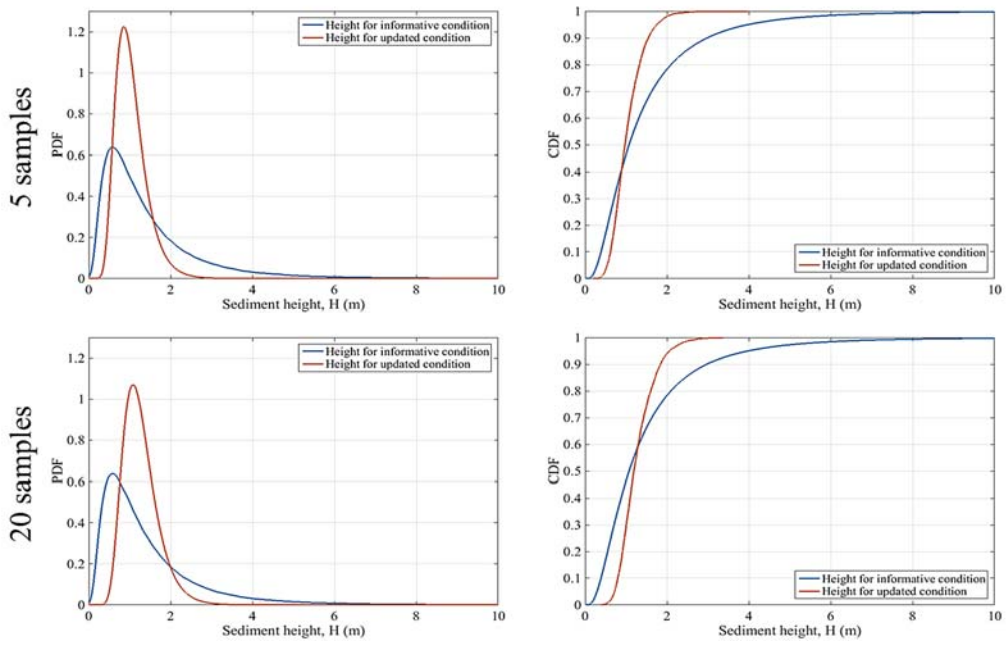

Fig. 5.33 PDF and CDF curves of sediment height from 0 to 5 m depth and a FS as a random variable.

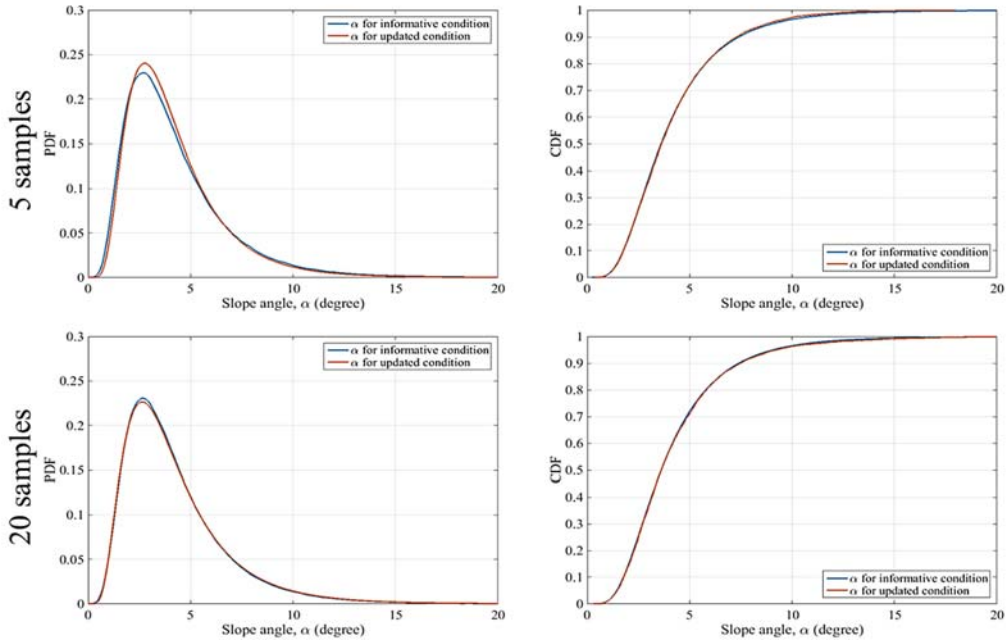

Fig. 5.34 PDF and CDF curves of slope angle from 0 to 5 m depth and a FS as a random variable

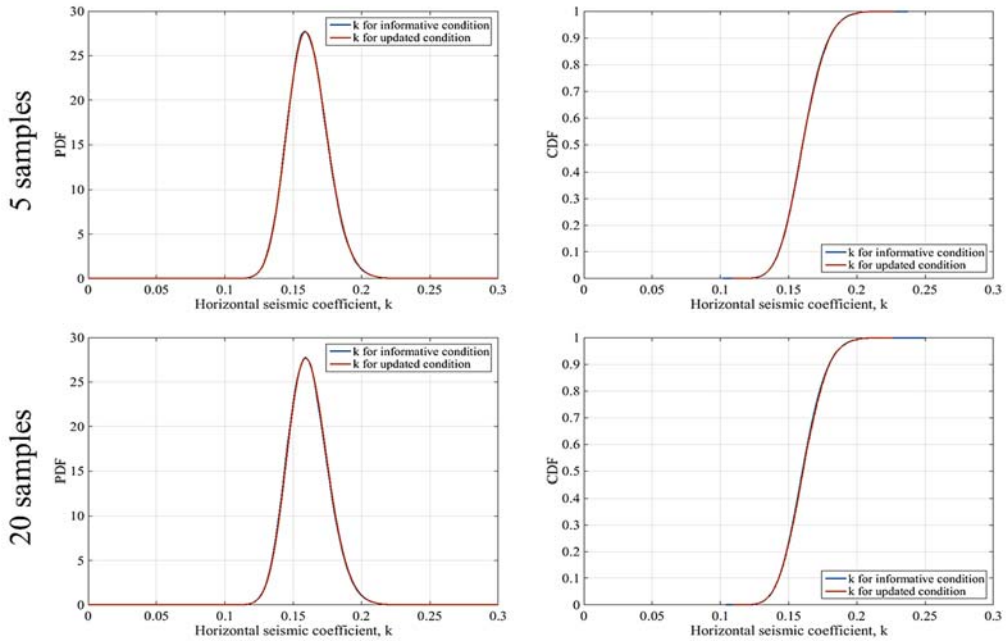

Fig. 5.35 PDF and CDF curves of seismic coefficient from 0 to 5 m depth and a FS as a random variable.

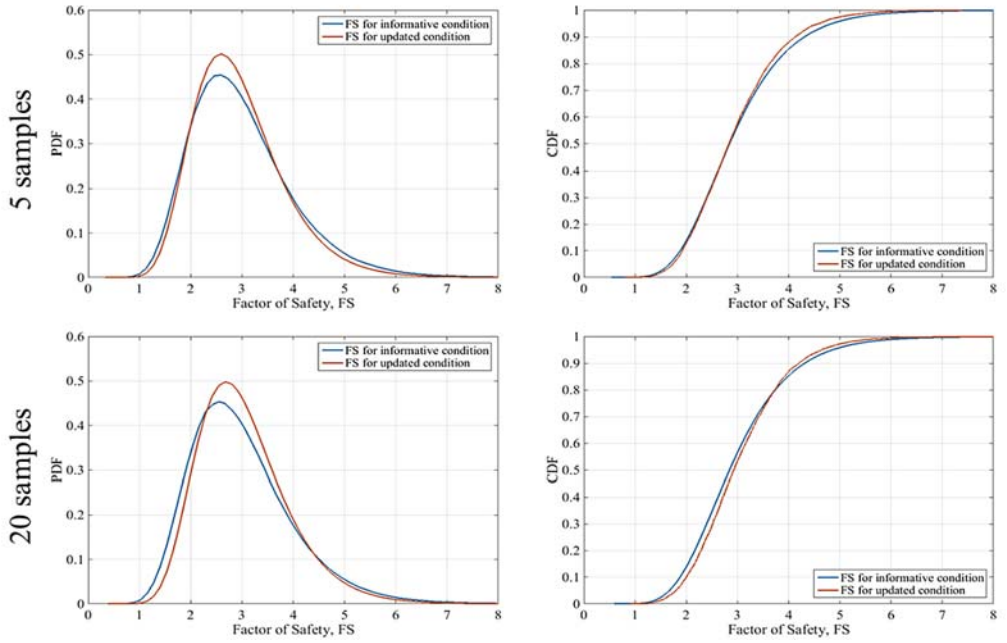

Fig. 5.36 PDF and CDF curves of factor of safety from 0 to 5 m dept.

Table 5.9. States of evidence of model parameters for 5 and 20 samples using one population and a FS as a random variable.

Table 5.9 States of evidence of model parameters for 5 and 20 samples using one population and a FS as a random variable.

Parameter	# Samples	Evidence	Mean	Standard Deviation
γ_{sub}	5 points	Prior	4.331	1.196
		Posterior	4.303	1.146
	20 Points	Prior	4.332	1.195
		Posterior	4.377	1.205
γ_{sat}	5 points	Prior	14.138	1.196
		Posterior	14.110	1.146
	20 Points	Prior	14.139	1.195
		Posterior	14.184	1.205
H	5 points	Prior	1.474	1.381
		Posterior	1.038	0.382
	20 Points	Prior	1.474	1.390
		Posterior	1.270	0.426
α	5 points	Prior	4.226	2.572
		Posterior	4.168	2.347
	20 Points	Prior	4.225	2.556
		Posterior	4.280	2.642
k	5 points	Prior	0.161	0.015
		Posterior	0.161	0.015
	20 Points	Prior	0.161	0.015
		Posterior	0.161	0.015
FS	5 points	Prior	2.998	0.998
		Posterior	2.948	0.886
	20 Points	Prior	2.999	1.000
		Posterior	3.039	0.887

Five Populations

The Bayesian model calibration was implemented at 5 ranges of depth considering the changes of the observed values of Su, using 5 and 20 samples from the prior distribution of the model's parameters, and a CoV of 0.3. The standard deviation of the observations extracted from the Su distribution at each depth used for testing the FS at limit state and as a random variable are presented in table 5.10. The results of the posterior forward model using 20 samples consistently returned lower levels of uncertainty with respect to the results obtained using 5 samples in all the experiments conducted in this study. Hereafter, the results displayed in this section are referring to the experiment using 20 samples.

Table 5.10 Standard deviation of samples extracted from 5 populations of Su.

Depth (m)	**# Samples**	**Standard deviation d_{obs}**
0-1	5	1.6108
	20	1.5305
1-2	5	1.9113
	20	1.8618
2-3	5	2.9198
	20	2.9303
3-4	5	3.4618
	20	3.508
4-5	5	3.587
	20	3.6293

FS at Limit State (LS)

A total of 600,000 iterations were required to reach homoscedasticity, and a burn-in point of 400,000 was used to extract the updated state of evidence of the studied parameters for a FS =1. The forward model of the prior and posterior inferences of Su for each studied discrete range of depth (Fig. 5.37) present a systematic uncertainty rise of the model predictions and of the modelled populations as the depth increases. The expected value of all the predictions also show an increase of the shear resistance with the depth increments. Yet, all the predictions of the posterior forward model stand out as the best estimates targeting the mean of the undrained shear strength, while the curves of the prior state of evidence flatten with larger depths. The modelled population of Su after the Bayesian model calibration overlaps the population of observed Su at all examined depth ranges.

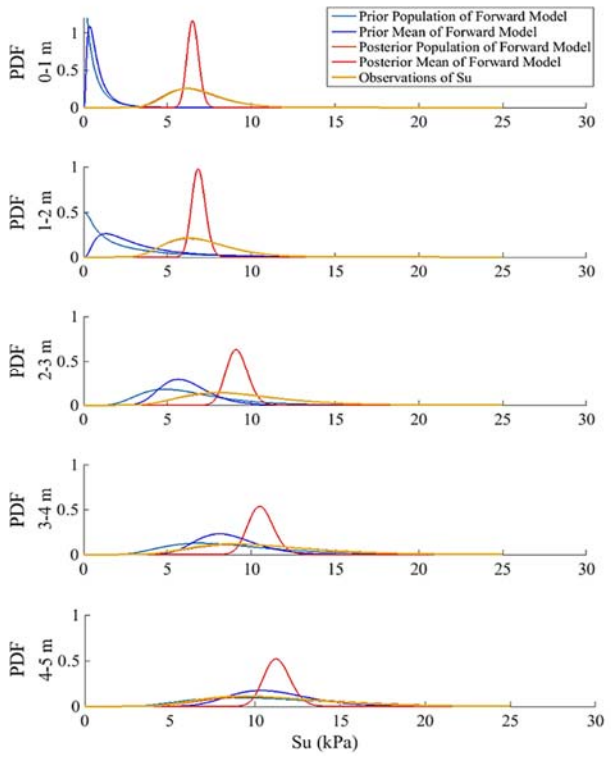

Fig. 5.37 Forward modeling and experimental observations of Su for a FS at LS for 5 populations of depth.

As the resistance and the load increases, it is observed that the SM shifts towards more conservative scenarios where the probability of failure increases with depth. The SM curves depicted in Fig. 5.38 also show a decrease of the uncertainty on the prior and posterior estimations. The mode of the SM after the model calibration is consistently close to zero, while the prior SM presents a behavior that decreases as depth increases. The probabilities of failure returned by this set of experiments are:

- $P(f_{prior}) = 0.11$, and $P(f_{posterior}) = 0.48$ between 0 and 1 m depth.
- $P(f_{prior}) = 0.25$, and $P(f_{posterior}) = 0.51$ between 1 and 2 m depth.
- $P(f_{prior}) = 0.30$, and $P(f_{posterior}) = 0.52$ between 2 and 3 m depth.

- $P(f_{prior}) = 0.37$, and $P(f_{posterior}) = 0.53$ between 3 and 4 m depth.
- $P(f_{prior}) = 0.43$, and $P(f_{posterior}) = 0.55$ between 4 and 5 m depth.

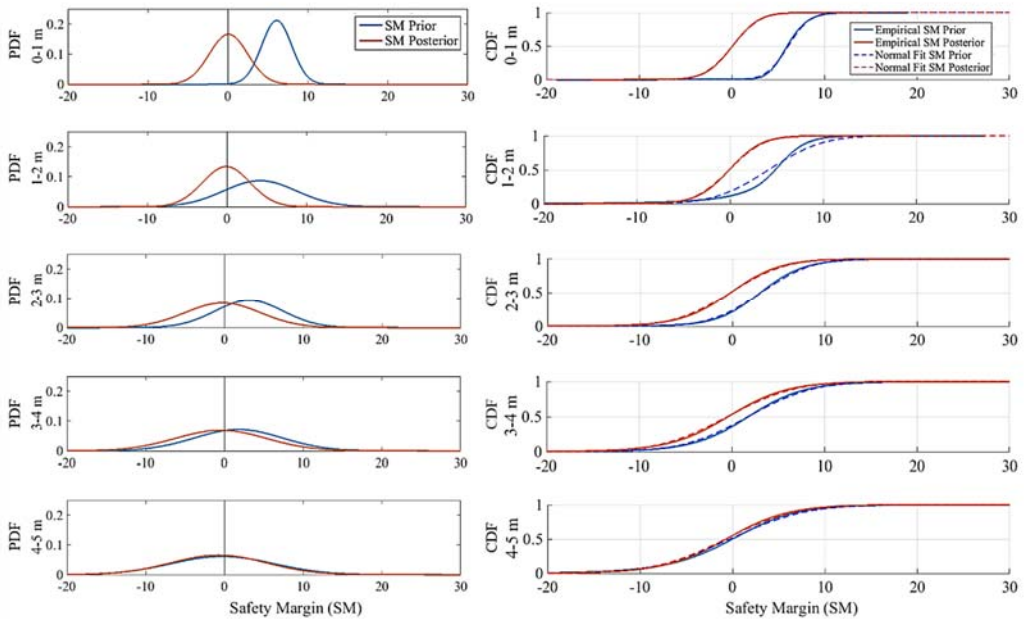

Fig. 5.38 PDF and CDF curves of SM for a FS at LS for 5 populations of depth

A summary of these results are shown in table 5.11.

Table 5.11 States of evidence of Su for a FS at limit state for 5 populations of depth.

Depth (m)	State of Evidence	20 Points	
		Mean	Standard Deviation
0-1	Observations of Su	6.81	1.69
	Forward model of prior Su	0.86	0.75
	Population prior Su	0.86	1.69
	Forward model of posterior Su	6.53	0.34
	Population posterior Su	6.53	1.69
	Prior SM	6.12	1.89
	Posterior SM	0.09	2.40
1-2	Observations of Su	7.06	2.07
	Forward model of prior Su	3.66	3.61
	Population prior Su	3.65	2.07
	Forward model of posterior Su	6.87	0.41
	Population posterior Su	6.87	2.07
	Prior SM	4.17	4.56
	Posterior SM	-0.08	2.98
2-3	Observations of Su	9.46	3.30
	Forward model of prior Su	6.16	1.49
	Population prior Su	6.16	3.30
	Forward model of posterior Su	9.16	0.64
	Population posterior Su	9.16	3.30
	Prior SM	3.12	4.32
	Posterior SM	-0.22	4.77
3-4	Observations of Su	10.81	3.96
	Forward model of prior Su	8.66	1.84
	Population prior Su	8.66	3.96
	Forward model of posterior Su	10.58	0.75
	Population posterior Su	10.58	3.96
	Prior SM	1.80	5.59
	Posterior SM	-0.43	5.78
4-5	Observations of Su	11.27	4.10
	Forward model of prior Su	11.11	2.43
	Population prior Su	11.11	4.10
	Forward model of posterior Su	11.31	0.77
	Population posterior Su	11.31	4.10
	Prior SM	-0.28	6.51
	Posterior SM	-0.74	6.05

The set of parameters retrieved during the Bayesian model inversion show consistently higher expected values than the parameters predicted by the priors. Fig. 5.39 to 5.43 display the variability of these parameters with respect to depth, where it is observed that the priors show no sensitivity to the depth changes, while the updated distributions adjust to the evidence of depth and Su. This calibration process makes the predictions of the Bayesian inversion to match the prior state of evidence at larger depths. It is also noted that the uncertainty of the updated parameters consistently decreases with higher depths.

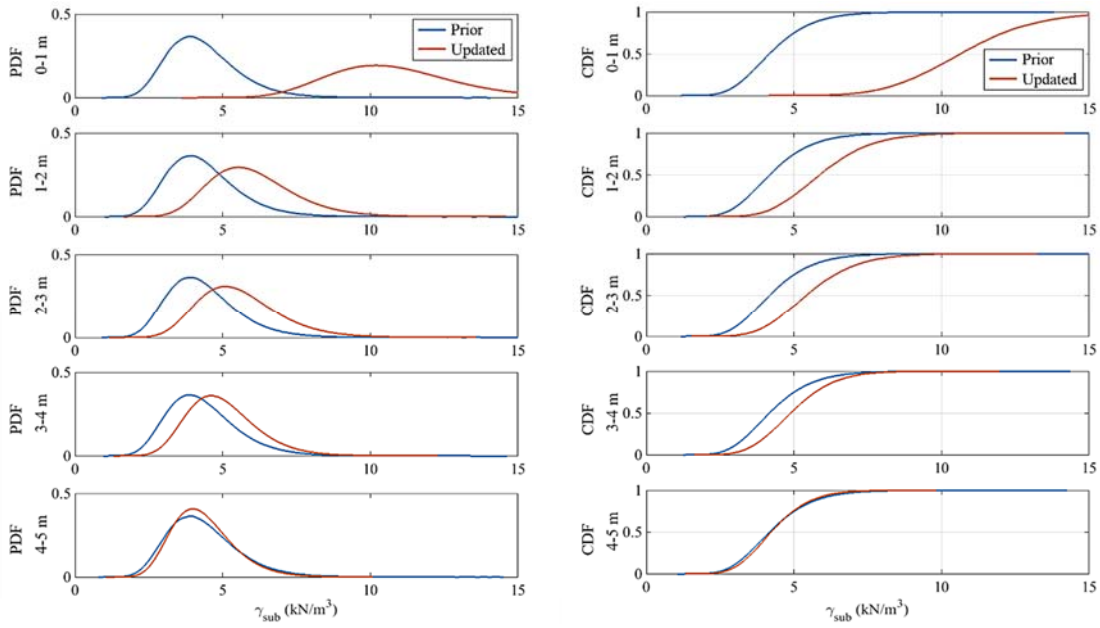

Fig. 5.39 PDF and CDF curves of γ_{sub} for a FS at LS for 5 populations of depth

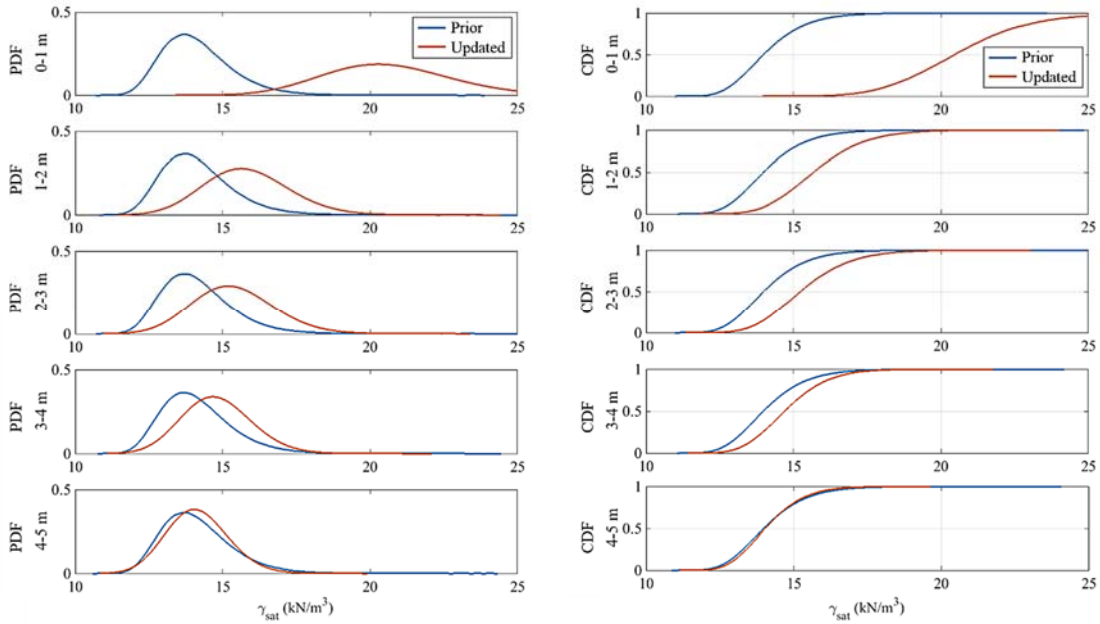

Fig. 5.40 PDF and CDF curves of γ_{sat} for a FS at LS for 5 populations of depth.

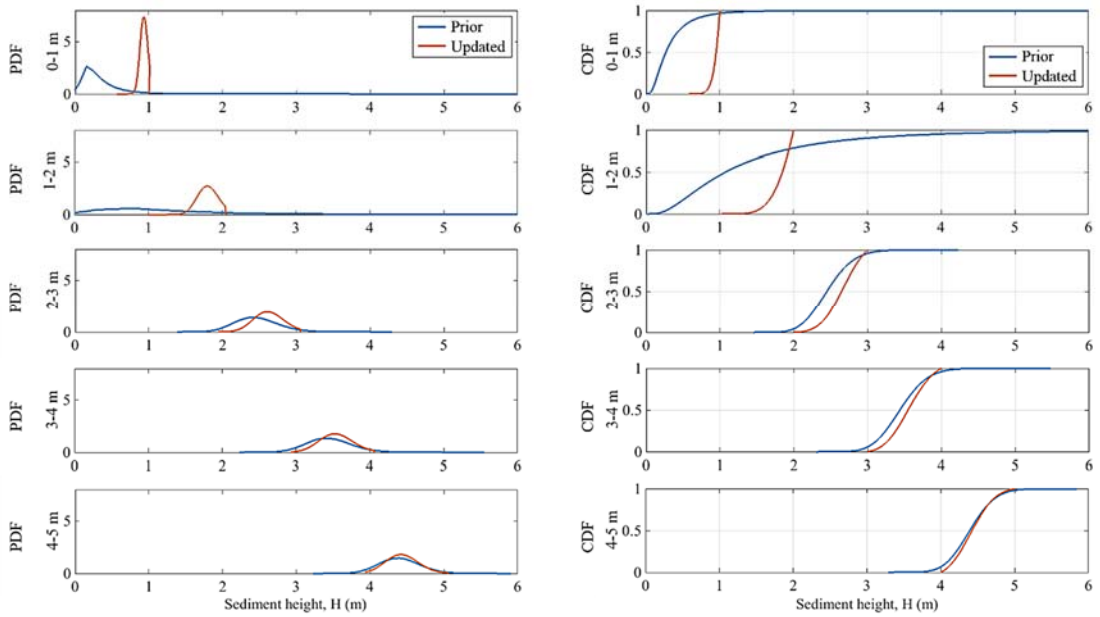

Fig. 5.41 PDF and CDF curves of H for a FS at LS for 5 populations of depth.

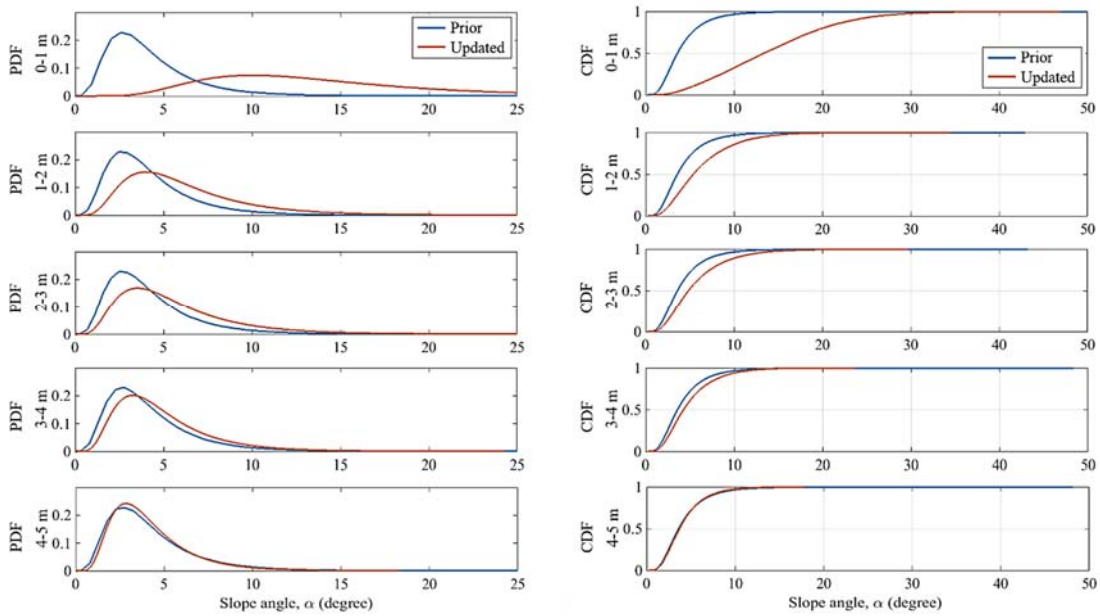

Fig. 5.42 PDF and CDF curves of α for a FS at LS for 5 populations of depth.

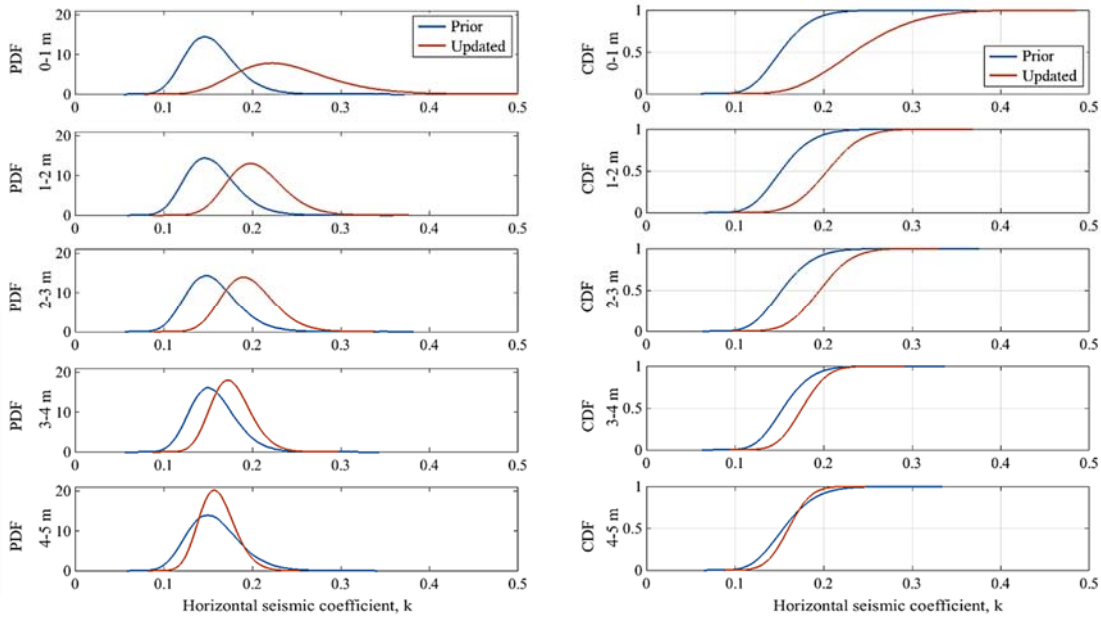

Fig. 5.43 PDF and CDF curves of k for a FS at LS for 5 populations of depth.

Tables 5.12 and 5.13 display a summary of the mean and standard deviation of the estimated parameters at different depth intervals.

Table 5.12 States of evidence of $\gamma_{sub}, \gamma_{sat}$ and H for 20 samples using five populations and a FS as at limit state.

Parameter	Depth (m)	Evidence	Mean	Standard Deviation
γ_{sub}	0-1	Prior	4.330	1.196
		Posterior	7.298	1.942
	1-2	Prior	4.332	1.192
		Posterior	5.154	1.371
	2-3	Prior	4.332	1.199
		Posterior	4.693	1.230
	3-4	Prior	4.332	1.195
		Posterior	4.336	1.105
	4-5	Prior	4.332	1.198
		Posterior	3.995	0.981
γ_{sat}	0-1	Prior	14.137	1.196
		Posterior	17.105	1.942
	1-2	Prior	14.139	1.192
		Posterior	14.961	1.371
	2-3	Prior	14.139	1.199
		Posterior	14.500	1.230
	3-4	Prior	14.139	1.195
		Posterior	14.143	1.105
	4-5	Prior	14.139	1.198
		Posterior	13.802	0.981
H	0-1	Prior	0.347	0.288
		Posterior	0.906	0.075
	1-2	Prior	1.494	0.295
		Posterior	1.655	0.190
	2-3	Prior	2.463	0.291
		Posterior	2.525	0.222
	3-4	Prior	3.451	0.299
		Posterior	3.463	0.230
	4-5	Prior	4.399	0.274
		Posterior	4.394	0.218

Table 5.13 States of evidence of α and k for 20 samples using five populations and a FS as at limit state.

Parameter	Depth (m)	Evidence	Mean	Standard Deviation
α	0-1	Prior	4.227	2.569
		Posterior	8.717	5.752
	1-2	Prior	4.224	2.571
		Posterior	5.252	3.219
	2-3	Prior	4.231	2.572
		Posterior	4.715	2.894
	3-4	Prior	4.225	2.557
		Posterior	4.264	2.533
	4-5	Prior	4.223	2.565
		Posterior	3.775	2.043
k	0-1	Prior	0.154	0.029
		Posterior	0.220	0.042
	1-2	Prior	0.155	0.029
		Posterior	0.182	0.030
	2-3	Prior	0.156	0.029
		Posterior	0.170	0.027
	3-4	Prior	0.156	0.026
		Posterior	0.158	0.022
	4-5	Prior	0.157	0.030
		Posterior	0.145	0.021

FS as a Random Variable (RV)

This experiment was conducted using 1,000,000 iterations and a CoV of 0.2. The selected burn-in point was 900,000. The results obtained from the forward model show that the certainty level achieved by the posterior state of evidence at all depths is significantly larger than the results retrieved from the priors, and that their mean trend increases with depth. The observations of Su are closely replicated by the modelled population of the posterior forward model. The distribution of the prior populations are shown to be highly

sensitive to the increase of uncertainty of the Su values derived from laboratory experiments. These remarks are illustrated in Fig. 5.44.

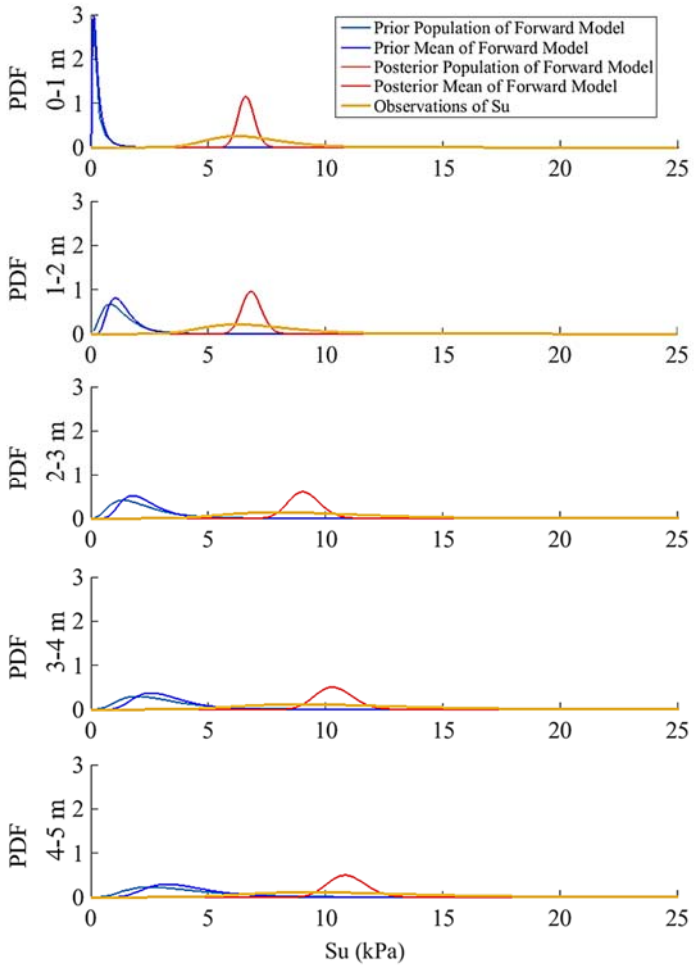

Fig. 5.44 Forward modeling and experimental observations of Su for a FS as a RV for 5 populations of depth and 20 samples.

The increased standard deviation of the estimated load populations is also captured by the SM curves shown in Fig. 5.45. In this figure, it is noted that the prior estimate of the forward model produces lower values of SM as the depth increases, while the posterior remains with a mode steadily close to zero. The probabilities of failure retrieved by these experiments are:

- $P(f_{prior}) = 0.00$, and $P(f_{posterior}) = 0.50$ between 0 and 1 m depth.
- $P(f_{prior}) = 0.00$, and $P(f_{posterior}) = 0.51$ between 1 and 2 m depth.
- $P(f_{prior}) = 0.01$, and $P(f_{posterior}) = 0.51$ between 2 and 3 m depth.
- $P(f_{prior}) = 0.02$, and $P(f_{posterior}) = 0.51$ between 3 and 4 m depth.
- $P(f_{prior}) = 0.05$, and $P(f_{posterior}) = 0.52$ between 4 and 5 m depth.

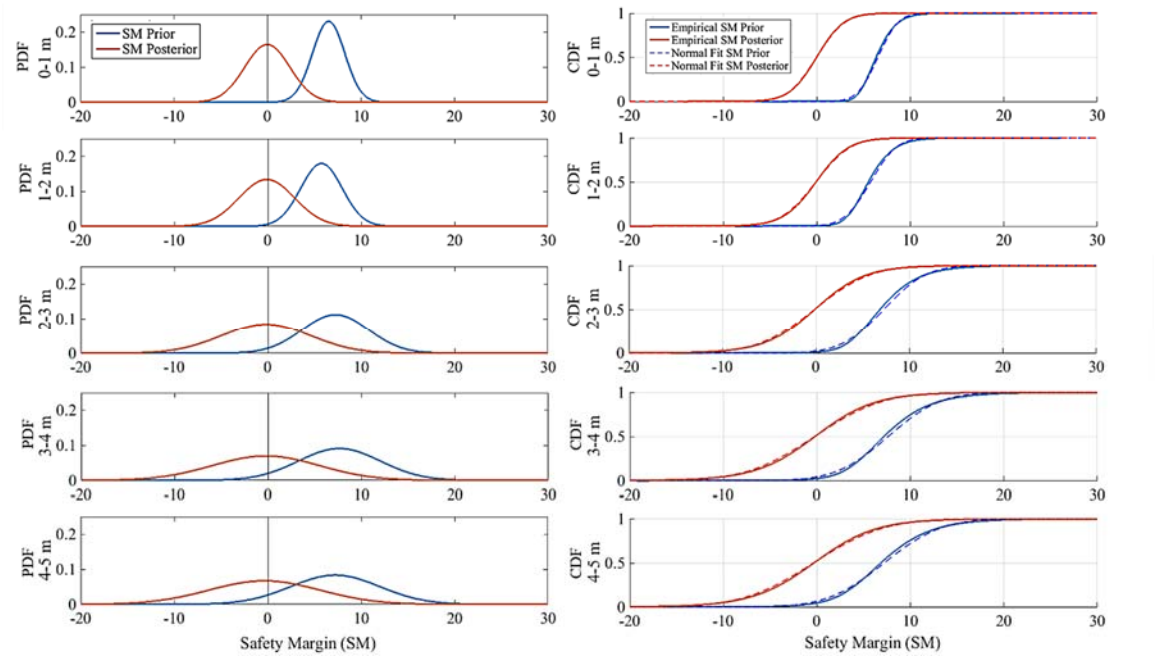

Fig. 5.45 PDF and CDF curves of SM for a FS as a RV for 5 populations of depth using 20 samples.

The results obtained by the forward Bayesian model calibration are shown in Table 5.14.

Table 5.14 States of evidence of Su for a FS as a RV for 5 populations of depth.

Depth (m)	State of Evidence	5 Points		20 Points	
		Mean	Standard Deviation	Mean	Standard Deviation
0-1	Observations of Su	6.81	1.69	6.81	1.69
	Forward model of prior Su	0.32	0.31	0.32	0.32
	Population prior Su	0.32	1.69	0.32	1.69
	Forward model of posterior Su	4.53	0.80	6.62	0.35
	Population posterior Su	4.53	1.69	6.62	1.69
	Prior SM	6.56	1.72	6.56	1.73
	Posterior SM	2.21	2.21	-0.01	2.42
1-2	Observations of Su	7.06	2.07	7.06	2.07
	Forward model of prior Su	1.38	0.62	1.38	0.62
	Population prior Su	1.38	2.07	1.38	2.07
	Forward model of posterior Su	4.71	0.89	6.86	0.42
	Population posterior Su	4.71	2.07	6.86	2.07
	Prior SM	5.76	2.22	5.76	2.22
	Posterior SM	2.24	2.70	-0.08	2.98
2-3	Observations of Su	9.46	3.30	9.46	3.30
	Forward model of prior Su	2.28	0.96	2.28	0.95
	Population prior Su	2.28	3.30	2.28	3.30
	Forward model of posterior Su	5.76	1.31	9.11	0.67
	Population posterior Su	5.76	3.30	9.11	3.30
	Prior SM	7.25	3.57	7.25	3.57
	Posterior SM	3.53	4.17	-0.16	4.77
3-4	Observations of Su	10.81	3.96	10.81	3.96
	Forward model of prior Su	3.21	1.29	3.21	1.28
	Population prior Su	3.21	3.96	3.21	3.96
	Forward model of posterior Su	10.20	1.35	10.38	0.79
	Population posterior Su	10.20	3.96	10.38	3.96
	Prior SM	7.65	4.40	7.65	4.41
	Posterior SM	0.03	5.80	-0.21	5.74
4-5	Observations of Su	11.27	4.10	11.27	4.10
	Forward model of prior Su	4.12	1.67	4.12	1.66
	Population prior Su	4.11	4.10	4.12	4.10
	Forward model of posterior Su	7.60	1.53	10.93	0.80
	Population posterior Su	7.60	4.10	10.93	4.10
	Prior SM	7.23	4.77	7.23	4.79
	Posterior SM	3.34	5.31	-0.33	5.96

The results of the inverse modelling of the studied physical parameters with a FS set as a random variable are illustrated in Fig. 5.46 to 5.51. In these figures it is observed that the domain of the updated parameters shift from higher to lower values, and gain certainty as the sediment height increases. The FS random variable is among the most sensitive variables to the model inversion, shifting from values strictly larger than 1.5 at the top interval of sediment to a likelihood of approximately 2.3% below 1. The quantitative estimators of these results are summarized in tables 5.15 and 5.16.

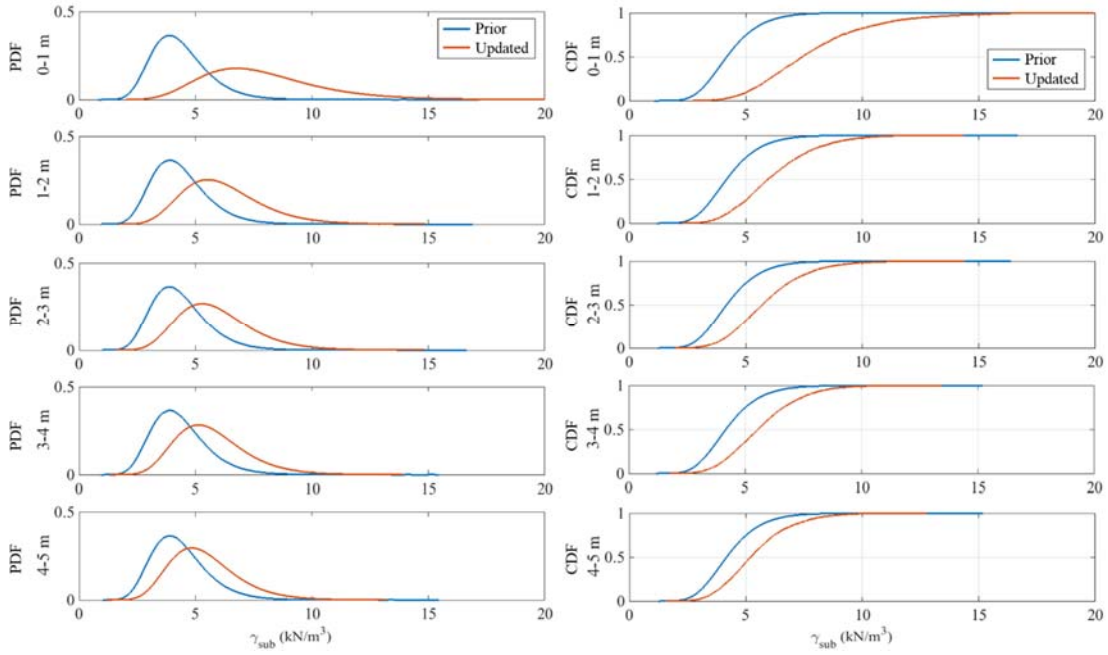

Fig. 5.46 PDF and CDF curves of γ_{sub} for a FS as a RV for 5 populations of depth using 20 samples.

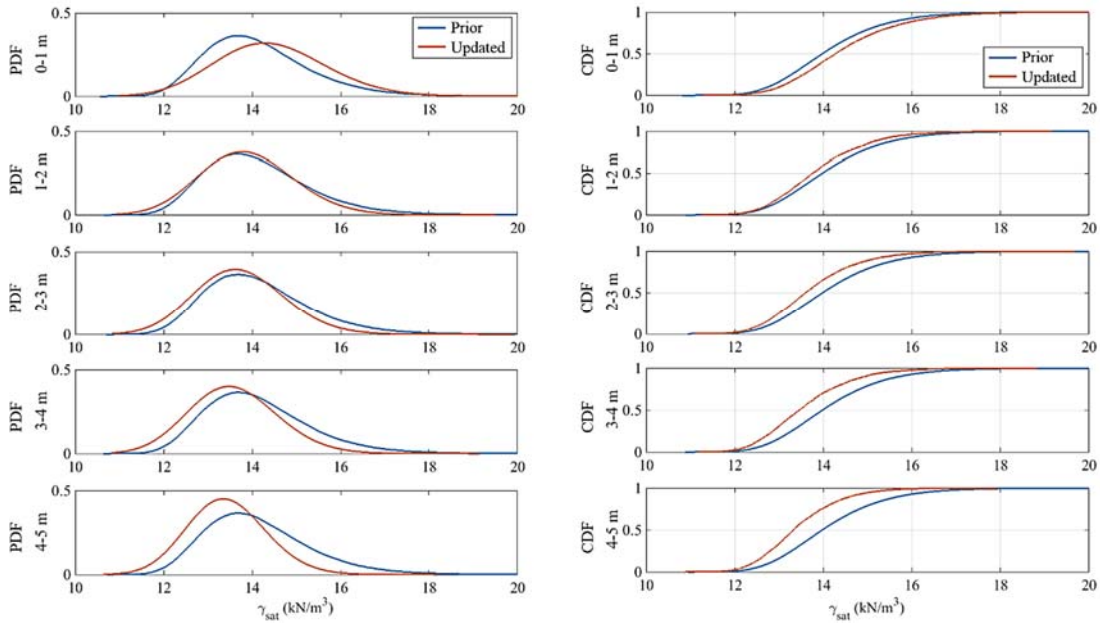

Fig. 5.47 PDF and CDF curves of γ_{sat} for a FS as a RV for 5 populations of depth using 20 samples.

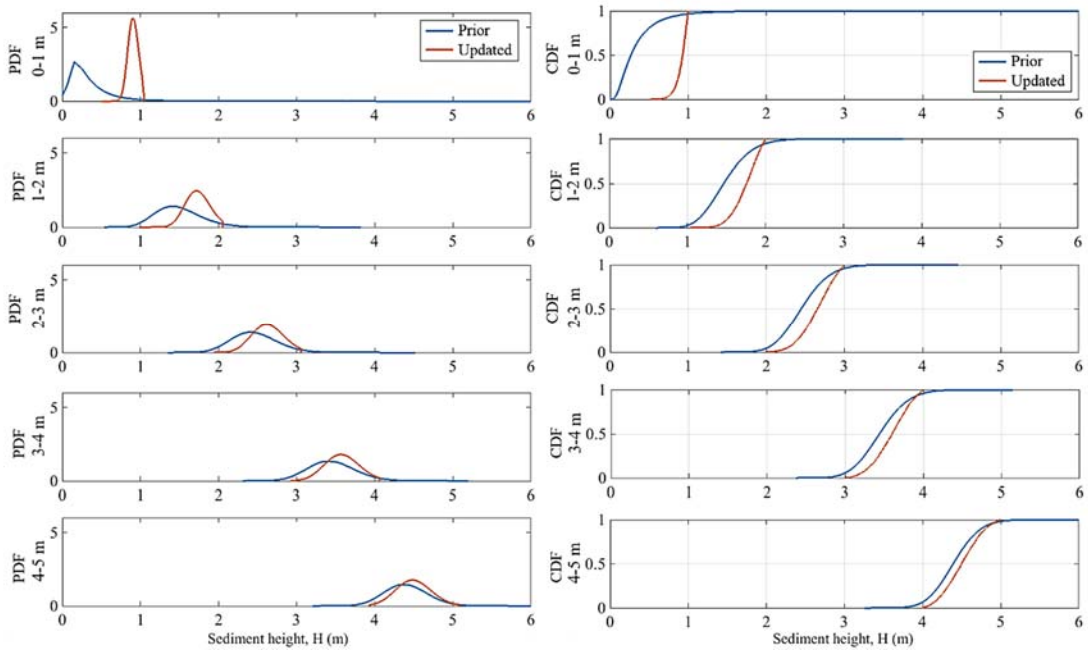

Fig. 5.48 PDF and CDF curves of H for a FS as a RV for 5 populations of depth using 20 samples.

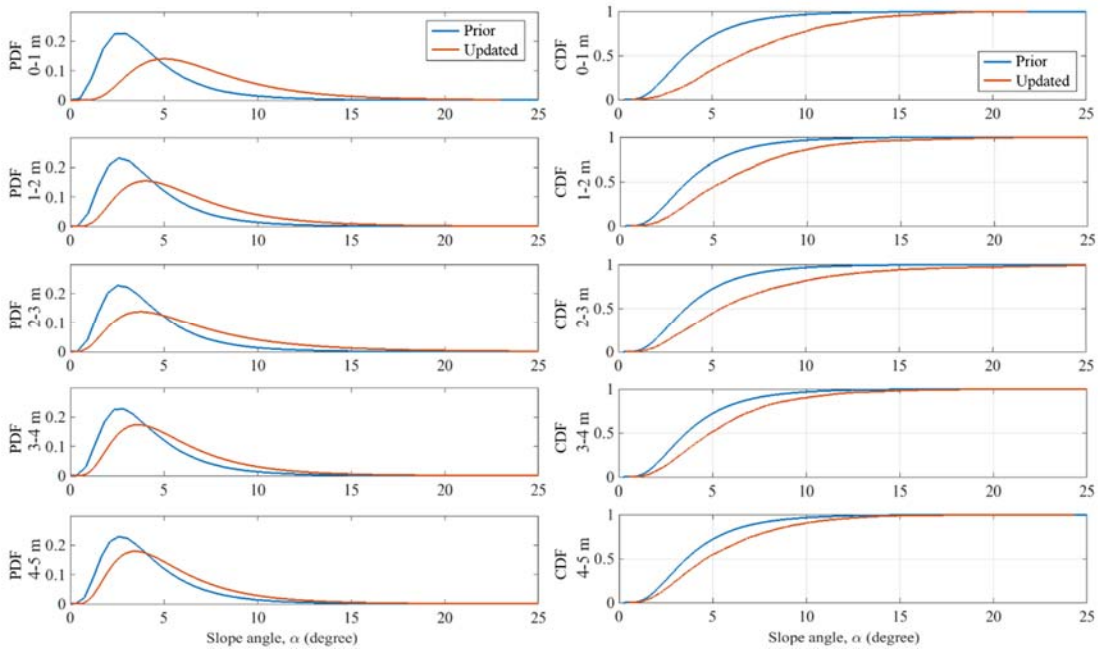

Fig. 5.49 PDF and CDF curves of α for a FS as a RV for 5 populations of depth using 20 samples.

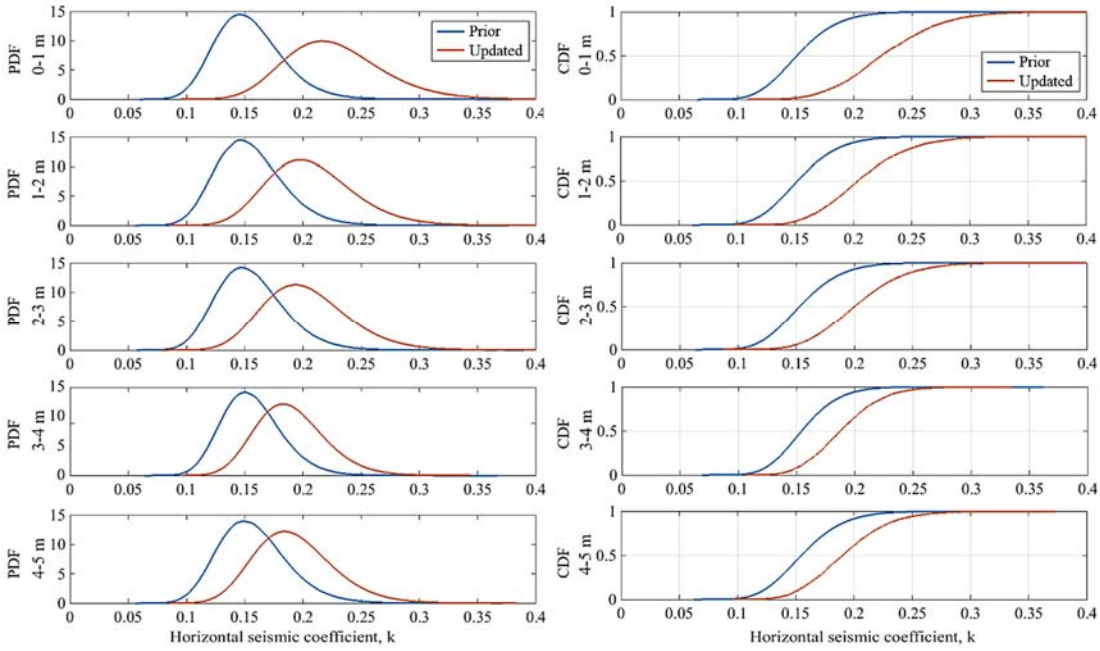

Fig. 5.50 PDF and CDF curves of k for a FS as a RV for 5 populations of depth using 20 samples.

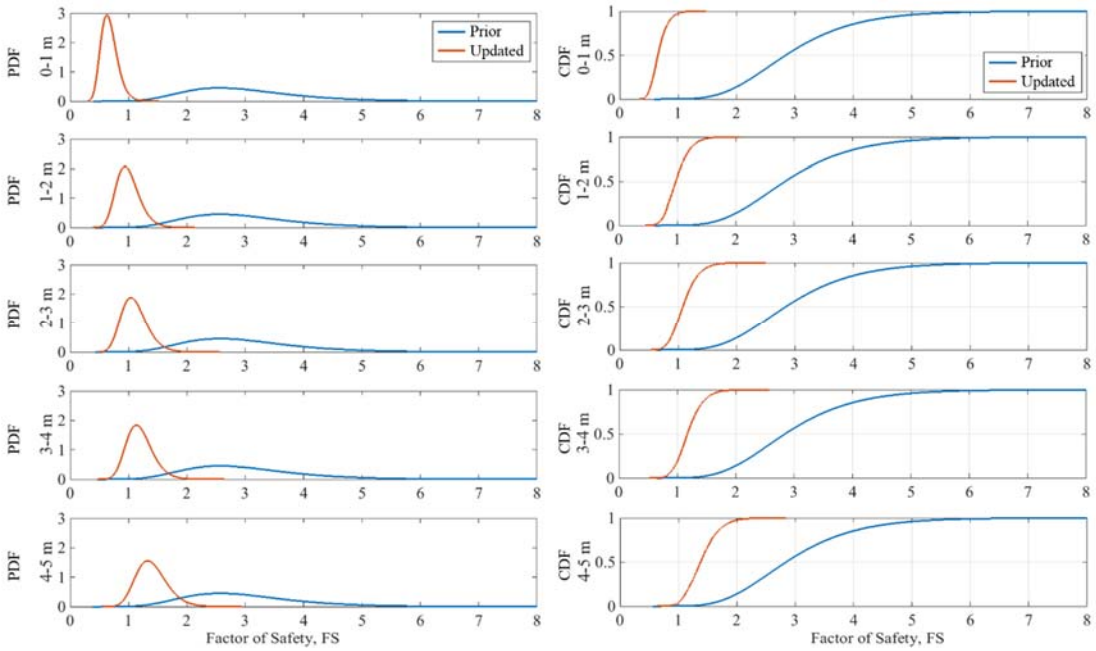

Fig. 5.51 PDF and CDF curves of FS for 5 populations of depth using 20 samples.

Table 5.15 States of evidence of $\gamma_{sub}, \gamma_{sat}$ and H for 20 samples using five populations and a FS as a RV.

Parameter	Depth (m)	Evidence	Mean	Standard Deviation
γ_{sub}	0-1	Prior	4.334	1.198
		Posterior	4.643	1.260
	1-2	Prior	4.333	1.198
		Posterior	4.095	1.068
	2-3	Prior	4.332	1.195
		Posterior	3.924	1.021
	3-4	Prior	4.333	1.198
		Posterior	3.781	1.004
	4-5	Prior	4.331	1.197
		Posterior	3.629	0.889
γ_{sat}	0-1	Prior	14.141	1.198
		Posterior	14.450	1.260
	1-2	Prior	14.140	1.198
		Posterior	13.902	1.068
	2-3	Prior	14.139	1.195
		Posterior	13.731	1.021
	3-4	Prior	14.140	1.198
		Posterior	13.588	1.004
	4-5	Prior	14.138	1.197
		Posterior	13.436	0.889
H	0-1	Prior	0.347	0.289
		Posterior	0.671	0.164
	1-2	Prior	1.494	0.295
		Posterior	1.400	0.208
	2-3	Prior	2.463	0.291
		Posterior	2.389	0.213
	3-4	Prior	3.451	0.299
		Posterior	3.380	0.220
	4-5	Prior	4.399	0.273
		Posterior	4.353	0.209

Table 5.16 States of evidence of α, k and FS for 20 samples using five populations and a FS as a RV.

Parameter	Depth (m)	Evidence	Mean	Standard Deviation
α	0-1	Prior	4.222	2.565
		Posterior	4.835	2.964
	1-2	Prior	4.224	2.560
		Posterior	4.034	2.535
	2-3	Prior	4.228	2.567
		Posterior	3.471	1.797
	3-4	Prior	4.225	2.560
		Posterior	3.520	1.918
	4-5	Prior	4.223	2.562
		Posterior	3.283	1.736
k	0-1	Prior	0.154	0.029
		Posterior	0.166	0.029
	1-2	Prior	0.155	0.029
		Posterior	0.145	0.024
	2-3	Prior	0.156	0.029
		Posterior	0.138	0.023
	3-4	Prior	0.156	0.026
		Posterior	0.138	0.021
	4-5	Prior	0.157	0.030
		Posterior	0.128	0.021
FS	0-1	Prior	3.000	1.002
		Posterior	4.008	1.140
	1-2	Prior	3.002	1.002
		Posterior	2.352	0.492
	2-3	Prior	3.001	1.000
		Posterior	1.981	0.372
	3-4	Prior	2.999	0.998
		Posterior	1.624	0.280
	4-5	Prior	3.000	0.999
		Posterior	1.449	0.259

Analysis

The use of lognormal distributions to model the behavior of the prior probability distributions of the physical parameters used in the slope stability analysis offered an acceptable description of their strictly positive domain, and of their lack of symmetry with respect to their mean value. However, the frequentist estimate of the modelled H presented the largest differences with respect to the lognormal probability distribution fit, providing an estimate with the largest amount of uncertainty. Since this parameter was assessed using the differential between the bathymetry and the nearest neighbor interpolation method, this approach is capturing the depth at which displacement most frequently occurs. However, the conception of the infinite slope model does not account for the sediment wedge's boundaries, and addresses an estimate of the depth of failure as a planar surface. The method of slices, which is a slightly more sophisticated commonly used approach to study landslides stability, takes under consideration the wedge ends of the sliding mass, and the slices where H tends to zero are the sections that contribute the least to the global failure mechanism. Considering these observations, the estimation of failure depths close to zero is the least likely scenario for a submarine landslide to occur when an infinite slope model is used. Hence, the use of the lognormal distribution to describe the prior behavior of this variable is considered an assertive approach to counteract the exponential trend of the observations.

The Bayesian model calibration conducted in this study is capable to accomplish two sets of results: (1) a forward model to estimate loading values of Su, SM and probability of failure, and (2) an inverse model yielding an updated state of the set of parameters θ

that fulfill a predefined condition of FS, and the observed values of the resistance. Comparing these calibrated results with the prior state of knowledge allows to draw conclusions about the strengths and limitations of each modeling approach. For instance, the capability of the Bayesian model calibration to reduce the uncertainty about the expected values of Su during the forward model (with 5 or 20 samples) consistently stands out compared with the prior's predictions. However, the calibrated results are strongly influenced by d_{obs} which means that it is simulating the expected value of the resisting forces. Additionally, since the population of both forward models (prior and posterior) are modelled using the standard deviation of d_{obs}, it is systematically observed that the modelled posterior population overlaps the observed Su population. Hence, the Bayesian forward model implemented in this study constantly predicts an expected value of the SM = 0 and a probability of failure close to 0.5. These results, although are not representative of the current state of the stability of the landslides, they are signaling that the calibration was achieved. The use of a FS at limit state or as a random variable has no effect on this observed behavior, since the posterior predictions are calibrated with respect to the same set of observations.

These results are accomplished by the tests conducted using 20 samples, and not with 5 samples. The posterior probability of failure using 5 samples returns an average of 0.3, and does not reach the anticipated value of 0.5 (e.g. see Fig. 5.22 and 5.30). Despite the fact that in some cases the level of uncertainty of d_{obs} for 5 samples is lower than for 20 samples (see table 5.10), the prediction of the expected value of the posterior forward model using 20 samples have lower standard deviations than the results obtained using 5

samples for all studied cases. These observations lead to the interpretation that 20 samples are the appropriate amount of physical observations of Su required to minimize the amount of uncertainty from the modelled results.

Assuming that the prior and posterior modelled populations of Su have the same standard deviation of the observations is not necessarily accurate. Yet, this approach is considered by the authors of this work as the most appropriate alternative given that those samples represent the only observed available evidence of the undrained shear strength. The SM predicted by the prior forward model is clearly adapting to the state of evidence provided by the changes of depth when 5 separate populations are tested. The prior forward model predicts higher probabilities of failure as depth increases, but at a cost of a significant rise of the uncertainty. These high levels of uncertainty are being influenced by the increased standard deviation of the d_{obs} at larger sediment heights. This trend is largely accentuated when a FS as a random variable is used. For these experiments, the confidence of the estimated SM is additionally attenuated by the contribution of the FS's uncertainty.

The results of the inverse problem are considered to be the most important contribution of the Bayesian model calibration approach proposed in this work. The updated set of parameters are interpreted as the physical conditions required to achieve the prescribed condition set upon the FS, given the observed evidence of Su. The results using one population (0 to 5 m of depth) and a FS at limit state show that the sediment height and the unit weight are most sensitive parameters to the calibration. The model predicts that the equilibrium state of the studied landslides is more likely to occur at 3.4 m of depth and

with slightly larger unit weights than suggested by the prior evidence. The prior distribution selected to model the FS returns a domain that is strictly larger than 1 ($\mu = 3, \sigma = 1$), which theoretically, guarantees that the resistance is larger than the loads. Therefore, when a FS as a random variable is used, the prediction of the updated H (1.3 m) is interpreted as the depth at which the FS is more likely to have a mean value of 3.

The results of the inverse model in the experiment using 5 populations allow to observe more significant changes on the prior and updated distributions of the studied parameters. Using a FS=1, the model is returning the conditions required by the parameters to reach the limit state at each depth range. At all depths, it is observed that all the updated parameters present higher values than the prior estimations, and this difference is reduced as the sediment height increases. For instance, the observed resistance between 0 and 1 m is 6.81 kPa, and the Su load predicted by the prior estimator is 0.86 kPa. In order to reach the equilibrium state at a depth between 0 and 1m, the updated $\gamma_{sub}, \gamma_{sat}, \alpha,$ and k should be higher than predicted by the prior, since they contribute to the loading forces required to match the resistance at such depth. According to the experiments using FS at limit state, it is interpreted that it is more likely that the load and the resistance reach equilibrium between 4 and 5 m of depth, given that the prior and updated estimates tend to overlap.

The use of FS as a random variable returns an updated distribution of the FS that increases with larger depth. It is observed that the overall behavior of the results obtained from the forward and inverse modelling using a FS as a random variable are noticeably more variable than the results obtained using the FS at limit state.

Conclusions

The Bayesian model calibration conducted on an infinite slope model to study submarine landslides consisted on the use of observed evidence of undrained shear strength to update the state of knowledge of the model's parameters. This slope stability model was selected as a simple approach to study the contributions of the Bayesian paradigm to improve the quality and the quantity of inferences derived from a limited amount of available data. Prior probability distributions of $\gamma_{sub}, \gamma_{sat}, \alpha, H,$ and k were used to predict the SM and the probability of failure of the slopes in the selected study area, while the SM retrieved by the posterior forward model was used to monitor that the results were calibrated. From the analysis of the number of samples required to achieve the best estimates, it is concluded that 5 samples are not enough evidence to complete the model calibration, which was achieved using 20 samples.

The updated estimations retrieved from the inverse model are considered to be a comprehensive assessment of the state of the parameters necessary to reach the prescribed conditions of FS given the available experimental observations of Su. The inferences derived from this type of analysis are heavily sensitive to the assumptions made about the FS. The experimental design utilized in this study sets the FS to be larger than or equal to one, which brings the necessity to highlight that the prior and posterior estimates are designed to respond under conservative circumstances. However, if the modeler selects any other value of FS, the forward and inverse prediction would respond accordingly. Therefore, the proposed methodology can be applied to test different desired scenarios to improve the estimations of the physical parameters to be used for the design of offshore

infrastructures. Nevertheless, if this work is replicated to minimize the uncertainty of the estimations, it is recommended to use a constant FS, or a random variable with a smaller standard deviation than the value used in these experiments.

The implementation of this methodology permitted to observe the sequential change of the parameters as the depth of the sediment increases. The use of the proposed model calibration methodology allowed to estimate the most likely depth at which the loading and the resistant forces are at equilibrium, which is an inference that the prior state of evidence was not able to capture. It was also found that as the updated estimations of the parameters θ reach the depth at which the prescribed condition of FS is reached, the uncertainty of the predictions decreases with respect to the prior estimations. All these remarks lead to conclude that the Bayesian model calibration can be successfully implemented to increase the quantity of inferences and the confidence on the estimations using limited amounts of evidence.

Future work to enhance the applicability of this method might include the modeling of individual landslides under different bathymetric conditions, along with the modeling of areas where no deformation is observed. This method could be used to map the updated estimations of the physical parameters and improve the decision-making process for pipeline routing or for the installation of any other type of infrastructure.

CHAPTER VI

CONCLUSIONS

Three different applications of the Bayesian paradigm were examined in this work, showing that the conditional probabilistic modeling is a versatile and valuable methodology to make predictions and to reduce the uncertainty. A simple conceptual Bayesian network within an environmental risk assessment framework was coupled with GIS to make predictions in a spatial domain. The set of random variables used in this model were designed to depict a state of hazard from a discrete number of threat intensity levels. The conditional probability of the consequences given the state of the hazard was considered as a vulnerability measurement. The join state of hazard and vulnerability allowed to assess a risk index defined as a symbolic quantification of the desirability of the consequences if a triggering event occurs. In chapter II, the spatial variability of the environmental risk upon aquifers, surface water bodies, ecoregions and land use/land cover was mapped across the Barnett Shale Play, given a potential accidental failure of the existent or projected oil and/or gas infrastructure.

The same principle was implemented in the study case described in chapter III, and it was used to predict the state of risk of slope failure in a selected area of the Oregon Coast Range. In this case, it was emphasized the capability of BNs to integrate disparate model predictions in a joint state of evidence used to retrieve an inclusive assessment of the risk upon the existent infrastructure in the study area. The *BN+GIS* methodology illustrated through these applications proved to be a practical approach for spatial data synthesis, and

demonstrated to provide substantial contributions to improve the decision-making process. Moreover, as the availability of GIS and remote sensing datasets become more frequent, accurate, and precise, it is expected that the inferences derived from the use of the BN+GIS tool become more significant and reliable.

The implementation of the forward model as described above, allowed to evaluate the prior state of threat intensity evidence to retrieve a posteriori assessment of the risk in a prognostic type of reasoning. This type of modeling can be applied during the early stages of a project development to design the necessary counter-measurements and reduce the vulnerability given the predicted potential consequences. Furthermore, the *BN+GIS* capability to perform an inverse type of modelling or diagnosis, allowed to study a mechanism that can be used for policy-making. The selection of a specific value of risk permitted to update the current state of evidence to a conjectural scenario that would be conditioned to a desired outcome. More specifically, the diagnostic tool described in this work allowed to map the threat intensity conditions required to achieve a prescribed value of risk. A potential application of this tool consists on identifying the most suitable areas to install monitoring stations to keep track of the potential hazards, and/or to design maintenance campaigns to reduce the vulnerability in the most sensitive regions.

The parametrical sensitivity analysis conducted in chapter III examined the effect of the spatial sampling methodology on the resulting maps. It was concluded that the optimum sample size and interval is strongly dependent of the joint state of evidence displayed by the prognostic risk maps. Results with a fine resolution required to sample at small intervals, and returned a slightly broader range of risk values, but at the cost of larger

computational times. It was also concluded that the selection of an appropriate sample frequency and buffer radius can be reasonably estimated through the computation of the spatial autocorrelation structure of the risk maps. The diagnostic message propagated to the top of the model to update the state of the hazard resulted to have less impact on spatially clustered variables than on those displaying a spatially disperse behavior.

The implementation of the Bayesian paradigm as part of a random process for continuous variables illustrated another application of conditional probabilities to improve the decision making process. Chapter V explored the use of forward and inverse modeling of failure mechanisms on submarine landslides using bathymetric and CPT data to calibrate the model predictions with the observations. It was concluded that the proposed methodology provide valuable information about the number of samples required to reduce the uncertainty about the estimated parameters, which can be used to plan further surveying efforts and the amount of resources necessary to acquire further data. The use of a fixed or variable factor of safety permitted to identify the most likely height of sediment at which failure occurs and the physical parameters of the sediments at such depth. These results included not only the expected value of such parameters, but also a quantification of their associated uncertainty that can also maximize the amount of inferences derived from the Bayesian model calibration process.

REFERENCES

AASHTO (American Association of State Highway and Transportation Officials). (1998) Bridge design specifications. L.R.F.D. Washington, DC.

Aguilera, P.A., Fernández, R., Rumí, R., and Salmerón, A. (2011). "Bayesian networks in environmental modeling." *Environmental Modelling & Software,* 26, 1376-1388.

Aitkenhead, M. J., and Aalders, I. H. (2009). "Predicting land cover using GIS, Bayesian and evolutionary algorithm methods." *Journal of environmental management*, 90(1), 236-250.

American Society for Testing and Materials (ASTM). (1999) "Standard Test Method for Unconsolidated-Undrained Triaxial Compression Test on Cohesive Soils" D2850 − 15, West Conshohocken, Pa.

American Society for Testing and Materials (ASTM). (2000) "Standard Test Method for Laboratory Miniature Vane Shear Test for Saturated Fine-Grained Clayey Soil" D4648/D4648M − 16, West Conshohocken, Pa.

American Society for Testing and Materials (ASTM). (2000) "Standard Test Methods for Liquid Limit, Plastic Limit, and Plasticity Index of Soils" D4318 − 17, West Conshohocken, Pa.

American Society for Testing and Materials (ASTM). (2009) "Standard Test Methods for Laboratory Determination of Density (Unit Weight) of Soil Specimens" D7263 − 09, West Conshohocken, Pa.

Bacon, P. J., Cain, J. D., and Howard, D. C. (2002). "Belief network models of land manager decisions and land use change." *Journal of Environmental Management*, 65(1), 1-23.

Beven, K. J., and Kirkby, M. J. (1979). "A physically based, variable contributing area model of basin hydrology." *Hydrological Sciences Journal*, 24(1), 43-69.

Bishop, A. W. (1955). "The use of the slip circle in the stability analysis of slopes." *Geotechnique*, 5:7-17.

Biswajeet, P., and Saro, L. (2007). "Utilization of optical remote sensing data and GIS tools for regional landslide hazard analysis using an artificial neural network model." *Earth Science Frontiers*, 14(6), 143-151.

Briaud, J. L. (2013). "Geotechnical engineering: unsaturated and saturated soils." John Wiley & Sons.

Brittingham, M. C., Maloney, K. O., Farag, A. M., Harper, D. D., and Bowen, Z. H. (2014). "Ecological risks of shale oil and gas development to wildlife, aquatic resources and their habitats." *Environmental Science & Technology*, 48(19), 11034-11047.

Brown, Michael Kenneth. (2012). "Landslide detection and susceptibility mapping using LiDAR and artificial neural network modeling: a case study in glacially dominated Cuyahoga River valley, Ohio." Doctoral dissertation. Bowling Green State University, OH.

Brunn, A., and Weidner, Uwe (1997) "Extracting buildings from digital surface models" *International Archives of Photogrammetry and Remote Sensing*, 32, 3-4W2, 27-34.

Bui, D., Pradhan, B., Lofman, O., Revhaug, I., and Dick, O. B. (2012). "Landslide susceptibility assessment in the Hoa Binh province of Vietnam: a comparison of the Levenberg–Marquardt and Bayesian regularized neural networks." *Geomorphology*, 171, 12-29.

Burns, W. J., and Madin, I. (2009). "Protocol for inventory mapping of landslide deposits from light detection and ranging (LiDAR) imagery." *Oregon Department of Geology and Mineral Industries*.

Burns, W. J., Mickelson, K. A., and Madin, I. (2016). "Landslide Susceptibility Overview Map of Oregon." *Oregon Department of Geology and Mineral Industries*.

Cepeda, J., Chávez, J. A., and Martínez, C. C. (2010). "Procedure for the selection of runout model parameters from landslide back-analyses: application to the Metropolitan Area of San Salvador, El Salvador." *Landslides*, 7(2), 105-116.

Cerovski-Darriau, C. R. (2016). "Landslides and Landscape Evolution over Decades to Millennia: Using Tephrochronology, Air Photos, Lidar, and Geophysical Investigations to Reconstruct Past Landscapes." Doctoral dissertation, University Of Oregon, OR.

Chen, S., and Pollino, C. (2012). "Good practice in Bayesian network modeling." *Environmental Modelling & Software*, 37, 134-145.

City Council of Coppell (2013). "Article 9-26 oil and gas drilling," *Ordinance Number 2013-1332,* [Author] Coppell, TX.

Coupé, V. M., and Van Der Gaag, L. C. (2002). "Properties of sensitivity analysis of Bayesian belief networks." *Annals of Mathematics and Artificial Intelligence*, 36(4), 323-356.

Danciu, L., and Giardini, D. (2015). Global Seismic Hazard Assessment Program-GSHAP legacy. Annals of Geophysics, 58(1).

Das, R. (2016). Probabilistic Slope Stability Assessment of Submarine and Slides by the Use of Bayesian Inference. Master's thesis, Texas A&M University.

Dincer, I. (1999). "Environmental impacts of energy." *Energy Policy*, 27(14), 845-854.

DrillingInfo. (2015). "Barnett shale Production wells." <http://info.drillinginfo.com/> (February, 2015).

Duncan, J. M. (1992). "Soil strengths from back-analysis of slope failures." *In Proc. of Specialty Conf. Stability and Performance of Slopes and Embankments-II* (Vol. 1, pp. 890-904). ASCE.

EIA (U. S. Energy Information Administration). (2011). *Lower 48 states shale plays*, [Author], Washington, DC.

ESRI (Environmental Systems Research Institute). (2012). ArcGIS Desktop 10.1. Redlands, CA.

Ercanoglu, M., and Gokceoglu, C. (2002). "Assessment of landslide susceptibility for a landslide-prone area (north of Yenice, NW Turkey) by fuzzy approach." *Environmental Geology*, 41(6), 720-730.

Ethridge, S., Bredfeldt, T., Sheedy, K., Shirley, S., Lopez, G., and Honeycutt, M. (2015). "The Barnett Shale: From problem formulation to risk management." *Journal of Unconventional Oil and Gas Resources*, 11, 95-110.

Faber, M. H., and Stewart, M. G. (2003). "Risk assessment for civil engineering facilities: critical overview and discussion." *Reliability engineering and system safety*, 80(2), 173-184.

Flower Mound Town Council. (2011). "Oil and natural gas well drilling and operations," *Ordinance No 29-11,* [Author], Flower Mound, TX.

Forth Worth City Council. (2009). *Ordinance N° 18449-02-200*, [Author], Forth Worth, Texas

Franchini, M., Hashemi, A. M., and O'Connell, P. E. (2000). "Climatic and basin factors affecting the flood frequency curve: PART II? A full sensitivity analysis based on the continuous simulation approach combined with a factorial experimental design." *Hydrology and Earth System Sciences Discussions*, 4(3), 483-498.

Gardoni, P., and LaFave, J. M (Eds.). (2016). *Multi-hazard approaches to civil infrastructure engineering*, Springer, Switzerland.

Gilbert, R. B., Wright, S. G., and Liedtke, E. (1998). "Uncertainty in back analysis of slopes: Kettleman Hills case history." *Journal of Geotechnical and Geoenvironmental Engineering*, 124(12), 1167-1176.

Gorsevski, P. V., Gessler, P. E., Foltz, R. B., and Elliot, W. J. (2006). "Spatial prediction of landslide hazard using logistic regression and ROC analysis." *Transactions in GIS*, 10(3), 395-415.

Griffiths, D. V., and Fenton, G. A. (2001). "Bearing capacity of spatially random soil: the undrained clay Prandtl problem revisited." *Geotechnique*, 51(4), 351-360.

Grêt-Regamey, A., and Straub, D. (2006). "Spatially explicit avalanche risk assessment linking Bayesian Networks to a GIS." *Natural Hazards and Earth System Science*, 6, 911-926.

Growe, S., Schröder, T., and Liedtke, C. E. (2000). "Use of Bayesian networks as judgement calculus in a knowledge based image interpretation system." *International Archives of Photogrammetry and Remote Sensing*, 33(B3/1; PART 3), 342-350.

GWP (Global Water Partnership). (2014). "The links between land use and groundwater." <http://www.gwp.org/Global/ToolBox/Publications/Perspective%20Papers/perspective_paper_landuse_and_groundwater_no6_english.pdf> (January, 2017).

Hamby, D. M. (1994). "A review of techniques for parameter sensitivity analysis of environmental models." *Environmental monitoring and assessment*, 32(2), 135-154.

Haneberg, W. C. (2012). "Spatially Distributed Probabilistic Assessment of Submarine Slope Stability." *In Offshore Site Investigation and Geotechnics: Integrated Technologies-Present and Future.* Society of Underwater Technology.

HARC (Houston Advanced Research Center). (2010). *Environmental friendly drilling systems scorecard reference guide,* Ver. 1.0, The Woodlands, TX.

Hashemi, A. M., Franchini, M., and O'Connell, P. E. (2000). "Climatic and basin factors affecting the flood frequency curve: PART I? A simple sensitivity analysis based on the continuous simulation approach." *Hydrology and Earth System Sciences Discussions*, 4(3), 463-482.

Haining, R. (1991). “Bivariate correlation with spatial data.” *Geographical Analysis*, 23(3), 210-227.

Hauke, J., and Kossowski, T. (2011). Comparison of values of Pearson's and Spearman's correlation coefficients on the same sets of data. Quaestiones geographicae, 30(2), 87.

Helton, J. C., Johnson, J. D., Sallaberry, C. J., and Storlie, C. B. (2006). “Survey of sampling-based methods for uncertainty and sensitivity analysis.” *Reliability Engineering & System Safety*, 91(10), 1175-1209.

Hoff, P. D. (2009). *A first course in Bayesian statistical methods*. Springer Science & Business Media.

Huang, J., and Yuan, Y. (2007). “Construction and application of Bayesian network model for spatial data mining.” *Proc., 2007 IEEE International Conference on Control and Automation*, Vol 18.6, IET, Stevenage, UK 2802-2805.

Huang, J., Qi, P., Wan, Y., and Ye, F. (2008). “A novel approach to spatial data fusion based on Bayesian network.” *Proc., Int. Conf. on Earth Observation Data Processing and Analysis*, Vol. 7285, International Society for Optical Engineering. Bellingham, WA.

IADC (International Association of Drilling Contractors). (2009). “Health, Safety and Environment Case Guidelines for Land Drilling Contractors.” Issue 1.0.1. Houston, Texas.

ISO (International Organization for Standardization). (2009) “Risk management – Principles and guidelines.” *ISO 31000:2009*, Geneva, Switzerland.

Jaboyedoff, M., Oppikofer, T., Abellán, A., Derron, M. H., Loye, A., Metzger, R., and Pedrazzini, A. (2012). “Use of LIDAR in landslide investigations: a review.” *Natural Hazards*, 61(1), 5-28.

Jenkins, J., Turner, B., Turner, R., Hayes, G. V., Sinclair, A., Davies, S., and Benz, H. M. (2010). “Seismicity of the Earth 1900–2010 Middle East and Vicinity” (ver. 1.1, Jan. 28, 2014). US Geological Survey Open File Report.

Jensen, J. R., Halls, J. N., and Michel, J. (1998). “A systems approach to Environmental Sensitivity Index (ESI) mapping for oil spill contingency planning and response.” *Photogrammetric Engineering and Remote Sensing*, 64, 1003-1014.

Jiang, S. H., Li, D. Q., Zhang, L. M., and Zhou, C. B. (2014). “Slope reliability analysis considering spatially variable shear strength parameters using a non-intrusive stochastic finite element method.” *Engineering Geology*, 168, 120-128.

Johnson, S., Low-Choy, S., and Mengersen, K. (2012). "Integrating Bayesian networks and geographic information systems: Good practice examples." *Integrated Environmental Assessment and Management,* 8(3), 473-479.

Jones, J. (2006). “An introduction to factor analysis of information risk (FAIR).” *Norwich Journal of Information Assurance*, 2(1), 67.

Kiiveri, H., and Caccetta, H. (1998). "Image fusion with conditional probability networks for monitoring the salinization of farmland." *Digital Signal Processing*, 8(4), 225-230.

Kocabas, V., and Dragicevic, S. (2007). "Enhancing a GIS cellular automata model of land use change: Bayesian networks, influence diagrams and causality." *Transaction in GIS*, 11(5), 681-702.

Korb, K., and Nicholson, A. (2004). *Bayesian artificial intelligence*, Chapman & Hall, London, England.

Lan, D., Liang, B., Bao, C., Ma, M., Xu, Y., and Yu, C. (2015). "Marine oil spill risk mapping for accidental pollution and its application in a coastal city." *Marine Pollution Bulletin*, 96(1), 220-225.

Laskey, K. B. (1995). Sensitivity analysis for probability assessments in Bayesian networks. IEEE *Transactions on Systems, Man, and Cybernetics*, 25(6), 901-909.

Lee, S., and Min, K. (2001). "Statistical analysis of landslide susceptibility at Yongin, Korea." *Environmental Geology*, 40(9), 1095-1113.

Lee, S. (2007). "Landslide susceptibility mapping using an artificial neural network in the Gangneung area, Korea." *International Journal of Remote Sensing*, 28(21), 4763-4783.

Li, L., Wang, J., Leung, H., and Jiang, C. (2010). "Assessment of catastrophic risk using Bayesian network constructed from domain knowledge and spatial data." *Risk Analysis*, 30(7), 1157-1175.

Liu, Z., Nadim, F., Garcia-Aristizabal, A., Mignan, A., Fleming, K., and Luna, B. Q. (2015). "A three-level framework for multi-risk assessment." *Georisk: Assessment and Management of Risk for Engineered Systems and Geohazards*, 9(2), 59-74.

Mahalingam, R., Olsen, M. J., and O'Banion, M. S. (2016). “Evaluation of landslide susceptibility mapping techniques using lidar-derived conditioning factors (Oregon case study).” *Geomatics, Natural Hazards and Risk*, 1-24.

Marcot, B., Steventon, D., Sutherland, G., and McCann, R. (2006). "Guidelines for developing and updating Bayesian belief networks applied to ecological modeling and conservation." *Canadian Journal of Forest Research*, 36(12), 3063-3074.

Mariano, J. B., and La Rovere, E. L. (2007). “Environmental impacts of the oil industry.” *Petroleum engineering-Downstream, Encyclopedia of Life Support Systems (EOLSS).* Sample-Chapters C, 8. <http://www. eolss. net> (January, 2017).

Masson, D. G., Harbitz, C. B., Wynn, R. B., Pedersen, G., and Løvholt, F. (2006). “Submarine landslides: processes, triggers and hazard prediction.” *Philosophical Transactions of the Royal Society of London A: Mathematical, Physical and Engineering Sciences*, 364(1845), 2009-2039.

Matthies, H. (2007). “Quantifying uncertainty: modern computational representation of probability and applications.” *Extreme man-made and natural hazards in dynamics of structures*, 105-135.

McCloskey, J., Lilieholm, R., and Cronan, C. (2011). “Using Bayesian belief networks to identify potential compatibilities and conflicts between development and landscape conservation.” *Landscape and Urban Planning*, 101(2), 190-203.

Medina-Cetina, Z., and Nadim, F. (2008). “Stochastic design of an early warning system.” *Georisk*, 2(4), 223-236.

Medina-Cetina, Z., and Varela, P. (2012). "System engineering design methodology-low impact well design optimization,*" RPSEA EFD Project 08122-35*, Houston Advanced Research Center, The Woodlands, TX.

Medina-Cetina, Z., Varela, P., and Eriksson, M. (2017). "Coupling Bayesian Networks and GIS for Prognosis and Diagnosis Environmental Risk Assessment". *ASCE-Journal of Risk and Uncertainty in Engineering Systems, Part A: Civil Engineering.* (In preparation).

Miles, D. W. R., and Swanson, F. J. (1986). "Vegetation composition on recent landslides in the Cascade Mountains of western Oregon." *Canadian Journal of Forest Research*, 16(4), 739-744.

Mitchell, A. (1999). The ESRI guide to GIS analysis: geographic patterns & relationships (Vol. 1). ESRI, Inc.

Montgomery, S., Jarvie, D., Bowker, K., and Pollastro, M. (2005). "Mississippian Barnett Shale, Fort Worth basin, north-central Texas: Gas-shale play with multi-trillion cubic feet potential." *AAPG Bulletin*, 89 (2), 155-175.

NRCS-USDA (Natural Resources Conservation Service - US Department of Agriculture,). (2007). Land use/Land cover map. <http://www.webgis.com/dlgdata.html> (July, 2012).

ODOT (Oregon Department of Transportation). (2015) *Geotechnical Design Manual*, Geo-Environmental Section, Salem, OR.

Oreskes, N., Shrader-Frechette, K., and Belitz, K. (1994). "Verification, validation, and conformation of numerical models in the earth sciences." *Science,* 263 (5147), 641-646.

OWRB (Oklahoma Water Resources Board). (2006a). OWRB major aquifers of Oklahoma, <http://www.owrb.ok.gov/maps/PMG/owrbdata_GW.html> (July, 2012).

OWRB (Oklahoma Water Resources Board). (2006b). OWRB minor aquifers of Oklahoma, <http://www.owrb.ok.gov/maps/PMG/owrbdata_GW.html> (July, 2012).

Pistocchi, A., Luzi, L., and Napolitano, P. (2002). "The use of predictive modeling techniques for optimal exploitation of spatial databases: a case study in landslide hazard mapping with expert system-like methods." *Environmental Geology*, 41(7), 765-775.

Pollastro, R., Jarvie, D., Hill, R., and Adams, C. (2007). "Geologic framework of the Mississippian Barnett Shale, Barnett-Paleozoic total petroleum system, Bend Arch Fort Worth Basin, Texas." *AAPG Bulletin,* 91(4), 405-436.

Pourghasemi, H. R., Moradi, H. R., and Aghda, S. F. (2013). "Landslide susceptibility mapping by binary logistic regression, analytical hierarchy process, and statistical index models and assessment of their performances." *Natural Hazards*, 69(1), 749-779.

Pradhan, B. (2010a). "Remote sensing and GIS-based landslide hazard analysis and cross-validation using multivariate logistic regression model on three test areas in Malaysia." *Advances in space research*, 45(10), 1244-1256.

Pradhan, B. (2010b). "Application of an advanced fuzzy logic model for landslide susceptibility analysis." *International Journal of Computational Intelligence Systems*, 3(3), 370-381.

Purdy, G. (2010). "ISO 31000: 2009—Setting a new standard for risk management." *Risk Analysis*, 30(6), 881-886.

Quirós, G. W., Little, R. L., & Garmon, S. (2000). "A normalized soil parameter procedure for evaluating in-situ undrained shear strength." *In Offshore Technology Conference*. Offshore Technology Conference.

Rahman, M. S. (1994). "Instability and movements of oceanfloor sediments: A review." *In The Fourth International Offshore and Polar Engineering Conference*. International Society of Offshore and Polar Engineers.

Ranalli, M., Medina-Cetina, Z., Gottardi, G., and Nadim, F. (2013). "Probabilistic calibration of a dynamic model for predicting rainfall-controlled landslides." *Journal of Geotechnical and Geoenvironmental Engineering*, 140(4), 04013039.

Rémai, Z. (2013). "Correlation of undrained shear strength and CPT resistance." *Periodica Polytechnica*. Civil Engineering, 57(1), 39.

Robert, C. (2007). *The Bayesian choice: from decision-theoretic foundations to computational implementation*. Springer Science & Business Media.

RRC (Railroad Commission of Texas). (2014). "Barnett Shale information." <http://www.rrc.state.tx.us/oil-gas/major-oil-gas-formations/barnett-shale-information/> (June, 2012).

Reid, S. (2000). “Acceptable risk criteria.” *Progress in Structural Engineering and Materials*, 2(2), 254-262.

Reuters, T. (2010). “Web of knowledge.” <http://wokinfo.com/training_support/training/web-of-knowledge/> (2010).

Rickli, C., Zimmerli, P., and Böll, A. (2001). “Effects of vegetation on shallow landslides: an analysis of the events of August 1997 in Sachseln, Switzerland.” *In International Conference on Landslides, Causes, Impacts and Countermeasures*, Essen (pp. 575-584).

Saltelli, A., Tarantola, S., and Chan, K. S. (1999). “A quantitative model-independent method for global sensitivity analysis of model output.” *Technometrics*, 41(1), 39-56.

Shooman, M. L. (1968). *Probabilistic reliability: an engineering approach*.

Smith, C., Howes, A., Price, B., and McAlpine, C. (2007). "Using a Bayesian belief network to predict suitable habitat of an endangered mammal–The Julia Creek dunnart (Sminthopsis douglasi)." *Biological Conservation*, 139(3), 333-347.

Smith, J. B., Godt, J. W., Baum, R. L., Coe, J. A., Burns, W. J., Morse, M. M., ... and Kaya, M. (2014). “Hydrologic monitoring of a landslide-prone hillslope in the Elliott State Forest, Southern Coast Range, Oregon, 2009-2012.” (No. 2013-1283). *US Geological Survey*.

Sobol, I. M. (1993). “Sensitivity estimates for nonlinear mathematical models.” *Mathematical Modelling and Computational Experiments*, 1(4), 407-414.

Sohl, T., and Sayler, K. (2008). “Using the FORE-SCE model to project land-cover change in the southeastern United States.” *Ecological Modelling*, 219(1), 49-65.

Spencer, E. (1967). “A method of analysis of the stability of embankments assuming parallel inter-slice forces.” *Geotechnique*, 17(1), 11-26.

Song, Y., Gong, J., Gao, S., Wang, D., Cui, T., Li, Y., and Wei, B. (2012). “Susceptibility assessment of earthquake-induced landslides using Bayesian network: a case study in Beichuan, China.” *Computers & Geosciences*, 42, 189-199.

Spiegelhalter, D. J., and Lauritzen, S. L. (1990). Sequential updating of conditional probabilities on directed graphical structures. Networks, 20(5), 579-605.

Stassopoulou, A., Petrou, M., and Kittler, J. (1998). “Application of a Bayesian network in a GIS based decision making system.” *International Journal of Geographical Information Science*, 12(1) 23-45.

Stelzenmüller, V., Lee, V., Garnacho, E., and Rogers, S. (2010). "Assessment of a Bayesian Belief Network–GIS framework as a practical tool to support marine planning." *Marine Pollution Bulletin*, 60(10), 1743-1754.

Terzaghi, K., and Peck, R. B. (1967). *Soil Mechanics in Engineering Practice*. John Wiley & Sons.

Tobler, W. R. (1970). “A computer movie simulating urban growth in the Detroit region.” *Economic Geography*, 46(sup1), 234-240.

Tong, S. T., and Chen, W. (2002). “Modeling the relationship between land use and surface water quality.” *Journal of Environmental Management*, 66(4), 377-393.

TWBD (Texas Water Development Board). (2006a). Major aquifers geodatabase. <https://www.twdb.texas.gov/groundwater/aquifer/> (June, 2012).

TWBD (Texas Water Development Board). (2006b). Minor aquifers geodatabase. <https://www.twdb.texas.gov/groundwater/aquifer/> (June, 2012).

UNDRO (United Nations Disaster Relief Organization). (1979). "Natural disasters and vulnerability analysis." <http://www.preventionweb.net/files/resolutions/NL800388.pdf> (July, 2012).

US Census Bureau. (2013). "TIGER Roads By County Merge" <http://www.census.gov/geo/maps-data/data/tiger-line.html> (Aug. 20, 2016).

USDA (United States Department of Agriculture). (2013). "Web Soil Survey." <http://websoilsurvey.sc.egov.usda.gov/App/WebSoilSurvey.aspx>(Aug. 20, 2016).

US EPA (US Environmental Protection Agency). (2011). "US level IV ecoregions of the continental United States." <https://www.epa.gov/eco-research/level-iii-and-iv-ecoregions-continental-united-states> (July, 2012)

USGS (US Geological Survey). (2010). "Feature directory for NHD datasets." <http://nhd.usgs.gov/data.html> (July, 2012).

USGS Geologic Hazards Science Center. (2016). Worldwide Seismic Design Tool (Beta). Retrieves from http://geohazards.usgs.gov/designmaps/ww/

Varela, P. (2013) "Bayesian networks and geographical information systems for environmental risk assessment for oil and gas site development." MS Thesis, Texas A&M University. College Station, TX.

Vidic, R. D., Brantley, S. L., Vandenbossche, J. M., Yoxtheimer, D., and Abad, J. D. (2013). "Impact of shale gas development on regional water quality." *Science*, 340(6134).

Völker, D. J. (2010). "A simple and efficient GIS tool for volume calculations of submarine landslides." *Geo-Marine Letters*, 30(5), 541-547.

Walker, A. R., Pham, B., and Moody, M. (2005). "Spatial Bayesian learning algorithms for geographic information retrieval." *Proceedings of the 13th Annual ACM International. Workshop on Geographic Information Systems,* ACM, New York, NY, 105-114.

Wang, J. F., Stein, A., Gao, B. B., and Ge, Y. (2012). "A review of spatial sampling." *Spatial Statistics*, 2, 1-14.

Wang, J. P., and Huang, D. (2013). "Slope Failure Probability Under Earthquake Condition by Monte Carlo Simulation: Methodology and Example for an Infinite Slope." *In Proceedings of the International Symposium on Engineering under Uncertainty: Safety Assessment and Management* (ISEUSAM-2012) (pp. 643-652). Springer, India.

Weber, P., Medina-Oliva, G., Simon, C., and Iung, B. (2012). "Overview on Bayesian networks applications for dependability, risk analysis and maintenance areas." *Engineering Applications of Artificial Intelligence*, 25(4), 671-682.

Westfall, S. (2016). "Exploration Impact Assessment Toolkit: Maximising Efficiency Through Standardisation To Deliver Robust Impact Assessments." Proc., *SPE*

International Conference and Exhibition on Health, Safety, Security, Environment, and Social Responsibility. Society of Petroleum Engineers, Richardson, TX.

Wright, N. H. (2014). "Dealing With Cumulative Environmental Risk in Unlocking Access to Constrained Resources in Frontier Areas and Unconventional Resources." Proc., *SPE International Conference on Health, Safety, and Environment*. Society of Petroleum Engineers, Richardson, TX.

Xie, M., Esaki, T., and Zhou, G. (2004). "GIS-based probabilistic mapping of landslide hazard using a three-dimensional deterministic model." *Natural Hazards*, 33(2), 265-282.

Xu, C. Y., Gong, L., Jiang, T., Chen, D., and Singh, V. P. (2006). "Analysis of spatial distribution and temporal trend of reference evapotranspiration and pan evaporation in Changjiang (Yangtze River) catchment." *Journal of Hydrology*, 327(1), 81-93.

Young, A. G., Honganen, C. D., Silva, A. J., and Bryant, W. R. (2000, January). "Comparison of geotechnical properties from large-diameter long cores and borings in deep water Gulf of Mexico." *Offshore Technology Conference*.

Yu, O. (2010). "Systems approach and quantitative decision tools for technology selection in Environmentally Friendly Drilling." Ph.D. Dissertation, Texas A&M University. College Station, TX.

Yu, O., Medina-Cetina, Z., Guikema, S., Briaud, J., and Burnett, D. (2012). "Integrated approach for the optimal selection of environmentally friendly drilling systems." *International Journal of Energy and Environmental Engineering*, 3(25), 1-18.